Università degli Studi di Cagliari

DOTTORATO DI RICERCA

INGEGNERIA INDUSTRIALE

Ciclo XXIX

TITOLO TESI

PHOTOELECTROCATALYTIC PERFORMANCE OF MIXED OXIDE ELECTRODES FOR APPLICATIONS IN SOLAR CELLS

Settore/i scientifico disciplinari di afferenza

ING-IND/27

Presentata da:	PABLO AMPUDIA CASTRESANA
Coordinatore Dottorato	FRANCESCO AYMERICH
Tutor	SIMONETTA PALMAS

Esame finale anno accademico 2015 – 2016
Tesi discussa nella sessione d'esame marzo 2017

Università degli Studi di Cagliari

DOTTORATO DI RICERCA

INGEGNERIA INDUSTRIALE

Ciclo XXIX

TITOLO TESI

PHOTOELECTROCATALYTIC PERFORMANCE OF MIXED OXIDE ELECTRODES FOR APPLICATIONS IN SOLAR CELLS

Settore/i scientifico disciplinari di afferenza

ING-IND/27

Presentata da:	PABLO AMPUDIA CASTRESANA
Coordinatore Dottorato	FRANCESCO AYMERICH
Tutor	SIMONETTA PALMAS

Esame finale anno accademico 2015 – 2016
Tesi discussa nella sessione d'esame marzo 2017

Contents

Abstract

The unique photocatalytic properties of several metal oxide semiconductors, such as TiO_2, Fe_2O_3 or WO_3, for the generation of electrons, holes or hydroxyl radicals allow their used as photocatalysts in three main processes: degradation or reduction of organic/inorganic pollutants, solar energy conversion and photoelectro-chemical water splitting. In particular, this Thesis presents the synthesis of semiconductor based materials for their used as photoanodes in photoelectro-chemical solar cells for hydrogen generation by the photoelectrosplitting of water.

The development of highly efficient and stable TiO_2 based photoanodes with both suitable band gap (E_g) and surface catalytic properties is one of the fundamental challenges in the photoelectro-chemical (PEC) water splitting. TiO_2 single-phase nanostructures have received considerable attention due to their unique physical properties, high activity, strong oxidation capability, chemical stability and numerous potential applications in solar energy systems. However, the photoactivity of this semiconductor is limited because titania does not possess both the E_g narrow enough to absorb a significant portion of visible light, and the potential of the conduction band edge negative enough to allow for proton reduction without the need to apply additional electric bias.

To solve this issue, this Thesis proposes the synthesis and modification of different TiO_2 nanostructures. In particular, WO_3 was considered as an attractive component to couple with TiO_2 in order to obtain TiO_2-WO_3 systems to be used as photoanodes in the photoelectrosplitting of water, under solar radiation. Compared to TiO_2 single-phase photo-catalysts, TiO_2-WO_3 hetero-nanostructures may allow increasing the efficiency of separation of the photogenerated charge and their lifetime, enhancing the light response range to the visible region, as well as the interfacial charge transfer to the absorbed substrates.

Different TiO_2-WO_3 photoanodes were prepared via one- or two-step electrochemical processes. The photoanodes will be composed of two oxide phases (TiO_2 and WO_3), which were combined in different ways. During

the first-step, compact or nanotubular layers were formed by either thermal oxidation or anodization of Ti foils. The anodization technique represented a very simple and useful way to obtain nanostructures the dimensions of which can be precisely controlled. In some cases, after the first-step of the synthesis process, a second-step was performed in which a WO_3 over-layer was electrochemically deposited on the obtained nanostructures.

The working mechanism of the different synthesized TiO_2-WO_3 systems will be investigated in order to propose a promising technique for synthesizing and modifying TiO_2 nanostructures, to obtain efficient TiO_2-WO_3 nanometric structures in large surface areas.

The attention has been firstly paid on the study of the morphology and electronic structure of TiO_2 based materials, to obtain TiO_2 nanostructures with good PEC performance. To this aim, different kinds of electrodes were obtained by electrochemical oxidation of titanium foils in a glycol organic solution under different working conditions. In particular, compact and nanotubular titania nanostructured electrodes were obtained in the absence or in the presence of fluoride ions in the solution, respectively. The results of the characterization of the synthesised electrodes were used to give indication about the benefit of using well-defined and ordered structures. The TiO_2 nanotubular structures led to higher values of photocurrent, which were correlated to a higher superficial area of the resulting electrode, but also to a better electron transfer trough the material.

However, the formation of TiO_2 nanotubes by anodic oxidation strongly depends on the operating conditions employed during the anodization process. Applied potential, anodization time, electrolyte composition and annealing temperature are some of the typical parameters that must be tailored in order to control both nanotube morphology (i.e. length and/ or the thickness) and also their crystalline structure.

In this context, the second part of the Thesis studies the effect of the anodization bath composition (i.e. organic solvent, water content and fluoride concentration) on both the structure and photoelectrocatalytic performance of TiO_2 nanotubes in the PEC water splitting reaction. For this purpose, the design of experiment (DOE) technique has been adopted with

the aim of identifying the minimum number of experiments required to evaluate both single and combined effects of the investigated parameters.

Then, an attempt is made to scale up the process for growing well ordered TiO_2 or TiO_2WO_3 nanotubar arrays on large surface (15 cm^2). The feasibility of the synthesis process was studied by testing the homogeneity of the titania nanotubular structures in terms of morphology and photoactivity.

The last study concerns the preparation and characterization of different semiconductor crystalline materials in the form of thin nanostructured layers, of TiO_2 single-phase or TiO_2-WO_3 mixed metal oxides, with different morphologies and distribution of the semiconductors in the combined structures.

The configuration of the proposed electrodes is indicated in the rest of the text as *A/B/C*, where "*A"* indicates the conductive substrate, while "*B"* and "*C"* represent the composition of the nanostructures (grown on the Ti foil) and the over-layer, respectively (see *Table 0.1*).

Table 0.1. *Configuration of the proposed electrodes: "A" indicates the nature of the conductive layer, "B" indicates the composition of the nanostructures grown on the Ti foil, and "C" indicates the composition of the over-layer.*

	*Configuration of the electrodes: "**A/B/C**"*			
	A	***B***	***C***	***"A/B/C"***
Single-phase electrodes	Ti	TiO_2	-	Ti/TiO_2
Mixed metal oxide electrodes	Ti	TiO_2	WO_3	$Ti/TiO_2/WO_3$
	Ti	TiO_2WO_3	-	Ti/TiO_2WO_3
	Ti	TiO_2WO_3	WO_3	$Ti/TiO_2WO_3/WO_3$

To obtain the proposed electrodes, different nanostructures (*B*) were

developed on a Ti foil (*A*). The nanostructures were obtained by Ti thermal oxidation or anodization of Ti foil in different organic solutions. These methods allowed the formation of directly back contacted electrodes since TiO_2, in the form of either compact or nanotubular layers, or also TiO_2WO_3 nanotubes grow directly on the Ti substrate. A second over-layer (*C*) of WO_3 was deposited on the obtained nanostructures. The over-layer of WO_3 was obtained via cathodic electrodeposition, by means of pulse potential technique (PPT).

The performances of the synthesized electrodes in alkaline or neutral supporting electrolytes were compared when the electrodes were irradiated with light at different wavelengths (320 nm, 365 nm, 380 nm, 400 nm and 430 nm). The effect of the presence of WO_3 in the nanotubular structure, as well as of the WO_3 loading on the performance of the TiO_2-WO_3 systems were investigated. The charge transfer mechanism at the combined system was also studied. The results from runs carried out in solutions containing glycerol were used to study the possible role of the WO_3 over-layer in the whole working mechanism of the combined structure. Finally, the photoactivity of the best performing electrodes was evaluated in the UV-vis range of the light.

Chapter 1 Overview of the Thesis

A summary of the thesis is given in this chapter, by showing how it is structured in different Chapters. Furthermore, a list of publications in journals and conference papers and other activities of the author are presented.

1.1 Motivation

The development of efficient anodic semiconductor materials represents a critical point when molecular hydrogen is obtained by the photoelectrocatalytic water splitting. It is well known that the cathodic generation of H_2 is effectively limited by the corresponding anodic oxidation of water; thus, lowering the anodic overpotential for the oxygen evolution reaction results also in improving the efficiency of H_2 production. In this context, the synthesis of highly efficient and stable photoanodes with both suitable band gap and surface catalytic properties becomes a fundamental challenge.

Nanostructured TiO_2 materials have been widely proposed as single-phase photoanodes for photoelectrochemical applications, in which the solar radiation to hydrogen conversion efficiency can be influenced by the configuration of the anodic material. There are several factors regarding the preparation of titania based photoanodes that have not to be ignored for a good performance of the PEC system and to promote the scale-up of PEC devices. The synthesis process (chemical or electrochemical), the type of substrate used to provide the electric contact between TiO_2 and the external circuit (transparent or opaque conductive substrates) or the morphology and dimensions of the nanostructures, are some of the factors to be considered to improve the performance of the anodic material, and in turns the global efficiency of the PEC process. Consequently, the study of the role of such factors in determining the optimal configuration of TiO_2 based photoanodes is very important.

On the other hand, the photoactivity of TiO_2 is limited to the UV range of the solar spectrum. To solve this limitation, TiO_2 is proposed in the present work as a component in a mixed oxide system, in which the coupling between semiconductors may be a route to exploit the positive characteristics of the single components in a synergic way to achieve better photoelectrocatalytic performance in a wider range of wavelengths.

The present investigation considers WO_3 as possible component to couple with TiO_2 photoanode to be used in the photoelectrosplitting of water. WO_3

is an indirect band gap semiconductor, which like TiO_2, presents favorable characteristics including chemical inertness and exceptional chemical and photoelectrochemical stability in aqueous media. Moreover, the relatively low band gap value of WO_3 (2.8 eV) extends the photoresponse of this material into the visible wavelength range, much more than for TiO_2.

Considering the photoelectrochemical activity of the TiO_2-WO_3 system fixed at a conductive support to which an external bias potential is applied, several authors report results on the positive performance of the combined structure. However, the working mechanism of the combined system is still not fully understood; some factors, such as the applied potential, the presence of a redox couple in the electrolyte or the irradiation by light of a suitable wavelength, may determine the charge transfer mechanism. Moreover, the reciprocal position of the two semiconductors and their position with respect to the electric contact were found to play an important role for an efficient charge transfer.

In this context, all the aspects involving not only the electronics of the semiconductor, but also the morphology of the oxides, the extent of the interface between the two semiconductors, as well as between electrode/electrolyte become paramount to be considered in order to guarantee a right working of the system.

The present work wants to give a contribution in this direction, being it addressed to study the behavior of the TiO_2-WO_3 combined structures during the photoelectrosplitting of water.

In particular, compact or tubular TiO_2 as well as tubular TiO_2WO_3 nanostructures were prepared and used as supports for the deposition of tungsten oxide. The nanotubular structures were obtained by electrochemical oxidation of Ti foils in specific electrolytic baths while the compact oxide was obtained both by thermal oxidation or anodization of Ti. WO_3 was cathodically electrodeposited on the different supports by using a pulse potential technique; to obtain different TiO_2-WO_3 combined structures.

The photoelectrochemical performance of the supports and the combined TiO_2-WO_3 nanostructures was investigated to give indications of the charge transport mechanism in the semiconductor structure. In the specific, the effect of *i)* the morphology of the TiO_2 support, *ii)* the WO_3 loading and *iii)* the disposition of the semiconductors with respect to the electric contact on the charge transfer mechanism in the TiO_2-WO_3 combined structure was studied, to obtain a photoanode characterized by a good performance also in the visible range of the solar spectrum.

1.2 Summary

The Thesis is structured in four main chapters; each one subdivided in different sections in order to help the reader to better follow the argument of the research project.

A summary of this Thesis is shown in the following list, where a brief description of each chapter is given.

Chapter 2 –Background

This chapter introduces the current problems concerning to the energy issues. In particular, the photoelectrochemical solar cell is proposed as an alternative device for the absorption of light and its conversion into useful energy or fuels. The basis of the semiconductors physics and other aspects concerning to the electrochemistry of semiconductors will be also explained.

Chapter 3 - Materials and Methods

This chapter presents the materials and methods used for the synthesis and characterization of either TiO_2 single phase or TiO_2WO_3 mixed oxide electrodes.

In the specific, the synthesis process of compact or tubular nanostructures was reported in this chapter. A description of the techniques used for the structural, optical, electro- and photoelectro-chemical characterization of the electrodes will be also given.

Chapter 4 - Results and Discussion

This chapter reports the results derived from the optical, structural, electro- and photoelecro-chemical characterization performed at the synthesized electrodes. The results will be compared in order to establish efficient nanostructured materials for solar cell applications.

This chapter is subdivided in the following sections:

4.1. TiO_2 Nanostructures: Ti/TiO_2 electrodes.

4.2. Effect of the synthesis conditions on the morphology and photoactivity of TiO_2 electrodes.

4.3. Scale up of the oxidation process to obtain TiO_2 or TiO_2WO_3 nanotubes.

4.4. Combined systems: $Ti/TiO_2/WO_3$ electrodes.

4.5. Combined systems: $Ti/TiO_2WO_3/WO_3$ electrodes.

4.6. Photoelectroactivity of the best performing samples under UV-vis simultaneous irradiation.

Chapter 5 – Final Conclusions

This final chapter reports the final conclusions.

1.3 Publications

Some of the topics present in this Thesis have been published in international journal papers, national and international congresses/conferences.

International Journal Papers:

Palmas S., Ampudia Castresana P., Mais L., Vacca A., Mascia M., Ricci P.C., *TiO_2-WO_3 nanostructured systems for photoelectrochemical applications*, RSC Adv., 6, pp. 101671- 101682, 2016, DOI: 10.1039/c6ra18649a.

Mais L., Ampudia Castresana P., Palmas S., Vacca A., Mascia M., Ferrara F., *Synthesis of Nanostructured Materials for Photoelectrochemical Oxidation of Organic Compounds*, Chemical Engineering Transactions, vol. 47, pp. 157-162, 2016, DOI: 10.3303/CET1647027.

Ampudia P., Palmas S., Vacca A., Mascia M., Matarrese R., *Design of Experiments (doe) for Synthesis of Nanotubular Structured Electrodes*, Chemical Engineering Transactions, vol. 41, pp. 349-354, 2014, DOI: 10.3303/CET1441059.

National and International Congresses and Conferences:

Ampudia Castresana P., Mais L., Palmas S., Vacca A., Mascia M., *Enhancement of the WO_3 performances for PEC applications*. 67th Annual Meeting of the International Society of Electrochemistry, The Hague, The Netherlands, August 2016.

Mais L., Ampudia Castresana P., Palmas S., Vacca A., Mascia M., Ferrara F., *Synthesis of Nanostructured Materials for Photoelectrochemical Oxidation of Organic Compounds*. NINE, International Conference on Nanotechnology based Innovative Applications for the Enviroment, Rome, Italy, March 2016.

Ampudia P., Palmas S., Vacca A., Mascia M., Matarrese R. *Design of Experiments (doe) for Synthesis of Nanotubular Structured Electrodes*. 10th European Symposium on Electrochemical Engineering, Domus de Maria (CA), Sardinia – Italy, September 2014.

Ampudia Castresana. P, Palmas S., Vacca A., Mascia M, Monasterio Martinez S., Mais L., Rizzardini S., Musu E., Systematic Investigation on the Effect of the *Synthesis Conditions on the Performance of Nanotubular Structured Electrodes*. SiO_2 Advanced Dielectrics and Related Devices X International Symposium, Cagliari, June 2014.

In addition to the work presented in this Thesis the author has also participated, during the course of the study, in other research projects.

International Journal Papers:

Ampudia Castresana P., Palmas S., Vacca A., Mascia M., Mais L., Marken F., *Mixed Oxides for Photo-electrochemical Applications*, Chemical Engineering Transactions, vol. 47, pp. 145-150, 2016, DOI: 10.3303/CET1647025.

Palmas S., Mascia M., Vacca A., Llanos J., Mena E., Rodrigo M., Ampudia P., *Hybrid Nanotubular Structures for Photoelectrocatalysis Or Energy Storage Devices*, Chemical Engineering Transactions, vol. 41, pp. 337-342, 2014, DOI: 10.3303/CET1441057.

National and International Congresses and Conferences:

Mais L., Ampudia Castresana P., Palmas S., Vacca A., Mascia M., *Electrochemical behaviour of synthesized Cu-Ni composites for CO_2 electroreduction*. 67th Annual Meeting of the International Society of Electrochemistry, The Hague, The Netherlands, August 2016.

Ampudia Castresana P., Palmas S., Vacca A., Mascia M., Mais L., Marken F, *Nickel oxide based electrodes as non-precious cathode for Oxygen Reduction Reaction*. E-MRS 2016 Spring Meeting (Symposium E), Lille, France, May 2016.

Ampudia Castresana P., Palmas S., Vacca A., Mascia M., Mais L., Marken F, *Mixed Oxides for Photo-electrochemical Applications*. NINE, International Conference on Nanotechnology based Innovative Applications for the Enviroment, Rome, Italy, March 2016.

Mais L., Ampudia P., Palmas S., Mascia M., Vacca A., Ferrara.,F Pettinau A, *Photo-anode driven solar cell for possible applications in photoelectrochemical reduction of CO_2*. Giornate dell'Elettrochimica Italiana (GEI2015), Bertinoro, Italy, July 2015.

Palmas S., Vacca A., Mascia M., Ampudia P., Mais L., Ferrara F Pettinau A., *On the behavior of modified TiO_2 nanotubes for a photoanode-driven photoelectrochemical reduction of CO_2*. Tech Connect World Innovation Conference & Expo. Washington DC, USA, June 2015.

Palmas S., Mascia M., Vacca A., Llanos J., Mena E., Rodrigo M., Ampudia P., *Hybrid Nanotubular Structures for Photoelectrocatalysis Or Energy Storage Devices*. 10th European Symposium on Electrochemical Engineering, Domus de Maria (CA), Sardinia – Italy, September 2014.

S. Palmas, A.Vacca, M. Mascia, P. Ampudia, *On the Behaviour of Electrochemical Capacitors Based on Nanostructured Hybrid TiO_2 Electrodes*. 65th Annual Meeting of the International Society of Electrochemistry, Lausanne – Switzerland, August 2014.

Chapter 2 Background

This chapter introduces the current problems concerning to the energy issues. In particular, the photoelectro-chemical solar cell is proposed as an alternative device for the absorption of light and its conversion into useful energy or fuels. The basis of the semiconductors physics and other aspects concerning to the electrochemistry of semiconductors will be also explained.

2.1 Brief Overview: From fossil to solar fuels

According to British Petroleum's 2016 Statistical Review of World Energy [1], global primary energy consumption grew by a below-average 1.0% in 2015, the slowest rate of growth since 1998; all fuels except nuclear power and oil grew at below-average rates. At present, the main fraction of the global energy is generated from carbon based fuels, and in the short term this fraction is unlikely to decrease because natural gas moves in to fill the gap in carbon based energy resources. However, renewable energy resources play an important role in the medium to longer term if there is to be a hope of limiting global emissions to levels that will mitigate the impact of the carbon dioxide accumulation on global climate change [2].

Currently, renewables in power generation account for a record of 2.8% of global primary energy consumption [1]. In particular, due to its advantages as a source of renewable energy, a rapid expansion of solar energy based systems for the generation of electricity, is likely to occur over the next years. However, the transport sector, which account for around 30% of primary energy consumption, will almost remain based on carbon-based fuels for the foreseeable future. This fact, have promoted the development of viable routes to obtain solar fuels, such as H_2, via light driven electrochemical processes.

Two generic approaches to achieving this goal are: photovoltaic powered electrolysis of water and direct photoelectrochemical generation of hydrogen from water [3]. The electrical power generated by photovoltaics could drive electrochemical water electrolysis to produce H_2, which could then be used either directly in fuel cells or alternatively as feedstock for the synthesis of carbon based fuels from carbon dioxide. On the other hand, the direct solar to chemical energy conversion in PEC cells is generally considered more practical, efficient and less expensive method for H_2 production if compared to photovoltaic powered electrolysis: in PEC cells, light energy collection and water splitting occurs into one device [2,4–8].

Since the publication of the highly cited paper of Fujishima, K. Honda et al. [9], in which the light driven water splitting process in a cell constituited of an n-type TiO_2 rutile photoanode and a platinum cathode was reported,

more than a decade of international effort have been made in order to find stable and efficient systems for the photoelectrochemical water splitting. Nevertheless, the research in this topic is still open; during the recent years several investigations have been done for the development of new efficient semiconductor materials to be used as photoanodes in PEC systems.

In particular, the most efficient water splitting photoanodes should have good qualities for efficient harvesting of the solar irradiation. Moreover, they have to drive water oxidation in aqueous solutions at a sufficient rate and current densities without being degraded for a long period of time [4,10].

Such a set of requirements cannot be easily achieve by a single material, therefore tandem devices [11–13], several methods for the protection of the semiconductors from the photocorrosion [14–18] as well as the synthesis of heterostructures [7,19–25], have been widely explored over the recent years (2010 – 2015), as can be seen from the list of the referenced literature [4].

2.2 PEC water splitting at Semiconductors

Figure 2.1 shows a simplified energy diagram of a photoelectro-chemical cell based on a single-phase photo-anode and a metal counter electrode immersed in an aqueous solution. The main component of the PEC cell is the semiconductor, which converts incident photons to electron/hole pairs. These electrons and holes are spatially separated from each other due to the presence of an electric field inside the semiconductor.

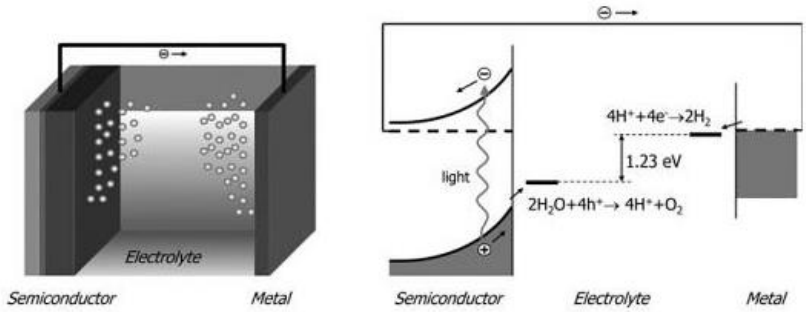

Figure 2.1. *Illustration of a photoelectron-chemical cell that consists of a semiconducting photoanode and a metal cathode. The corresponding energy diagram is shown in the right.*

The photogenerated electrons are swept toward the conducting back contact, and are transported to the metal counter-electrode via an external wire. At the metal, the electrons reduce water to form hydrogen gas. The photo-generated holes are swept toward the semiconductor/electrolyte interface, where they oxidize water to form oxygen gas. Usually an ammeter and the voltmeter are used to record the currents and potential differences involved in the cell. For an alkaline electrolyte, the reduction and oxidation reactions can be written as[1]:

$$4H_2O + 4e^- \longleftrightarrow 2H_2 + 4OH^- \quad E^O_{\mathrm{Red}} = -0.828V \qquad \textbf{(2.1)}$$

$$4OH^- + 4h^+ \longleftrightarrow 2H_2O + O_2 \quad E^O_{\mathrm{Red}} = -0.401V \qquad \textbf{(2.2)}$$

As an example, when TiO_2 is used as photoanode, the water splitting can be described according to the following mechanism:

$$TiO_2 + 2h\nu \rightarrow TiO_2 + 2e^- + 2h^+ \qquad \textbf{(2.3)}$$

$$2h^+ + H_2O \rightarrow \tfrac{1}{2}\, O_2 + 2H^+ \qquad \textbf{(2.4)}$$

$$2e^- + 2H+ \rightarrow H_2 \qquad \textbf{(2.5)}$$

[1]*Note that the sign of the potential for the oxidation half-reactions is opposite from that usually encountered in the literature, which usually lists these reactions as reduction reactions*

$$H_2O + 2h\nu \rightarrow \frac{1}{2} O_2 + H_2 \quad \textbf{(2.6)}$$

In this model, the TiO_2 photoelectrode is energized due to the absorption of two photons (a) generating electrons and holes. Then, the water is oxidized with the holes in the photo-electrode (b) and it is reduced at the counter electrode with the electrons, which flows to him (c). As net process, the water is decomposed into oxygen and hydrogen from the radiation, the semiconductor is the reaction promoter, which is activated by the radiation. It is important to note that the step "a" represents an overall process by which the semiconductor material is energized from the two-photon absorption.

2.3 Elemental semiconductors

2.3.1 Fundamental of semiconductor physics

The properties of semiconductor electrodes, and the differences from those of metallic electrodes, can be understood by examining the electronic structures of these materials [26]. Due to the high number of atoms that must be considered, electronic structure of solids is normally discussed in terms of energy bands, which are made up of the atomic orbitals of the individual atoms. As a result of the large number of orbitals, the energetic difference between adjacent molecular orbitals within a given energy band is so small that the bands can be effectively considered a continuum of energy levels. The highest and lowest level of a band is referred to as the band edges. As it happens with molecular orbitals, also in the case of bands, the energy bands of interest are the highest occupied (Valence Band, VB) and the lowest unoccupied (Conduction Band, CB) [27]. The difference in energy between the VB and the CB is the Band Gap (E_g) and it plays a basic influence over the properties of the material.

Conductivity of a solid-state material is defined by capacity of electrons to move through the material. This will depend on the level of occupancy of the bands by electrons, and on the distance between the bands. Metals are

considered as good conductors because the conduction and valance bands overlap, allowing the free movement of electrons. For insulators, the distance between the bands is sufficiently large to avoid the promotion of electrons from the VB to the CB. Differently, semiconductors have not a so distanced band as insulators, but they are not overlapped as metals. Band gap of semiconductors is enough, typically in the range of 1 - 4 eV (see *Figure 2.2*), to allow the increase of conductivity by electrons excitation.

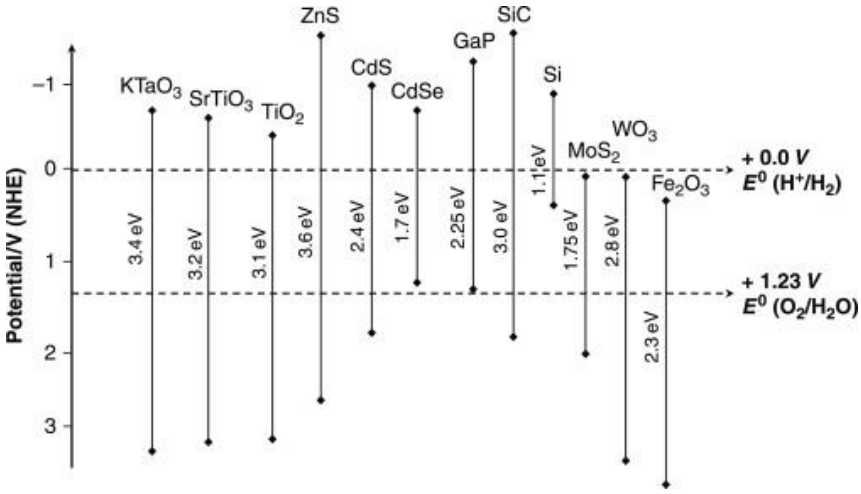

Figure 2.2. *Valance and conductance band positions for various semiconductors, and relevant redox couples.*

From electronic energy plot, is possible to see how the bands change depending on the character of solids: the bands overlap for metals, the band gap is relatively low for semiconductor, and finally for insulators the distance between the bands becomes very large. *Figure 2.3* shows the distinction between semiconductors, metal and insulators. The difference resides in energy band gap and the occupancy of bands.

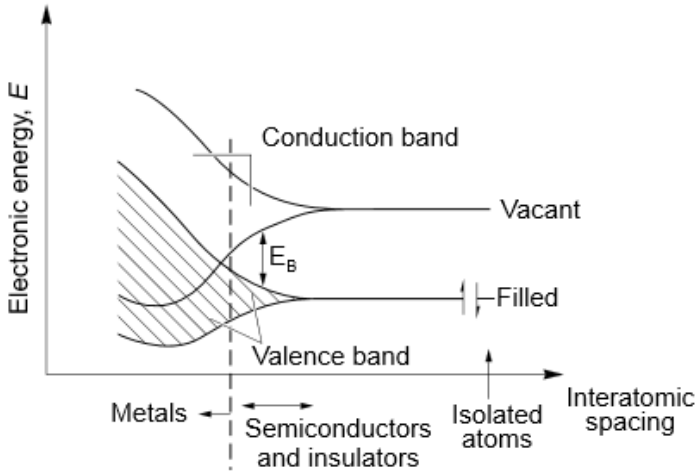

Figure 2.3. *Generation of bands in solids from atomic orbitals of isolated atoms. Taken from Ref. [29].*

Another important concept in discussion of solid-state materials is the Fermi level (E_f). This is defined as the energy level at which the probability of occupation by an electron is ½; for example, for an intrinsic semiconductor the Fermi level lies at the mid-point of the band gap (*Figure 2.4*). Doping changes the distribution of electrons within the solid, and hence changes the Fermi level. For an n-type semiconductor, the Fermi level lies just below the conduction band, whereas for a p-type semiconductor it lies just above the valence band (*Figure 2.5*).

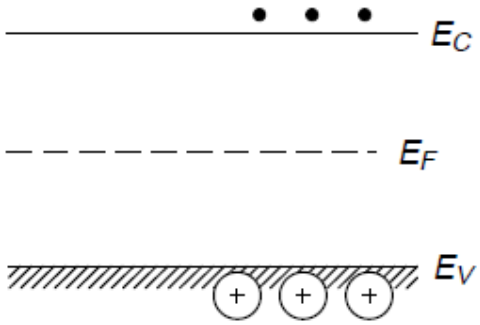

Figure 2.4. *Schematic diagram of the energy levels of an intrinsic semiconductor. Taken from Ref. [29].*

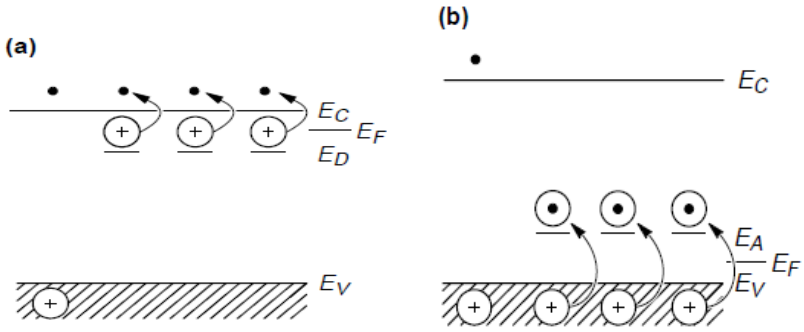

Figure 2.5. *Schematic diagram of the energy levels of n-type (a) and (b) p-type semiconductors. Taken from Ref. [29].*

In addition, as with metal electrodes, the Fermi level of a semiconductor electrode varies with the applied potential; for example, moving to more negative potentials will raise the Fermi level. We now need to consider what happens at the (idealized) interface between a semiconductor electrode and an electrolyte solution. When the two phases to be in equilibrium, their electrochemical potential must be the same. The electrochemical potential of the solution is determined by the redox potential of the electrolyte solution, and the Fermi level determines the redox potential of the semiconductor. If the redox potential of the solution and the Fermi level do

not lie at the same energy, a movement of charge between the semiconductor and the solution is required in order to equilibrate the two phases. The excess charge that is now located on the semiconductor does not lie at the surface, as it would for a metallic electrode, but extends into the electrode for a significant distance (100-10,000 Å). This region is referred to as the space charge region, and has an associated electrical field. Hence, there are two double layers to consider: the interfacial (electrode/electrolyte) double layer, and the space charge double layer.

For an *n*-type semiconductor electrode at open circuit, the Fermi level is typically higher than the redox potential of the electrolyte, and hence electrons will be transferred from the electrode into the solution.

Therefore, there is a positive charge associated with the space charge region, and this is reflected in an upward bending of the band edges (*Figure 2.6a* and *Figure 2.7a*). Since the majority charge carrier of the semiconductor has been removed from this region, this region is also referred to as a depletion layer.

For a p-type semiconductor, the Fermi layer is generally lower than the redox potential, and hence electrons must transfer from the solution to the electrode to attain equilibrium. This generates a negative charge in the space charge region, which causes a downward bending in the band edges (*Figure 2.6b* and *Figure 2.7b*). Since the holes in the space charge region are removed by this process, this region is again a depletion layer. As for metallic electrodes, changing the potential applied to the electrode shifts the Fermi level. The band edges in the interior of the semiconductor (i.e., away from the depletion region) also vary with the applied potential in the same way as the Fermi level. However, the energies of the band edges at the interface are not affected by changes in the applied potential.

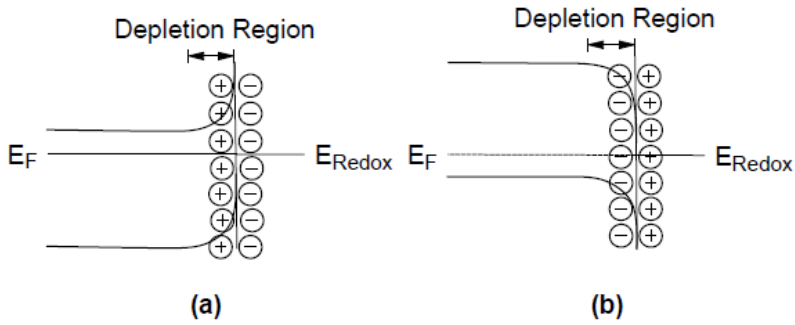

Figure 2.6. *Band bending for an n-type (a) and (b) a p-type semiconductor in equilibrium with an electrolyte. Taken from Ref. [29].*

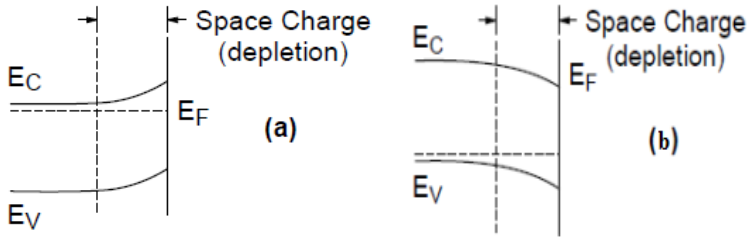

Figure 2.7. *Effect of varying the applied potential (E) on the band edges in the interior of an n-type semiconductor (a) $E > E_f$ and (b) effect of varying the applied potential (E) on the band edges in the interior of a p-type semiconductor. $E < E_f$. Taken from Ref. [29].*

Therefore, the change in the energies of the band edges on going from the interior of the semiconductor to the interface and hence the magnitude and direction of band bending, varies with the applied potential. As it is explained in the literature, there are three different situations to be considered. One of these situations is represented in the *Figure 2.7*, which shows how the depletion regions arise at potentials positive of the flatband potential for an n-type semiconductor and at potentials negative of the flatband potential for a p-type semiconductor.

2.3.2 Fundamental of semiconductors: Electrochemistry

A description of well established aspects related to the semiconductor energy band model and electrostatics at the semiconductor-electrolyte interfaces in dark conditions will be reported in this section.

2.3.2.1 Semiconductor-electrolyte interface

When a metal is partly immersed in an electrolyte, a potential is set up across the two phases, i.e., at the electrode/electrolyte interface. The phases may be solids (metals or alloys, semiconductors, insulators), liquids (ionic liquids, molten salts, neutral solutions), or gases (polar or non polar). The more common terminology in electrochemistry is that a double layer is set up at the interface. There are several reasons for a potential difference being set up across the interface of two phases, the most common one being the charge transfer occurring across the interface. During this process, a charge separation will occur because of electron transfer across the interface. Other reasons for the occurrence of potential differences are due to surface-active groups in the ionizable media (liquid, solid, or gas) and orientation of permanent or induced dipoles.

The double layer at the interface between two phases has electrical, compositional, and structural characteristics. The electrical and compositional characteristics deal with the excess charge densities on each phase and the structural one with the distribution of the constituents (ions, electrons, dipoles, and neutral molecules) in the two phases, including the interfacial region. A brief description of the theoretical aspects of the structure of the double layer, as applied to electrode/electrolyte interfaces, across which charge transfer reactions occur, is presented below [28].

If a semiconductor is immersed in a redox electrolyte the equilibrium is reached at the interface when the Fermi levels of the two phases is the same. In the case of a redox electrolyte, the electrochemical potential of electrons is given by the Nernst expression:

$$E_{redox} = E^{0}_{redox} + \frac{RT}{nF} ln \frac{a_{ox}}{a_{red}} \qquad (2.7)$$

where *E* redox is the standard redox potential, *R* is the universal gas constant, *T* is the absolute temperature, *F* is the Faraday constant, *n* is the number of electrons transferred, and a_{ox} and a_{red} are the activities of the oxidized and reduced species, respectively. The parameter E_{redox} can be identified with the Fermi level of redox electrolyte ($E_{F,redox}=E_{redox}$) [29].

The model developed by Gerischer [29] to describe the interface semiconductor-liquid phase, is still used today. Besides the Fermi level of the redox system, this model introduced the existence of occupied and empty energy states corresponding to the reduced and the oxidized species of the redox system, respectively. The model leads to a Gaussian distribution of the redox states versus electron energy as illustrated on the right side of *Figure 2.8*. The distribution functions for the states are given by

$$\boldsymbol{D_{ox} = exp\left[-\frac{\left(E-E_{F,redox}-\lambda\right)^2}{4kT\lambda}\right]} \qquad \textbf{(2.8)}$$

$$\boldsymbol{D_{red} = exp\left[-\frac{\left(E-E_{F,redox}-\lambda\right)^2}{4kT\lambda}\right]} \qquad \textbf{(2.9)}$$

In which λ is the reorganization energy of electron transfer and *kT* thermal energy [30]. *Figure 2.8* displays a detailed picture of energy levels of semiconductors bands and energy distribution of occupied and unoccupied states of a redox couple.

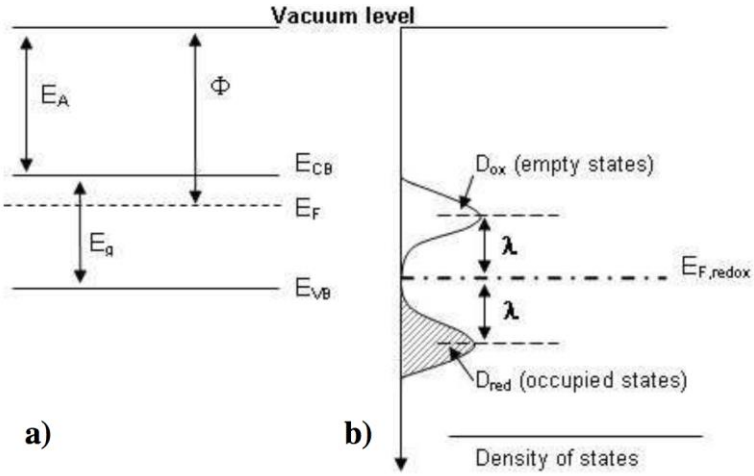

Figure 2.8. *a) Energy levels of semiconductor bands. E_A and Φ are the semiconductor-electron affinity and work function, respectively. b) Energy distribution of occupied and unoccupied states of a redox couple. (Adapted from Ref [31].*

Supposing the case in which an n-type semiconductor is in contact with a redox electrolyte, initially the electrochemical potentials or Fermi levels are different, so a flow of charge carriers takes place between semiconductor and solution in order to equilibrate the electrochemical potentials of two phases.

For an n-type semiconductor the Fermi level is typically higher than electrochemical potential or redox electrolyte. So, a flow of electrons takes place from the semiconductor to the electrolyte, to guarantee the reaching of the equilibrium. This results in a charging of the interphase, that will be positively charged at the electrode side and negatively charged at the solution side (*Figure 2.9a*). In the case of a p-type semiconductor, the inverse process happens: the Fermi level of semiconductor is situated below the electrochemical potential of redox electrolyte, therefore electron transfer from electrolyte to semiconductor occurs. Consequently, the semiconductor acquires a negative charge, and electrolyte is positively charged (*Figure 2.9b*).

For lightly doped semiconductors, this excess of charge does not stay at semiconductor surface, because the density of states is not enough to

accommodate it. Hence, the charge extends inside the electrode, generating a region of a distance of 10-1000 nm approximately, defined as *space charge region*. Since this region is depleted of its majority charge carriers, the zone is also known as *depletion layer* [32]. This process results in the generation of an electric field in the space charge region, which modifies the electrochemical potential of electrons, being different near the surface region and in the bulk. That difference is represented like a *band-bending* in the Gerischer diagram.

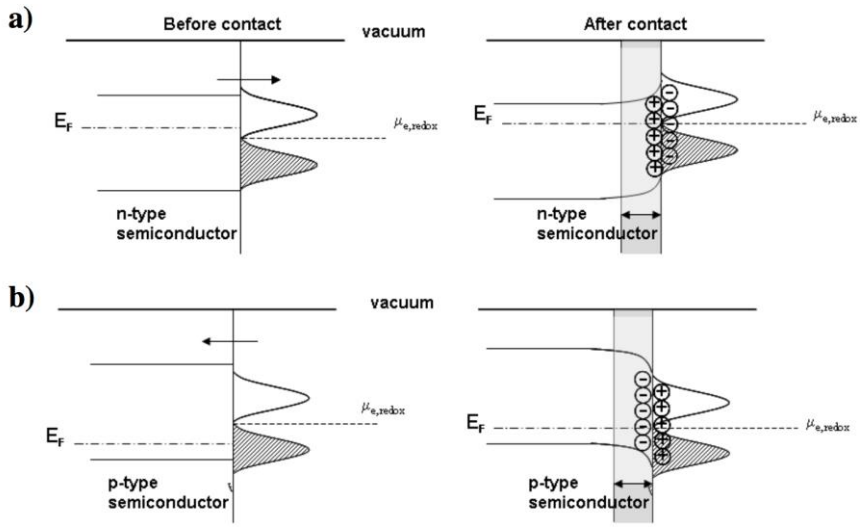

Figure 2.9. *Interface semiconductor before and after equilibration: a) n-type semiconductor b) p- type semiconductor. (Adapted from Ref. [33].*

This bending of bands can be understood in terms of a continuously growing barrier for interfacial electron transfer when moving from the bulk of the semiconductor to the interface due to the continuously less efficient screening of the negative charges in the solution by the positive charges in the depletion layer. Φ_{sc} is the height of the barrier, and corresponds to the difference created between the bulk of the semiconductor and the interface due to band-bending. This concept is reported in *Figure 2.10*.

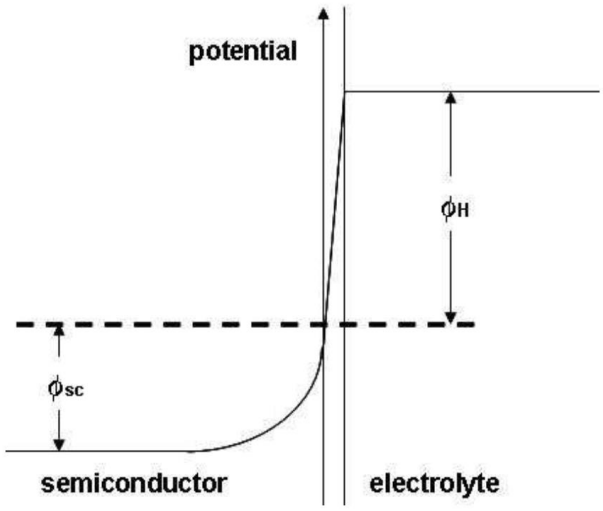

Figure 2.10. *Band-bending for an n-type semiconductor electrode upon equilibration of the Fermi level of the semiconductor with the redox specie. The height of the barrier is represented by* Φ_{SC} *(adapted from Ref. [31,32]).*

In order to completely describe the interface, also the potential distribution in the solution side must be considered. *Figure 2.11* depicts a typical picture of the electrical layers which are origin

ated due to the adsorption of ions or molecules of the solvent, orientation of dipoles and formation of surface bonds from solid and species in solution [31]. In particular, the Helmoltz and the Gouy-Chapman layers are well evidenced in *Figure 2.11*. As for electrolyte/metal interfaces, in the case of very diluted solutions, the Gouy-Chapman layer must be considered, but with a sufficiently high ion concentration, as is in our case in which a supporting electrolyte is used, it can be neglected. However, unlikely for electrolyte/metal interface, in which the charge is concentrated on the surface, and the complete potential drop occurs within the Helmoltz layer in the electrolyte phase, in case of semiconductors also the space charge region must be considered. So when the whole interface is considered, it can be essentially modeled by two capacitors in series (*Figure 2.11*).

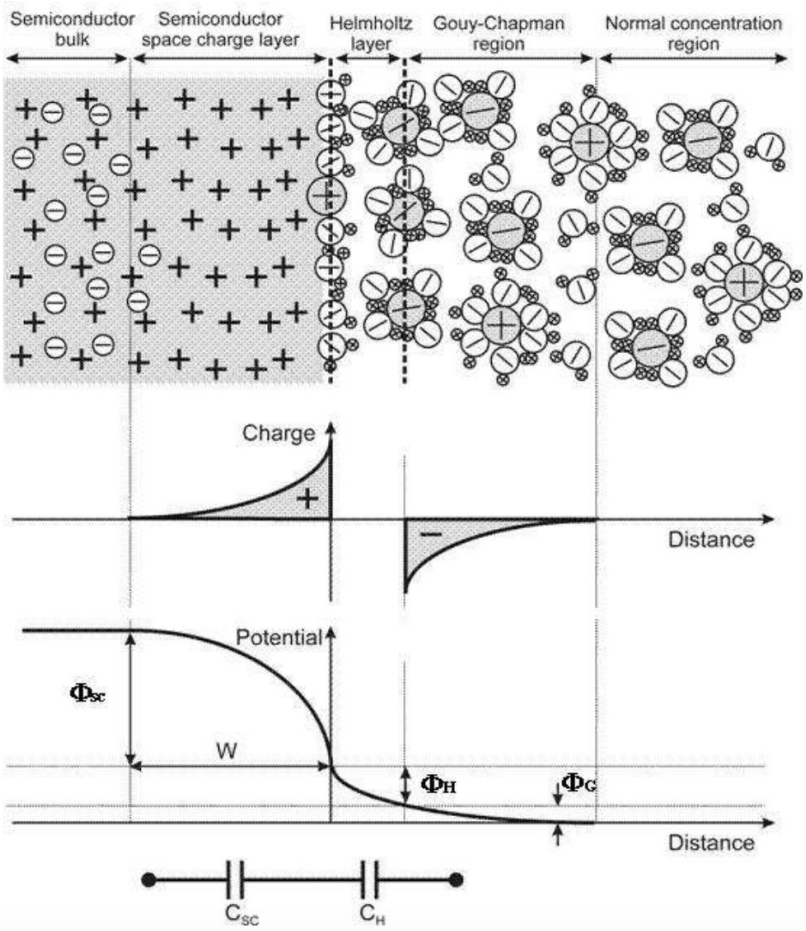

Figure 2.11. *Potential and charge distribution at semiconductor-electrolyte interface. The three different double layers are also shown.* Φ_{sc}, Φ_H, Φ_G *are the space charge, Helmoltz and Gouy double layer potentials, respectively, and W the width of the space charge layer (taken from Ref. [29]).*

Considering the relative disposition of these energy levels with respect to the semiconductor band edge positions at interface, the total potential difference in the interface (Φ_t) can be expressed as the sum of the two contributions related to space charge (Φ_{SC}) and Helmoltz layer (Φ_H):

$$\boldsymbol{\Phi_t = \Phi_{SC} + \Phi_H} \qquad \textbf{(2.10)}$$

where Φ_t is measured between an ohmic contact on the rear surface of the semiconductor electrode and the reference electrode.

Actually, if equation 2.11 holds:

$$\frac{1}{C} = \frac{1}{C_{SC}} + \frac{1}{C_H} \quad \textbf{(2.11)}$$

Considering a single crystal behavior, low doping and absence of surface states, it is possible to assume than the capacity C_{SC} is much smaller than C_H ($C_{SC} << C_H$), so that:

$$\frac{1}{C} = \frac{1}{C_{SC}} \quad \textbf{(2.12)}$$

Moreover, assuming that the space charge layer can be described as capacitor, its capacity can be defined by:

$$C = \frac{dQ}{d\Phi} = \frac{A\varepsilon_r\varepsilon_0}{d} \quad \textbf{(2.13)}$$

where dQ is the variation of the accumulated charge, ε_r is the dielectric constant of the semiconductor, ε_o is the permittivity of free space and A and d represent the surface area and the distance between the two faces of the capacitor.

The electric field in the depletion zone can be defined using the Gauss law:

$$\left(\frac{dQ}{d\Phi}\right)_{\Phi_{SC}} = \frac{q_{SC}}{\varepsilon_r\varepsilon_0 A} = \frac{Q_{SC}}{\varepsilon_r\varepsilon_0} \quad \textbf{(2.14)}$$

The differential capacity of the space charge layer below the semiconductor surface can be derived quantitatively by solving the equation of Poisson [29,31,34]:

$$\frac{d^2\Phi}{dx^2} = \frac{q}{\varepsilon_r\varepsilon_0}[N_D - N_A - n(x) + p(x)] \quad \textbf{(2.15)}$$

where x is the distance from the surface, N_D and N_A the concentration of donator and acceptors, $n(x)$ and $p(x)$ are the densities of electrons and holes at thermodynamic equilibrium. For an n-type semiconductor, in the

depletion zone, N_A and $p(x)$ can be neglected. Now, taking into account the $n(x)$ definition:

$$\boldsymbol{n(x) = n_0 exp\left(-\frac{q\Phi}{kT}\right)} \quad \textbf{(2.16)}$$

where $n_0=N_D$ is the density of electrons in the bulk of the semiconductor, the equation of Poisson can be simplified as follows:

$$\boldsymbol{\frac{d^2\Phi}{dx^2} = \frac{qN_D}{\varepsilon_r\varepsilon_0}\left[1 - exp\left(-\frac{q\Phi}{kT}\right)\right]} \quad \textbf{(2.17)}$$

By integrating this equation under the boundary conditions dΦ/dx=0 when Φ=0 (potential gradient in the bulk is null when Φ=0) the following equation is obtained:

$$\boldsymbol{\left(\frac{d\Phi}{dx}\right)^2 = \frac{2qN_D}{\varepsilon_r\varepsilon_0}\left[\Phi + \frac{kT}{\varepsilon_r\varepsilon_0}\left(exp\left(-\frac{q\Phi}{kT}\right) - 1\right)\right]} \quad \textbf{(2.18)}$$

Paying attention on the space charge region, $\Phi=\Phi sc$, the term $exp(-q\Phi_{sc}/kT)$ can be neglected.

Combining equations 2.15 and 2.18, the following equation is obtained:

$$\boldsymbol{\left(\frac{d\Phi}{dx}\right)_{\Phi=\Phi_{SC}} = \frac{Q_{SC}}{\varepsilon_r\varepsilon_0} = \left(\frac{2qN_D}{\varepsilon_r\varepsilon_0}\left[\Phi_{SC} - \frac{kT}{\varepsilon_0}\right]^{1/2}\right)} \quad \textbf{(2.19)}$$

Finally, considering the definition of space charge region capacity ($C_{sc}= dQ_{sc}/d\Phi_{SC}$), and integrating again, the Mott-Schottky equation is obtained [29,35]:

$$\boldsymbol{\frac{1}{C_{SC}^2} = \frac{2}{\varepsilon_r\varepsilon_0 qN_D}\left(\Phi_{SC} - \frac{kT}{q}\right)} \quad \textbf{(2.20)}$$

Φ_{sc} can be defined as $E_{appl} - E_{fb}$.

So the Mott-Schottky equation can be re-written as:

$$\boldsymbol{\frac{1}{C_{SC}^2} = \frac{2}{\varepsilon_r\varepsilon_0 qN_D}\left(\left(E_{appl} - E_{fb}\right) - \frac{kT}{q}\right)} \quad \textbf{(2.21)}$$

Being E_{appl} the applied potential and E_{fb} the flat-band potential, i.e. the applied electrode potential at which the semiconductor energy bands are flat.

A plot of $1/C^2$ as a function Φ_{SC} of leads to a linear trend with positive or negative slope for p- and n- type semiconductors, respectively (*Figure 2.12*). An extrapolation of Mott-Schottky to $1/C_{sc}=0$ allows to individuate the flat band potential.

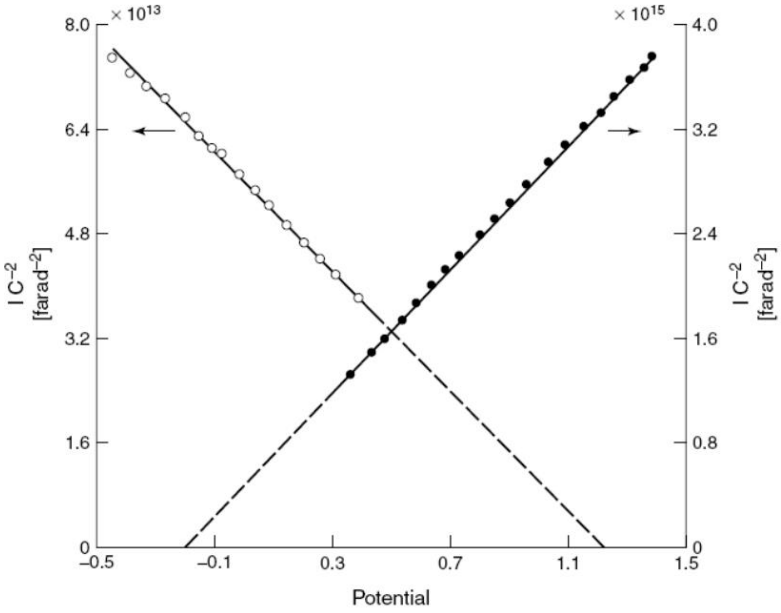

Figure 2.12. *Mott-Schottky plot, typical shape of an n-type (solid dots) and p-type semiconductor (white dots). The value in which $1/C_{SC}$ becomes zero corresponds to the flat band potential for each case. Taken from Ref. [29].*

However, if capacitor is perfect, variation of the Mott-Schottky slope, is observed depending on the range of investigated potential. Some authors [29,35] have explained the curve bending by the existence of multiple donor levels that are successively ionized with the potential increase. If surface states are not completely occupied, the applied potential is used to charge or discharged these surface states, and consequently the capacity of the

space charge layer is not modified because the charge remains in the surface states. However, in the case of surface states completely occupied or empty, C_{sc} is modified following the equation 2.21.

2.3.2.2 Potential profiles and Band gap positions

While the possibility of a semiconductor to be excited by the light depends on the wavelength of the incident light and the relevant band gap of the semiconductor, the ability of a semiconductor to undergo photoinduced electron transfer to adsorbed species on its surface is governed by the band energy positions of the semiconductor and the redox potentials of the adsorbate. The relevant potential level of the acceptor species is thermodynamically required to be below (more positive than) the conduction band potential of the semiconductor. The potential level of the donor needs to be above (more negative than) the valence band position of the semiconductor in order to donate an electron to the vacant hole. The band edge positions of several semiconductors are presented in *Figure 2.2*.

The knowledge of the Flat band potential (E_{fb}), as well as the positions of the band edges, becomes fundamental for the determination of the energetic position of the band edges, which provides crucial information of the oxidizing or reducing power of the photogenerated electrons or holes.

When an electrode is polarized, the total potential is sustained by each single layer at the interface. The main limit cases are explained as follows [29,36].

Assuming that a change in the electrode potential mainly entails a change in the space charge region potential, then $|\Delta\Phi_{SC}| >> |\Delta\Phi_H|$, $|\Delta\Phi_G|$. The fact that potential drops for Gouy and Helmoltz layers remain invariable, allows to consider that $|\Phi_t| = |\Phi_{SC}|$. In this case, conduction and valence bands positions at the surface keep unchanged (E_c and E_v in *Figure 2.13b*), and the boundary bands can be considered pinned at the surface, being the charge located in the space charge region. This situation is called band pinning.

If polarization of electrode provokes apparent changes in potential of Helmoltz layer, then $|\Phi_H|>>|\Phi_{SC}|, |\Phi_G|$. In these conditions, the energy of surface states shifts $e\Delta\Phi_H$ (see *Figure 2.13c*). In this case, respect to the Fermi level position, the energies of valence and conduction bands keep the position because the charge is now placed in the surface of the semiconductor. This situation is known as Fermi level pinning. This situation is often connected to the presence of surface states which can be involved in the charge transfer: when these states are present in the band gap, then the charge transfer will be preferentially mediated by surface states. In this case the energetics of the semiconductor is driven by these states, rather than by the bulk state of the semiconductor. In such a situation the band bending is more sensitive to the parameters such as a result of surface pretreatment, cleaning of the surface, adsorption, etc [33].

In real systems, it is usually to find an intermediate situation, in which polarization of electrode provokes simultaneously variation of $\Delta\Phi_H$ and $\Delta\Phi_{SC}$. Consequently not Fermi level pinning or band pinning are found.

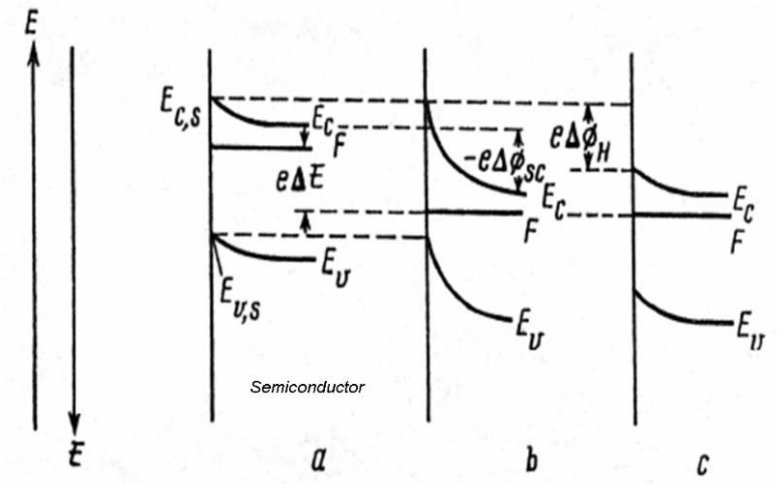

Figure 2.13. *Schematic representation of interface electrode-electrolyte under bias potential: (a) thermodynamic equilibrium situation (b) situation of band pinning and (c) situation of Fermi level pinning. Taken from Ref. [29].*

In order to verify the presence of a Fermi level pinning, it is needed the determination of flat band potential in the presence of couple compounds with different redox potentials. If E_{fb} depends of redox couple potential, the situation corresponds to a Fermi level pinning: the photopotential is independent of redox couple present in the solution.

2.3.2.3 Charge separation in the dark

Electron-transfer reactions at semiconductor electrodes in contact with redox electrolytes can follow two different pathways [27,29,37]: as shown in *Figure 2.14*, the electron transfer can be performed by electrons of the conduction band to oxidant species or by electrons from the reductor species to the valence band. The latter case corresponds to a transfer of holes.

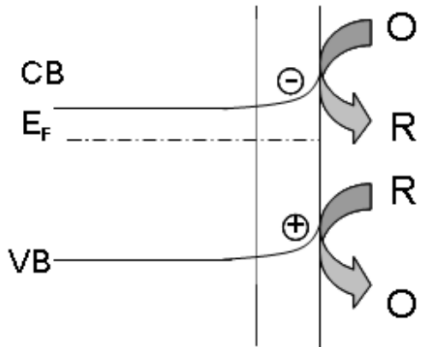

Figure 2.14. *Electron transfer reaction at the semiconductor interface in the dark for an n-type semiconductor. Taken from Ref. [29].*

Considering an n-type semiconductor in contact with a sufficiently stirred redox electrolyte (in order to current will not be limited by mass transfer of ions in the solution), in the dark the electron transfer will be the main charge transfer process. Actually, since there is an excess of electrons in the CB of the semiconductor, the electron transfer from the CB to the oxidant specie in solution (O) is favorited with respect to transfer from reductor specie (R) to VB. In this case electron has to overcome the potential drop in the space charge layer (Φsc) to arrive to the electrolyte, so a net cathodic current is obtained:

$$\boldsymbol{i_c = nFAk_f n_{SC} C_o\ (x = 0)} \qquad \textbf{(2.22)}$$

where k_f is the reaction rate constant for the reduction and n_{SC} is the density of electrons in the space charge region. In the case of a p-type semiconductor, oxidation of the reduced form is the favorite process, and consequently the anodic current is expressed as:

$$\boldsymbol{i_a = nFAk_b p_{SC} C_R\ (x = 0)} \qquad \textbf{(2.23)}$$

where k_b is the reaction rate constant for the oxidation process, and p_{SC} the density of holes in the space charge region.

Up to now, we have analyzed the charge transfer process without a potential bias applied, so the system is driven by Φ_{SC}. When the equilibrium is reached, the reaction rates of both processes at the electrode must be equal, and no current will flow at the interface.

Considering now the application of a bias potential to the interface, the heterogeneous rate constants (k_f and k_b) will vary with E according to the Butler- Volmer equations:

$$\boldsymbol{k_f = k^0 exp\left[-\frac{\alpha(E-E^{0'})}{RT}\right]} \qquad \textbf{(2.24)}$$

$$\boldsymbol{k_b = k^0 exp\left[-\frac{(1-\alpha)F(E-E^{0'})}{RT}\right]} \qquad \textbf{(2.25)}$$

Where $E^{0'}$ is the formal reduction potential of the redox couple and k is the standard rate constant that can be related to the exchange current density (i_0) at the interface. Its value depends upon the overlap of the electronic wave function of the semiconductor and the redox couple [29]. The higher the overlap, the faster is the charge transfer because the kinetics is favoured [33]. k_f and k_b depend on the potential drop at the Helmoltz layer across the interface, which could change with the applied potential.

However, semiconductors have a space charge region, and application of a bias potential will alter the composition of this region. This influence is considered by the carrier densities equations:

$$\boldsymbol{n_{SC} = N_D exp\left[-\frac{F(E-E_{fb})}{RT}\right]} \quad \textbf{(2.26)}$$

$$\boldsymbol{p_{SC} = N_A exp\left[\frac{F(E-E_{fb})}{RT}\right]} \quad \textbf{(2.27)}$$

In this case, (E-E_{fb}) can be substituted by potential drop or barrier height (Φ_{sc}). The applied potential alters the potential drop in the space charge region, controlling the current and the charge transfer in the cell. This situation is analogous to the current through a semiconductor-metal Schottky barrier [29], the only difference is that in an electrolyte the concentration of acceptor states for the charge carriers of the semiconductor is orders of magnitude smaller than in a metal and these states are localized and their energy levels fluctuate over a wide energy range [29]. In the present situation, variation of E affects n_{sc} and p_{sc} in *n*-type and *p*-type semiconductor respectively.

The applied potential induces changes in the energies of the band edges from the interior of the semiconductor to the interface modifying, hence, the magnitude and direction of band bending. If we consider an *n*-type semiconductor, depending of applied potential, different situations can be considered [29]. At a certain potential, the Fermi energy lies at the same energy as the solution redox potential. There is no net transfer of charge, and hence there is no band bending. This potential is therefore referred to as Efb (*Figure 2.15*a). At potentials negative of the flatband potential for an n-type semiconductor, there is now an excess of the majority charge carrier (electrons) in this space charge region, which is referred to as an accumulation region (*Figure 2.15*b). Depletion region arises at potentials positive of the flatband potential for an *n*-type semiconductor and at potentials negative of the flatband potential for a *p*-type semiconductor (*Figure 2.15*c).

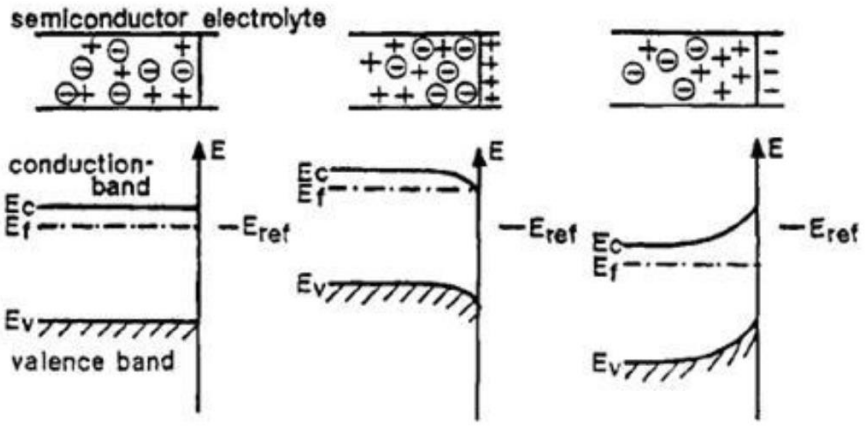

Figure 2.15. *Space charge layer formation at the n-type semiconductor-solution interface: (a) flat band situation, (b) accumulation layer, and (c) depletion layer. Taken from Ref. [29].*

Summarizing, in absence of an energetic radiation, the charge transfer abilities of a semiconductor electrode depend on whether the space charge layer is in accumulation or depletion state. In such a case, the behaviour of a semiconductor electrode is similar to that of a metallic electrode, since there is an excess of the majority charge carriers available for charge transfer. In the last case, when a depletion layer is originated, then there are few charge carriers available for charge transfer, and electron transfer reactions occur slowly, if at all.

2.3.3 Fundamental of semiconductors: Photoelectrochemistry

When a semiconductor electrode, immersed in a redox electrolyte, is irradiated by a light source having a photon energy (represented with hν, where h is the Planck constant and ν is the frequency) greater than the band gap of the semiconductor (E_g), electron/hole pairs are generated and separated in the electric field of the space charge layer.

The direction of the electric field at the interface, is such that the minority carriers are swept to the surface and the majority ones are driven to the bulk of the semiconductor and to the external circuit (depending of type of semiconductor), leading the separation of the photogenerated charge carriers. Hence, in the case of an *n*-type semiconductor, electric field will

drive electrons toward the interior of semiconductor and from there to the external circuit, and holes to the surface (*Figure 2.16*a). On the contrary, for a *p*-type semiconductor, the holes will be impelled by electric field toward the bulk and physically separated from the electrons, which will be mobilized to the interface of the semiconductor electrode and made available for reactions with the solution (*Figure 2.16*b).

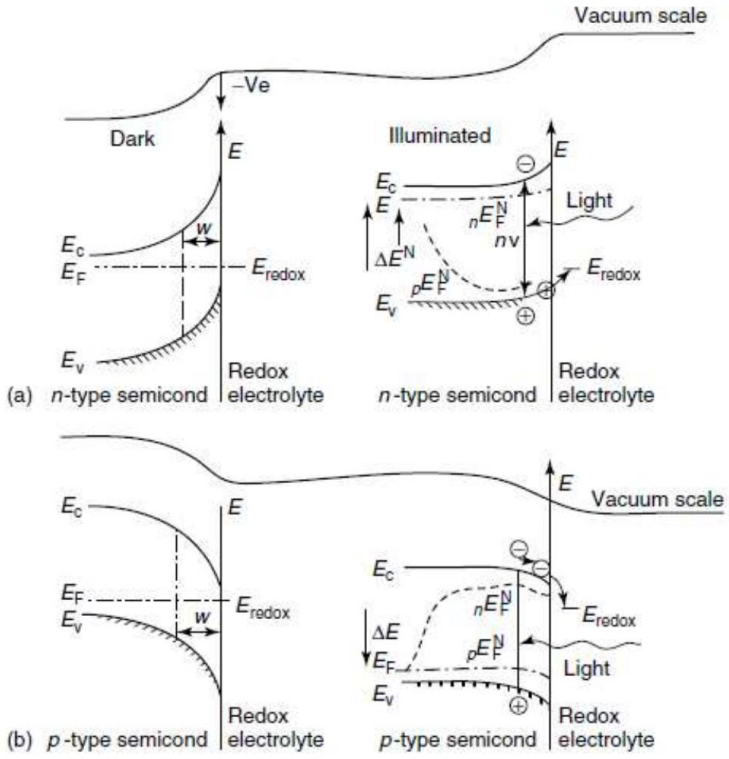

Figure 2.16. *Photogeneration of electron-hole pairs in the field-free region and depletion layer for a) n-type semiconductor and (b) p-type semiconductor. Taken from Ref. [29].*

Assuming light illumination from the electrolyte side, for an n-type semiconductor the electron-hole pairs are optically generated, both in the field-free and in the space charge regions within the semiconductor [29].

The absorption coefficient for this process is given by:

$$\alpha = A\frac{(h\nu - E_g)^n}{h\nu} \quad \textbf{(2.28)}$$

where *A* is a constant, and *n* is a constant which depends on nature of optical transition (*n*=1⁄2 for direct transition and *n*=2 for indirect transition) [29]. The type of optical transition depends on the respective positions of the valence band maximum and the conduction band minimum. *Figure 2.17* shows the corresponding band structures of a direct (a) and indirect (b) semiconductor. In direct semiconductors the transition requires only the absorption of a photon. In contrast, indirect semiconductors require the change in both energy and momentum, the latter being achieved by absorption or emission of a phonon (a quantum of lattice vibration). The indirect transition is a two-step process and hence it is less probable than a single- step direct transition, which typically leads to higher absorption coefficients for direct semiconductors as compared to indirect ones.

The transition (e.g. induced by a photon) of an electron from the conduction band to the valence band in the direct semiconductors occurs with energy conservation ($E=E_g$). On the other hand, in the indirect semiconductor, the transition conduction-to-valence band requires an additional energy E_p ($E=E_g + E_p$). The lattice vibrations called phonons provide this additional energy.

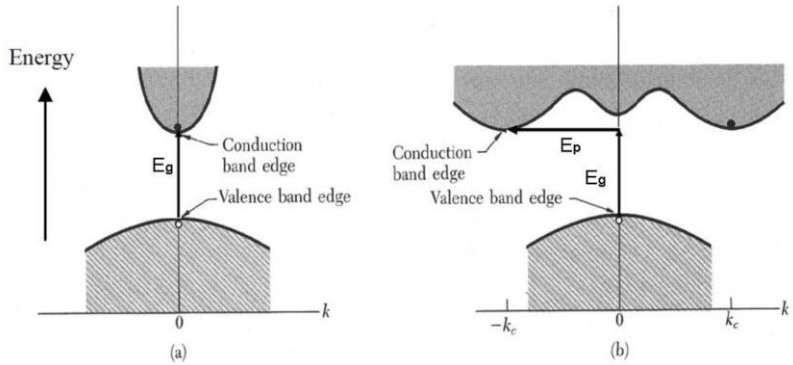

Figure 2.17. *Schematic view of an allowed direct a) and b) an allowed indirect optical transition. Taken from Ref. [29].*

Figure 2.18 shows the difference between the absorption behavior of a direct and indirect semiconductor. The phonon is either created by the absorption process or, if the temperature is high enough, the lattice is already thermally excited in the crystal.

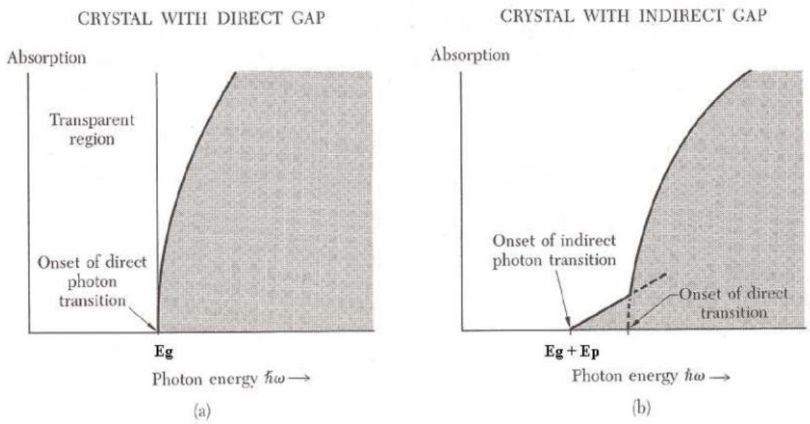

***Figure 2.18**. The absorption edge of (a) a direct semiconductor and (b) indirect semiconductor. Taken from Ref. [29].*

In principle, the charges contributing to the photocurrent can be generated either in the depletion (space charge) layer or in the diffusion layer (the length of diffusion layer is LP), that refers to the photogenerated carriers which diffuse to the space charge region. The electron/hole pairs generated at depths longer than the Debye length, L_D (L_D=W + L_p) will simply recombine. Thus, the effective quantum yield for a given interface will depend on the relative magnitudes of L_D and the light penetration depth, $1/\alpha$ [29].

Gartner, proposed a model to quantify the photocurrent response in a *n-p* junction. Gerischer noted that the junction between the semiconducting electrode and the electrolyte closely resembles to a Schottky barrier between a semiconductor and a metal. Subsequently Butler used this analogy to adapt this model to a semiconductor–electrolyte junction. This model considers that all carriers generated in the depletion region contribute

to the photocurrent, then no recombination process takes place in this region [29]. The corresponding component of this process is given by:

$$\boldsymbol{I_{dep} = q\int_0^W g(x)dx = -q\varphi_0[exp(-\alpha W) - 1]} \quad \textbf{(2.29)}$$

where *W* is the depletion-layer width given by:

$$\boldsymbol{W = W_0(E - E_{fb})^{1/2}} \quad \textbf{(2.30)}$$

W_0 is the depletion layer width for a potential of 1 V across it, E is the applied potential relative to a reference electrode, and E_{fb} is the flat-band potential, measured respect to the same reference electrode.

$$\boldsymbol{W_0 = \left(\frac{2\varepsilon}{qN_D}\right)^{1/2}} \quad \textbf{(2.31)}$$

The contribution of diffusion to the current is obtained by solving the diffusion equation for holes with suitable boundary conditions. Following arguments of Gartner, $p=p_o$ at $x=\infty$ and p=0 at $x=W$, i.e. the surface concentration of minority carries is zero. Hence, the diffusion current, is given by:

$$\boldsymbol{I_{diff} = q\varphi_0 \frac{\alpha L_p}{1+\alpha L_p} exp(-\alpha W) + qp_0 \frac{D_p}{L_p}} \quad \textbf{(2.32)}$$

where L_p is the hole diffusion length, D_p is the hole diffusion constant and p_0 is the equilibrium hole concentration with no illumination. For wide band gap the last term in equation 2.32 can be neglected. Combining the expressions, the following relation is obtained

$$\boldsymbol{I_{ph} = q\varphi_0\left(1 - \frac{exp\left[-\propto W_0(E-E_{fb})^{1/2}\right]}{1+\propto L_p}\right)} \quad \textbf{(2.33)}$$

This equation describes the behavior of the photocurrent as a function of the carrier density, diffusion length, applied potential, flat-band potential, and wavelength of incident light [29].

The quantum yield (Φ) can be obtained normalizing equation 2.33 as follows:

$$\boldsymbol{\phi = \frac{I_{ph}}{q\varphi_0} = \frac{exp(-\alpha W)}{1+\alpha L_p}} \quad \textbf{(2.34)}$$

Equation 2.35 displays the effective quantum yield, given by the ratio of the photocurrent density I_{ph}, and the incident light flux, ($q\varphi_o$).

A very useful parameter to study the quantum efficiency is the incident photon to current conversion efficiency, known as IPCE. Also called external quantum efficiency, IPCE is a measurement of the effectiveness in converting photons incident on the cell to photocurrent flowing between the working and counter electrodes. Thus, the maximum value of IPCE (100%) means that all photons generate electron/hole pairs. However this is not a real case, because of the losses corresponding to the reflection of incident photons, their imperfect absorption by the semiconductor, the recombination of the photogenerated charge within the semiconductor, *etc* [38].

$$\boldsymbol{IPCE = \frac{I_{ph}}{eF\lambda} = \left(\frac{hc}{e}\right)\left(\frac{I_{ph}}{P\lambda}\right) = 1240\,\frac{I_{ph}}{P\lambda}} \quad \textbf{(2.35)}$$

where I_{ph} and P are the photocurrent density (A/m^2) and the incident power density of light (W/m^2), respectively, at wavelength λ (m) and c is the speed of light ($3 \cdot 10^9$ m/s).

IPCE is calculated by measuring the current in a cell when a particular wavelength or a small group of wavelengths (bandpass, usually up to 12 nm) with a known power density P is incident on it. It is usually measured at a bias voltage corresponding to the maximum power point.

2.3.3.1 Nanostructured semiconductors: Photoinduced process in semiconductor-electrolyte interface

As seen before, the immersion of a semiconductor into an electrolyte generates the equilibration between the Fermi levels of the two contacting phases. For a compact semiconductor electrode, after Fermi levels are

adjusted, the space charge layer is formed and the separation of the photogenerated charges is controlled by the built-in potential gradient in the space charge layer. However, the formation of a space charge layer in a nanocrystalline semiconductor can be questionable due to the small particle size. When very low particle size materials are used, the charge separation is mainly determined by the differential kinetics at the semiconductor electrolyte interface and the semiconductor substrate interphase [29,39,40]. *Figure 2.19* contains a schematic representation of mechanisms of photogeneration of charge carriers and transport of electrons in nanocrystalline semiconductor-electrolyte interphase. Because the size of particles, differently from compact semiconductor electrodes, the electrolyte can penetrate the whole film, and thus impregnate all the particles, as in a colloidal system [29,38]. Thus electrolyte/semiconductor junction occurs at each nanocrystal. During illumination, light absorption in any individual colloidal particle will generate electron-hole pairs. Assuming the case of *n*-type semiconductor, the kinetics of charge transfer to the electrolyte is much faster for holes than the recombination processes, and thus holes are rapidly scavenged by the electrolyte redox species at the surface of the particles. In contrast, the photogenerated electrons can create a gradient in the electrochemical potential between the particle and the back contact. In this gradient, the electrons can be transported through the interconnected particles to the back contact.

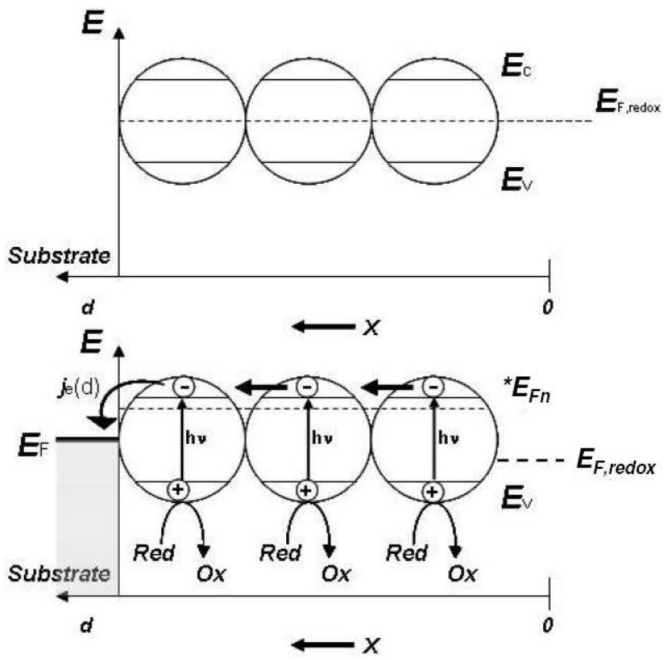

Figure 2.19. *Schematic representation of the model of the charge carrier separation and charger transport in nanocrystalline film for an n-type semiconductor immersed in redox electrolyte. The holes transfer to the electrolyte, and the electrons traverse several crystallites before reaching the substrate. Taken from [29].*

It must be noted that the possibility for electron recombination will depend on the distance between the photoexcited particle and the rear contact, and thus it is clear that there will be an increased probability of recombination with increasing film thickness [29,41,42]. Thus, the competition between surface recombination of photogenerated electrons and holes, and collection at the rear contact dictates the magnitude of the quantum yield.

2.4 Semiconducting metal oxides

Since their properties can be modified over a wide range, semiconducting metal oxides are promising materials for the synthesis of nanostructured photolectrodes, which can be used as anode, cathode or both in the photoelectro-chemical water splitting process.

Moreover, these materials are economically promising because their processing technologies are relatively simple. In the context of hydrogen production, the band gap of the most common metal oxides is wide enough to allow the photochemical water splitting. However, the choice of possible materials becomes limited when their stability is considered: unfortunately, most of them, such as for example Fe_2O_3 (E_g = 2:3 eV), and GaAs (E_g = 1:4 eV), are not very stable and exhibit significant corrosion in water.

Among the others, TiO_2 and WO_3 have been selected for the present investigation because they represent a good alternative either in terms of stability to corrosion and photocorrosion, as well as low cost, high availability, and low toxicity.

2.4.1 TiO_2

TiO_2 is one of the most encouragin photocatalyst for the fabrication of a commercial PEC cell for the production of H_2 from water [43]. When TiO_2 is irradiated with photons whose energy matches or exceeds the band gap energy of TiO_2, electron/hole pairs are photogenerated. Then, the photogenerated charges migrate to the surface, where the redox reactions take place with the chemical species adsorbed on the TiO_2 surface. If an electrolyte aqueous solution is considered, water molecules are reduced by electrons to form H_2 at the cathode while at the TiO_2 photoanode water molecules are oxidized by holes to form O_2 [44–47].

In order to have a general picture of the different factors that can influence the PEC performance of TiO_2 based photoanodes, some relevant aspects of this material will be explained in the following sections.

2.4.1.1 TiO_2 properties

Titania belongs to the family of transition metal oxides. This material is sensitive to the radiation and in excited states it reacts with water molecules.

As explained before, when the semiconductors are irradiated electrons are excited from the semiconductor valance band (VB) to the conduction band (CB) with leaving a hole (h^+) in the VB. The oxidizing power of the h^+ often destabilizes the semiconductor material itself, which limits the applications of semiconductor photocatalysts. In this respect, titania is an excellent material that exhibits good photocatalytic activity and stability under both dark and irradiation conditions [48,49]. A fraction of photogenerated h^+ (the ones who do not recombine with electrons) diffuse to the semiconductor surface where they can react with the electron donor species. This process is the main driving force of most photocatalytic oxidation processes [49].

The h^+ oxidation potential is essentially equal to the VB edge potential and depends on the kind of semiconductors. In general, wide bandgap semiconductors have highly positive VB potentials. In particular, the VB edge of TiO_2, which lays around 2.7 V vs. NHE at pH 7, induces the generation of strongly oxidizing h^+ under UV irradiation. The VB positions of metal oxide semiconductors like TiO_2 are usually similar among themselves because the VB mainly consists of the O 2p orbital that is a common component of oxide materials [48–51].

However, TiO_2 is unique not only in its highly oxidizing VB hole but also for its main well-known characteristics, which are reported below:

- It is a thermodynamically stable material against the corrosion and the photo-corrosion in aqueous solutions at any pH.
- TiO_2 is not soluble in aqueous solutions (in alkaline or acid solutions).
- It is an abundant and economically accessible material.
- This material presents a low toxicity.

On the other hand, although the VB holes and OH radicals are the main active species in most photocatalytic oxidation processes, their roles are

effective only when the electrons at the CB are also efficiently transferred on the semiconductor surface (or to the counter electrode in PEC systems, where the reduction take place). Otherwise, the accumulation of electrons at the CB of titania results in the fast recombination with h^+ in the VB or the surface-bound OH radicals, which in turns reduces the overall photocatalytic efficiencies.

TiO_2 exists under three main crystalline phases: rutile, anatase and brookite. All three forms occur naturally but the latter is rather rare and has no commercial interest [44].

The structure of rutile (tetragonal, a = b = 4,584 Å, c = 2,953 Å), anatase (tetragonal, a = b = 3,782 Å, c = 9,502 Å) and brookite (orthorhombic, a = 5,436 Å, b = 9,166 Å, c = 5,135 Å) can be analyzed in terms of octahedrals (TiO_6^{-2}) [52], where the basic building block consists of a titanium atom surrounded by six oxygen atoms. These crystal structures differ by the distortion of the octahedric units and by the assembly patterns of octahedral chains [53]. *Figure 2.20* displays the bulk structures of anatase, brookite and rutile. As observed, in the case of anatase, the octahedric units are united by the vertices. For rutile only the edges are connected, and in brookite both, edges and vertices are connected.

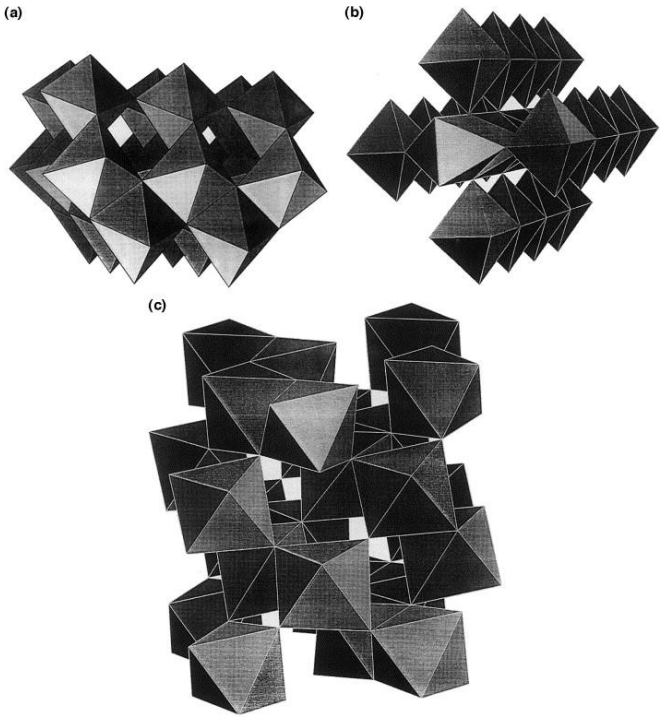

Figure 2.20. *Crystalline arrangements of (a) anatase, (b) rutile and (c) brookite.*

A schematic representation of an ideal TiO_2 structure, formed of Ti^{4+} and O^{2-} ions, is shown in *Figure 2.21*. However, such ideal crystals are not stable thermodynamically due to a configuration entropy term that requires the formation of point defects [54]. Thus, titania can be considered a non-stoichiometric compound [54]: both oxygen vacancies and Ti interstitials are generally considered as predominant defects [54,55]. According to this approach the apparent oxygen deficit is more correctly interpreted as a combination of oxygen vacancies and Ti interstitials. A simplified representation of the lattice structure is shown in *Figure 2.22*, involving different kinds of point defect, including ionic defects.

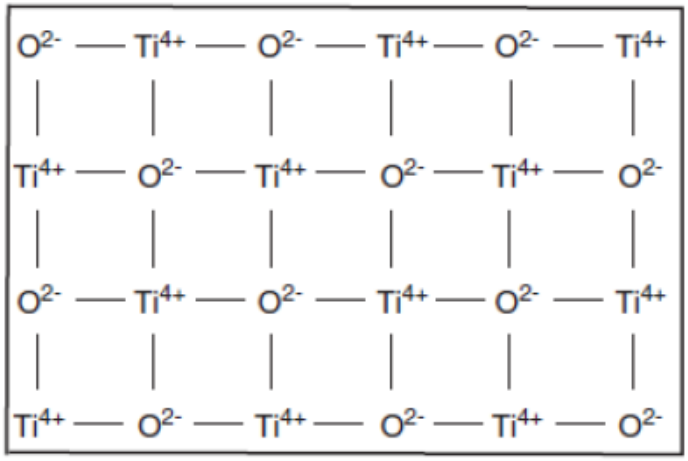

Figure 2.21. *A schematic representation of an ideal TiO_2 structure.*

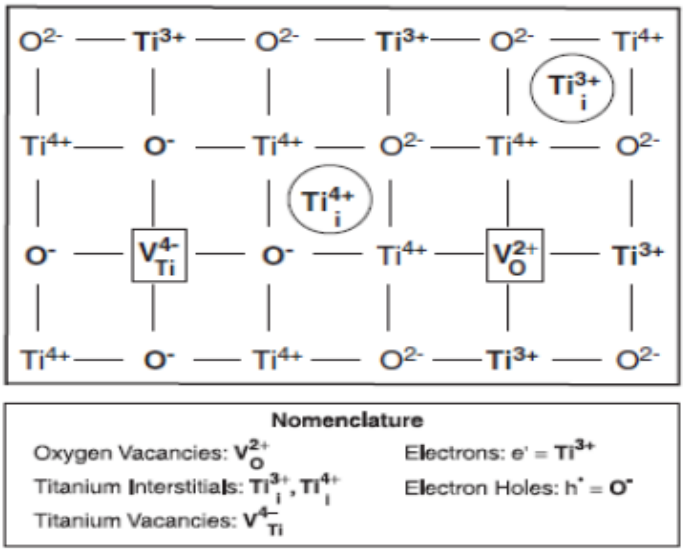

Figure 2.22. *A simplified representation of the TiO_2 lattice structure.*

Oxygen vacancies and titanium interstitials, which are donors of electrons, well explain n-type properties of TiO_2. The defect structure varies with oxygen deficiency, which depends on temperature, gas pressure, impurities,

etc. However, it is not still clear which type of defect is dominant in which region of oxygen deficiency, being nowadays subject to debate [56]. It has been recently shown; however, that TiO_2 is an amphoteric semiconductor that exhibits n-type and p-type properties at low and high oxygen activities, respectively. These properties cannot be explained by the presence of oxygen vacancies and titanium interstitials as the only ionic defects in TiO_2.

From a photochemical point of view, band gap is one of the most important differences between the three phases, being it 3.4, 3.2 and 3 eV for brookite, anatase, and rutile, respectively. Thus photocativity of rutile is observable up to 415 nm, whereas the other two phases can be excited by radiation of maximum wavelength of about 387 and 365 nm for anatase and brookite, respectively. However, photoactivity of anatase is generally reported to be better than that of rutile.

The above reported values of band gaps are in any case wide enough to allow water splitting, at least from a theoretical point of view.

However, the utilization of TiO_2 remains confined to UV light, and a very low efficiency is obtained when the photochemical processes are performed under solar radiation. In fact, it must be considered that UV irradiation represents only a little fraction of the solar spectrum and semiconductors like titania, with band gap of the order of 3 eV can exploit just about 10% of the total solar energy incident on them (see *Figure 2.23*).

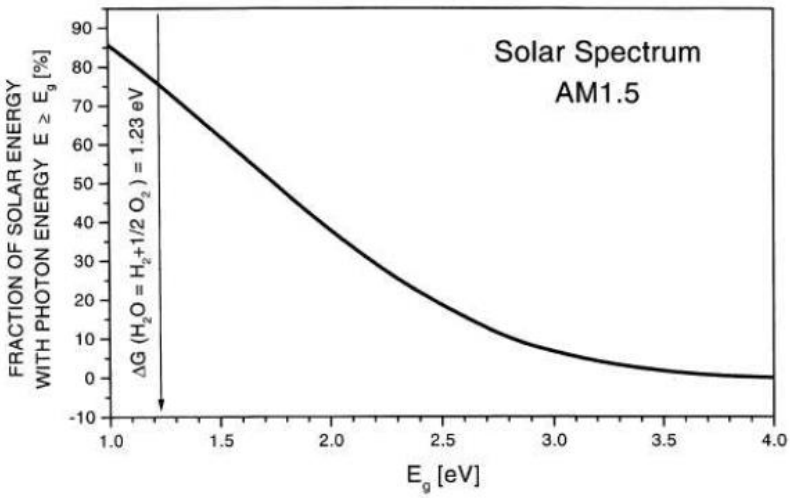

Figure 2.23. *Fraction of solar spectrum used efficiently for generation of electron / hole pairs vs band gap.*

Shifting the photoresponse of titania into the visible range might therefore enhance its potential for photoelectron-chemical solar energy conversion and open possibilities for further applications [57]. So, modification of the functional properties of TiO_2 becomes essential in order to increase the energy conversion efficiency to the level required for the possible commercialization of this material.

2.4.1.2 TiO_2 nanostructured electrodes: Preparation techniques

The use of TiO_2 nanostructured materials increases the surface area and also enhances the concentration of available surface active sites, thus leading to higher photocatalytic activity. However, an increase in the surface area may increase the number of surface defects, which are known as e^-/h^+ recombination centers. Therefore, an optimization of the crystallinity and of the TiO_2 particle size and morphology is usually required to achieve high efficiencies of the PEC cell [44,45,58]. Until now, a large variety of morphologies of TiO_2 nanostructures, such as nanoparticles, nanorods, nanowires, mesoporous structures or nanotubes have been tested as well as diverse synthesis.

The interest in the application of the nanotechnology, as synthesis method, in the field of the PEC cells lies in the fact that a photoelectrode synthesized using the nanotechnology could significantly increase the efficiency of a photelectro-chemical cell. This could be due to the high real surface area of the nanostructured material, which is in contact with the solution; this fact allows a greater absorption of the incident radiation on the nanostructured surface of the electrode and also the electrode presents a larger surface area available to carry out the process of charge transfer with the electrolyte solution.

Numerous techniques for the preparation of nanostructured electrodes are reported in the literature, such as the mechanical activation by energy ball-milling or the electrospinning to obtain nanofibers. In this thesis, the electrochemical oxidation method (anodization) was adopted in order to obtain different TiO_2 nanostructures (compact oxide or nanotubular structures). In the specific, the formation of either compact or nanotubular structures, by anodization of titanium foils, will be described in the next section.

2.4.1.3 Electrochemical oxidation to obtain TiO_2 nanotubes

Nanotubes of TiO_2 have become commonly used structures for photoelectro-chemical applications because nanotubular architecture, being ordered and strongly interconnected, eliminates randomization of the grain network and increases contact points for good electrical connection [59]. Vertically oriented self-organized nanotubes formed by electrochemical anodization improve the orthogonalization of charge separation and charge transfer. Moreover, the nanotubes architecture constitutes a sort of light “trapping scheme”, whereby the incident light must pass through the sample multiples times before escaping, substantially increasing the probability it is absorbed [60].

The generation of self-ordered nanoporous structure for TiO_2 was reported for first time by Kelly and co-workers [61], which indicated the formation of a nanoporous structured during anodization of Ti in NaF containing electrolyte. The particular advantages of regular tube arrays such as the large surface area or the defined geometry stimulated the use of nanotubes

for a wide range or functional applications. In fact, a high attention has been paid on TiO_2 nanotubes as can be deduced for the strong increase of the publications about the TiO_2 nanotubes.

In the most used approach, the process of formation of TiO_2 nanotubes is governed by the equilibrium between two reactions: the continuous anodic growth of a compact oxide layer on the metal surface (equation 2.36) and simultaneous chemical dissolution of the oxide as consequence of the generation of soluble fluoride complexes (equation 2.37).

$$\boldsymbol{Ti + 2H_2O \rightarrow TiO_2 + 4H^+ + 4e^-} \quad \textbf{(2.36)}$$

$$\boldsymbol{TiO_2 + 4H^+ + 6F^- \rightarrow [TiF_6]^{2-} + 2H_2O} \quad \textbf{(2.37)}$$

In the specific, the formation of a compact oxide layer occurs, as consequence of the reaction of metal species with O^{-2} ions from H_2O (*Figure 2.24a*). As the system is under constant applied voltage, the field within the oxide is progressively reduced by the increasing oxide thickness, the process is self-limiting.

In the presence of fluorides, the situation changes mainly due to two phenomena:

- The attack and dissolution of the formed TiO_2 oxide, by the generation of a soluble complex (TiF_6^{-2}, *Figure 2.24b*)

- The fluorides penetration in the TiO_2 lattice, that is possible for the small ionic radiuses, which are suitable to be transported through the oxide by the applied field, competing with the O^{-2} transport.

It should also be noted that in absence of fluoride ion, a titanium hydroxide compound could precipitate as consequence of the transport of Ti^{4+} ion at the oxide electrolyte interface (*Figure 2.24a*). However when fluorides are present in solution, they can establish a constant chemical attack, preventing the formation of the $Ti(OH)_xO_y$ precipitate [62–66].

Figure 2.24c shows also the current transient phases with (continuous line) and without fluorides (discontinuous line) in the electrolyte during the anodization process. Analyzing the whole process step by step, it is possible

to relate the different phases in the current transient to physic phenomena in the oxide/electrolyte interface:

• Stage I: Oxide layer formation. A current decay occurs as result of the formation of the oxide barrier, following the current trend of the high field oxide formation process. (phase I in figure 2.24c)

• Stage II: Dissolution of TiO2. The attack of F- ions allows the activation of the surface, and consequently the random formation of the first pore structure. The pores grow, increasing the active area and thus also the current increases (phase II in figure 2.24c). After a time, the permanent dissolution of the TiO2 leads pores to reach a certainly depth.

• Stage III: Formation of self-organized nanotubes. As the process goes on, a new situation in which current becomes equal for all pores, and self-order under steady state conditions is established (phase III in figure 2.24c). The current has reached a plateau because of a steady state condition.

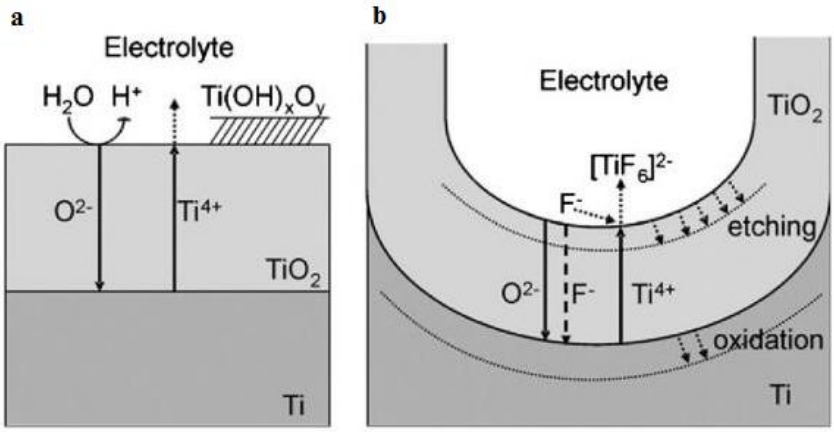

(Scheme of Ti anodization, figure 2.24)

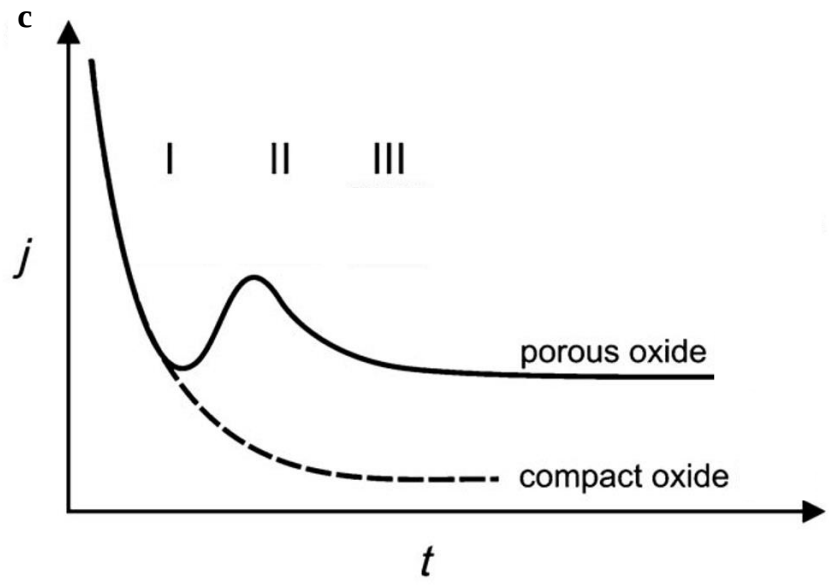

Figure 2.24. *Scheme of Ti anodization: (a) in absence of fluoride ions and (b) in presence of fluorides. Taken from Ref.[131]. (c) Typical current-time (j-t) characteristics after a voltage step in the absence (discontinuous line) and presense (continuous line) of fluoride ions in the electrolyte. Typical Current transient phases (I-III) are also depicted in figure. Adapted from [168].*

The equilibrium state is established when the pore growth rate at the metal oxide interface is identical to the thickness reducing dissolution rate of the oxide film at the outer interface (an equilibrium is reached between the involved reactions). At this point a limiting value of current density is observed (Figure 2.24c), after a certain anodization time. In this situation the nanotubes oxide layer is only continuously dissolved through the titanium substrate without thickening of the oxide layer. Even prolonged anodization does not increase the tube layer thickness significantly.

The nanotube layers, as they are grown in fluoride containing electrolytes, show a U-shaped sidewall thickness profile that is due to exposure of the formed tubes to the etching fluoride-containing electrolyte (permanently etching and thinning the tube walls). As reported in literature[TiO2 Nanotubes: Synthesis and Applications Poulomi Roy, Steffen Berger, and Patrik Schmuki], the outer part of the nanotube is typically dense very pure TiO_2, and the inner part of the tube is made of a more loose nature and contains incorporated electrolyte

components. Several SEM studies [TiO2 Nanotubes: Synthesis and Applications Poulomi Roy, Steffen Berger, and Patrik Schmuki] showed that chemical dissolution of the inner TiO_2 layer is faster and thus contributes more to the fact that the walls become thinner towards the top of nanotubes.

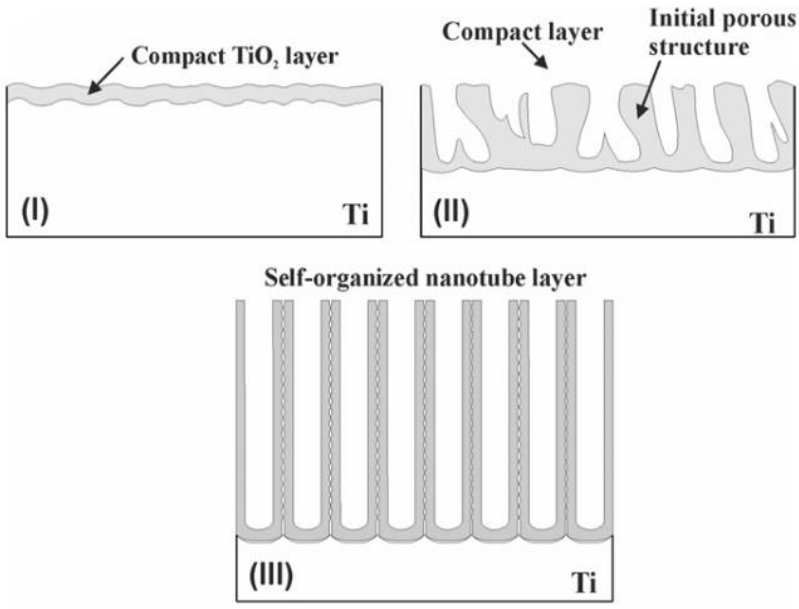

Figure 2.25. *Scheme of the phases involved in the nanotubes formation. I: compact TiO_2; II:formation of etching grooves; III: sensitized tubes.Taken from Ref. [169]*

Considering the information reported above, it should be noted that the controlling factors of the process are the concentration of fluoride ions and the applied potential, because they are directly related with the dissolution and oxidation reactions.

Although in this thesis only the anodization has been used as the technique to prepare nanotubes, also they can be produced by a variety of different methods including hydrothermal synthesis [65,67], deposition into porous alumina templates [63,68], and the seeded-growth mechanism [69]. Despite the advantages of these methods, none is able to produce self-organized

nanotubes, allowing to tutoring the geometry and dimensions as anodization method does. For this reason, this methodology has been used to prepare and study self-organized TiO_2 nanotubes for photoelectrochemical applications.

2.4.2 WO_3

This section summarizes the recent developments of nanostructured WO_3 thin layers synthesized by cathodic electrodeposition for their application in PEC water splitting. The key fundamental reaction mechanisms of cathodic electrodeposition methods for the preparation of nanostructured WO_3 thin layers will be described. Finally, the effect of some of the most relevant synthesizing parameters on the size, composition and photoresponse of the WO_3 layers will be also reported.

2.4.2.1 WO_3 properties

Compared to titania, WO_3 is characterized by a smaller band gap energy (2.6 eV). Therefore, this material is capable of increased the absorption in the visible light region (about 12% of the solar spectrum) [70,71]. To date, WO_3 has been reported in a number of studies as a new generation photocatalyst for PEC water splitting.

Thermodynamically, WO_3 is reported to be stable in acidic environments (in strong acidic electrolytes, tungstate cations may be formed) [72]. The potential–pH equlibrium diagram (Pourbaix diagram), considering the tungstic ion WO_4^{2-} and the solid substances W, WO_2, W_2O_5 and anhydrous WO_3 are reported in *Figure 2.26*.

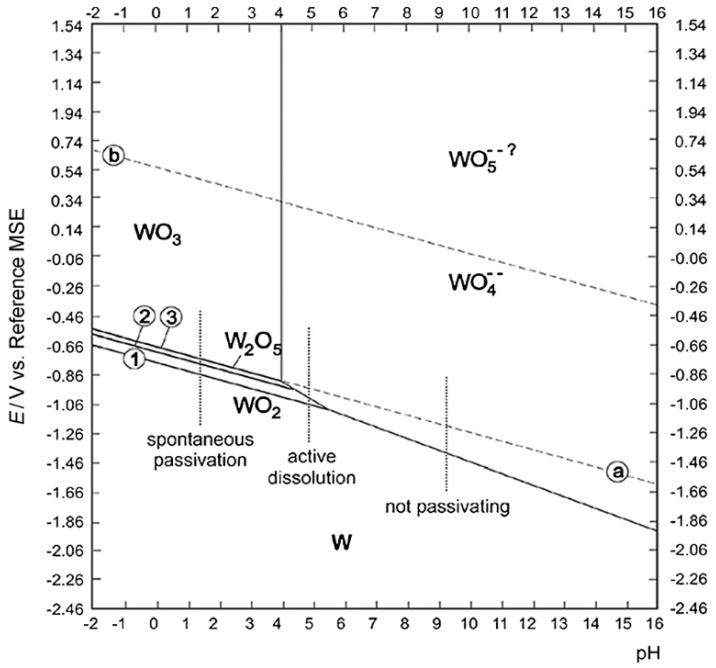

Figure 2.26. *Potential-pH equilibrium diagram for the system tungsten-water, at 25 °C. Taken from Ref. [71].*

The Pourbaix diagram shows the potential at which chemical and electrochemical reactions may occur on an electrode surface in a specific electrolyte as a function of the pH value [73]. From the Pourbaix diagram the thermodynamic stability of chemical species at various potentials and pH ranges can also be determined. Tungsten forms a wide range of oxides, and WO_3 is the most stable. Other oxides formed with W are mostly the results of thermal oxidation of W or reduction of WO_3. According to the Pourbaix diagram, the W surface at pH equal to 2 should be passivated through the formation of WO_2, W_2O_5, or WO_3 [71].

Many researchers have studied the dissolution of tungsten oxides in acidic solution, but thus far no general agreement on the mechanism has been found. Some authors, proposed a dissolution model for W in acidic solutions through the formation of intermediate species such as WO_2^{2+}. For pH > 1, passive dissolution of W can occur owing to the conversion of species more stable than WO_2^{2+}, such as WO_4^{2-}. Other authors, investigated

the influence of the pH value on the anodic behavior of W. They suggested that at pH 1 and pH 2.6, which corresponds to the point of zero charge of the WO_3 surface, both H^+ and H_2O would assist in WO_3 dissolution. When approaching pH 2.6, the contribution of H^+-assisted dissolution diminishes. [71PhD]

The cathodic electrodeposition of WO_3 is generally considered a cost effective synthesis method for the preparation of stoichiometric nanostructured WO_3 thin films [74]. This method, which is versatile and can be performed at room temperature, is widely used to prepare advanced nanostructured WO_3 thin films [71,75–78]. The nanostructured WO_3 films can be tailored to exhibit desirable physical and chemical properties by varying the electrochemical synthesis parameters, such as metal oxide precursor, electrode substrate and morphology, applied potential and current density, and annealing temperature [71,79].

Figure 2.27 shows a typical scheme of the cathodic WO_3 electrodeposition method in a three-electrode cell.

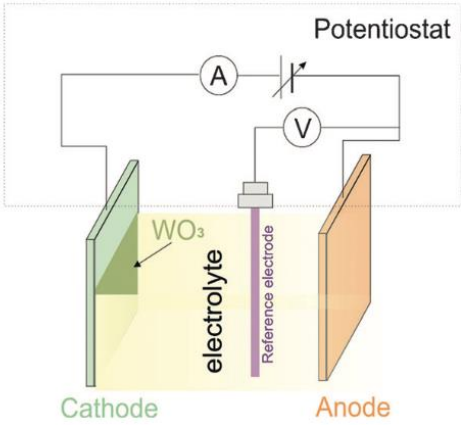

Figure 2.27. *Cathodic electrodeposition method for synthesizing WO_3 thin films, where the cathode usually uses FTO or ITO as electrode substrate whereas Pt is employed as the anode. (Taken from [71])*

During the cathodic electrodeposition method, two different mechanisms can occur: the direct reduction of the tungsten oxidation state and its deposition on the electrodes and/or the precipitation of the tungsten oxide due to the generation of a localized high pH region in the electrode

/electrolyte interface, which induces the electrodeposition of metal ions [80].

The formation of the tungsten peroxo precursor ($W_2O_{11}^{2-}$), which is used in this Thesis as a component of the tungsten oxide deposition solution, and the cathodic WO_3 electrodeposition mechanisms are described by the reactions reported in equations 2.38 and 2.39, respectively [81].

$$\boldsymbol{2W + 10H_2O_2 \rightarrow W_2O_{11}^{2-} + 2H^+ + 9H_2O} \quad \textbf{(2.38)}$$

$$\boldsymbol{W_2O_{11}^{2-} + (2+x)H^+ + xe^- \rightarrow 2WO_3 + (2+x)/2H_2O + (8-x)/4O_2} \quad \textbf{(2.39)}$$

where $W_2O_{11}^{2-}$ corresponds to $[(O_2)_2W(O)OW(O)(O_2)_2]^{2-}$ and (O_2) represents a peroxide ligand [82].

Some authors only link the increase in efficiency of nanostructured tungsten oxide films with a good approximation by the reduction of peroxy tungstate [81]. However, this theory may contradict that of many other metal oxides, which are usually based on both the mechanisms discussed above (electrodeposition and precipitation).

2.4.2.2 Effects of the synthesis conditions on the morphology of WO_3 nanostructures

This section summarizes the effects of metal oxide precursors, electrode substrates as well as annealing temperatures on size, composition, and photoresponse of the WO_3 thin layers, when the electrochemical synthesis is considered as route to obtain the tungsten oxide nanostructures.

Effect of the metal oxide precursor

The metal oxide precursors employed in the electrochemical synthesis of the tungsten oxide layers, can significantly influence the morphology of the

WO_3 nanostructures. As an example, Shen et al., [83] assessed that when the WO_3 is electrodeposited from alcoholic solutions, the obtained layers are more stable than those synthesized in solutions without alcohols.

Severeal papers also report the influence of the precursor solution composition on the electrodeposition efficiency: Kondrachova et al. found that the efficiency of electrodeposition from a peroxo-poly-tungstate solution strongly depended on the composition of the precursors [84]. Other authors [85], also found that the pH value of precursors played an important role in modifying the surface morphology of nanostructured thin layers; two different layer types were obtained at three different pH values [85]. A mesoporous WO_3 layer formed when performing the electrodeposition under cyclic voltammetry from a strongly acidic solution (at pH = 0.8, which was adjusted by using H_2SO_4); the same authors found that 0.8–1.1 was the optimum pH range to prepare mesoporous WO_3 layers, while in the absence of H_2SO_4 transparent WO_3 layers were electrodeposited from precursor solution with a pH equal to 1.92. When the photoactivity of the layers were compared, the authors reported that the nanoporous WO_3 synthesized under the optimum pH conditions gave rise to photocurrent densities nearly three times that of transparent nanoporous [71,85].

Effect of the electrode substrate

Several conductive electrode substrates have been reported in literature as electrodeposition platforms to provide an effective growth of nanostructured WO_3 thin films. In general, it can be summarized that the electrode substrate can influence the final electrodeposition efficiency.

Moreover, the morphology of the structure of the substrates has an impact on the eventual size, shape, and efficiency of the WO_3 deposit. Therefore, understanding the impact of the surface structure of chosen electrode substrates during the electrodeposition process are essential to achieve a more uniform particle size and better dispersion of photocatalyst particles [86].

Different authors have been studied the effects of the electrode surface on both the electrodeposition efficiency and the photo performance of binary

systems. Shen et al. synthesized WO_3 layers by performing the electrodeposition method on various electrode substrates including Au or Pt foils and indium tin oxide (ITO) coated glasses [83]. The authors found that the highest surface coverage of WO_3 at the same current density and deposition charge was achieved on ITO coated glass, followed by Au foil. The least coverage was obtained on the Pt foil. Baeck et al. [87] also synthesized WO_3 films by pulsed electrodeposition on Ti and ITO coated glass electrodes. When comparing the cathodic current deposition, the nanocrystalline WO_3 layers on Ti electrodes showed significantly higher current densities [87].

If the photoactivity is considered, other authors, prepared WO_3 layers on polished Ti foils that showed a considerably enhanced photocurrent compared to WO_3 layers deposited on unpolished and preoxidized Ti foils [88]. This finding suggested that the in situ formation of a thin tungsten oxide–titania interfacial composite layer and a good adhesion of WO_3 to the polished Ti foil played an important role in enhancing the photoresponse [71,88].

Effect of the anneling temperature

To transform the structure of the electrodepositd WO_3 layer (electrodeposited on the electrode substrate) into a crystalline structure, an annealing treatment is required. Such a transformation usually occurs at the expense of decreasing surface area and active sites for subsequent photocatalytic reactions. It is also considered that depending on the annealing temperature, at which the electrodeposited WO_3 layer is submitted, different phase transitions occur. After the electrodeposition process, the WO_3 film layers could be transformed into a monoclinic structure by thermal annealing [90]. Ng et al. studied the relation between the crystallinity degree of WO_3 electrodes and the annealing temperature. They determined that the photocurrents and charge stored changed with the WO_3 crystallinity degree, which depends on the annealing time (*Figure 2.28* and *Figure 2.29*) [91].

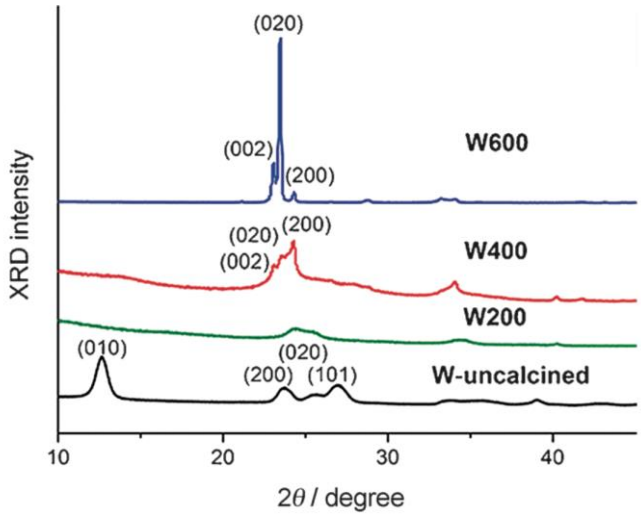

Figure 2.28. *XRD patterns of WO_3 films at different calcination temperature of 200, 400, and 600°C. Taken from Ref. [91].*

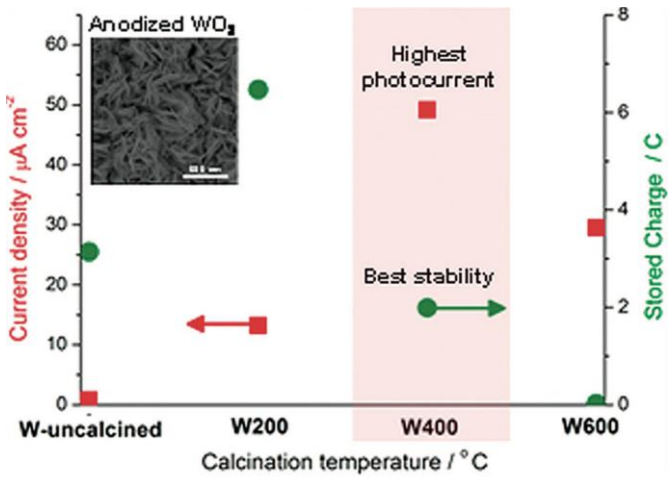

Figure 2.29*. Photocurrent response for compact and porous WO_3 layers. The inset shows the SEM image for anodized WO_3 layer. Taken from Ref. [91].*

Moreover, the change of the WO_3 structure from amorphous to monoclinic one (annealing temperature 500°C) was reported to significantly increase

the photocurrent conversion efficiency as well as decrease the band gap energy [92]. Other studies reported that the shift in absorption edge of tungsten oxide-titania nanoparticles depended on the synthesis method used and the nature of precursors but also on the type of the thermal annealing treatment [71,90].

Liu et al. [93] attributed the low photoactivity in annealed WO_3 thin layers to a low crystallization degree of the WO_3 samples. They observed that increasing the annealing temperature to 450°C, the photoactivity of the WO_3 thin layers was increased. Liu et al. linked this fact to a higher degree of crystallization of WO_3 and a decrease in surface defects. They also reported that 450°C was the optimum annealing temperature with the highest photoactivity and a reaction rate constant of 0.0459 min^{-1} for PEC water splitting. Any further increase in the annealing temperature beyond 450°C generated a deterioration in the photoactivity of the WO_3 layers. The same authors attributed the deterioration in photoactivity of the WO_3 layers to two main causes [93]. The first one was the formation of W_2N compounds in the WO_3 layers, which has a lower photoactivity, while the second one was the destruction of the nanoporous WO_3 films, which results in a decrease in photoactivity.

Another important factor to consider is the annealing time, which can also affect the properties of the WO_3 layers. As an example, Regragui et al. analyzed the effects of the annealing time on the structure and optical properties of tungsten oxide based layers [94]. They observed that the water content decreased significantly during annealing. Before the annealing treatment, FTIR spectroscopy and compositional measurements demostrated that the unannealed layers have hydroxyl groups on the surface where as water molecules are present in the bulk of the sample. During annealing, the hydroxyl groups are first destroyed and the water molecules leave the layer as the annealing time is increased: water evaporation during annealing results in a rough surface and causes the formation of defects; this results in an increase of light scattering as demonstrated by optical measurements. Therefore, a significant increase in light scattering was observed when the annealing time increased [71,94].

2.5 Binary semiconductor based materials: TiO_2-WO_3

The combination of two different types of semiconductors (hetero-nanostructured mixed metal oxides) has been usually considered as a method to improve charge pair separation and thereby to enhance the overall photocatalytic activity of single-phase photocatalysts [49,95,96]. An adecuate selection of the semiconductors based on their CB and VB positions leads to the cascaded transfer of photogenerated charge (electron/holes) from one semiconductor to another.

Compared to single-phase photo-catalysts, hetero-nanostructured mixed metal oxides can allow increasing the efficiency of separation of the charges and their lifetime, enhancing the light-response range to the visible region, as well as the interfacial charge transfer to adsorbed substrates. Actually, when the photoactivity of a composite-semiconductor structure is considered, not only the different band gap value, but also the reciprocal position of the energetic levels of VB band and CB have to be taken into account. In fact, depending on the wavelength, either only one or both the semiconductors can be activated by the incident radiation. Moreover, the reciprocal position of the band edges determines the possible transfer of holes or electrons from one to the other semiconductor. As reported in the literature, two possible cases could occur:

i. the incident photons are energetic enough to excite the semiconductor with the small band gap, but are not energetic enough for the material with the large band gap. In this case, photoexcited electron/hole pairs are only created in the CB and VB of the semiconductor with the smaller band gap.

ii. the energy of the light is high enough to activate both the semiconductors. In this case, a transfer of electrons and holes from one semiconductor to another occurs: a better separation of photogenerated charges may be achieved; electrons are accumulated at the lower lying CB of one semiconductor, while holes are accumulated at the VB of the other semiconductor.

Several binary systems consisting of TiO_2 and other semiconductors (e.g., WO_3, [97,98], CdSe, [99,100] and CdS [101]) have been prepared and tested for their photocatalytic activities. Among all the different

combinations, WO_3/TiO_2 combined photocatalysts have been frequently studied for environmental remediation and solar energy storage [98,102,103]. The role of WO_3 in the combined system is to accept the electrons of the TiO_2 CB: WO_3 has a lower (more positive) CB potential than that of the TiO_2, so that the TiO_2 CB electrons can be transferred to the WO_3 CB while holes are transfer to the TiO_2 VB. The electrons accumulated at the WO_3 CB can react with the surrounding electron acceptors (e.g., O_2) [98,104]. On the other hand, holes accumulated in the TiO_2 VB can react with electron donor spices in the solution (see *Figure 2.30*).

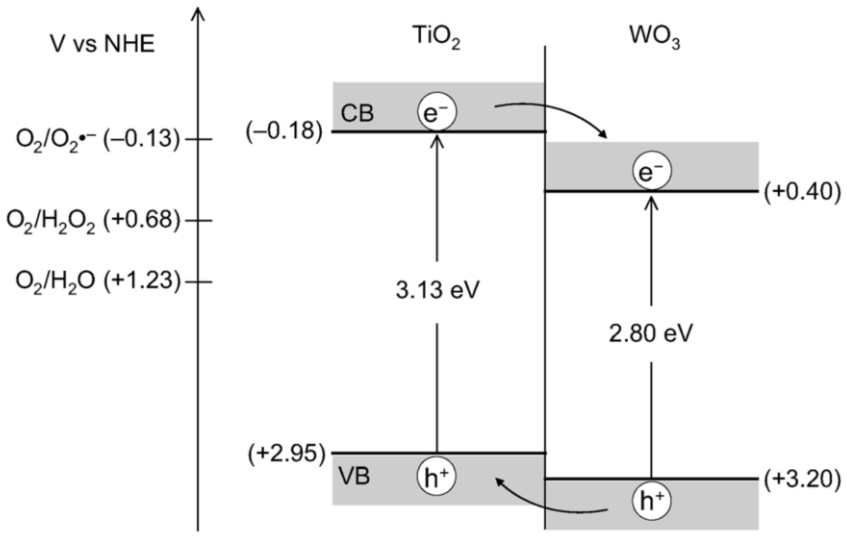

Figure 2.30. *VB and CB potentials for TiO_2 and WO_3. Charge transfer mechanism when the two semiconductors are photo-activated. Taken from Ref. [105].*

2.6 Charge kinetics in photocatalysis

As well known, in photocatalysis, charge kinetics is critical in determining the quantum efficiency of solar to chemical conversion. Charge kinetics includes the separation of photoexcited electron/hole pairs, utilization of

plasmonic hot carriers and transfer of photogenerated charges to reaction sites. In this section, the principles of various processes associated with charge kinetics that account for or may affect photocatalysis are introduced. Moreover, depending on the semiconductor system (bare semiconductors, metal-semiconductor or semiconductor-semiconductor juntions), different working mechanisms are also presented [106].

2.6.1 Bare Semiconductors

As explained in detail in section 2.3.1, the unique electronic structure of a semiconductor is mainly characterized by its valence band (VB), conduction band (CB), band gap (E_g), and Fermi level (E_f) [107]. The band structure is very important for a semiconductor-based photocatalyst, as it determines the light absorption properties as well as the redox capability of the semiconductor.

On the one hand, a semiconductor can only absorb the photons with energy equal to or greater than its E_g. During this process, the electrons in the VB are excited to the CB, leaving holes in the VB and generating electron–hole pairs. Once the electrons and holes transfer to the semiconductor surface, two half redox reactions can occur.

On the other hand, the reduction and oxidation capabilities of photogenerated electrons and holes in a semiconductor are mainly determined by the edge positions of the CB and VB, respectively. Only when the energy levels of the VB and the CB of a semiconductor are more negative and positive than the redox potential of reduction and oxidation half reactions, respectively, can an overall photocatalytic reaction occur [107]. If one of the band edges (CB or VB) does not satisfy the requirement, sacrificial agents have to be used as substituted electron acceptors or donors to make the other half reaction happen. In the case that the reactions take place on the surface, the rates of the charge consumption are still greatly influenced by the differences between the band-edge positions and the reaction redox-potential levels without band bending being considered. The larger the differences, the higher are the rates [106].

2.6.1.1 Bare Semiconductors in PEC processes

In addition to what we discussed above, bare semiconductors in a PEC system behave differently in a direct photocatalytic system. As explained in section 2.2, a PEC process is a system that integrates photocatalysis with electrochemistry, thus showing different charge kinetics from a direct photocatalytic process [108–110]. The PEC system consists of a semiconductor electrode, a metal counter electrode and an electrolyte between the two electrodes (*Figure 2.31*) [106].

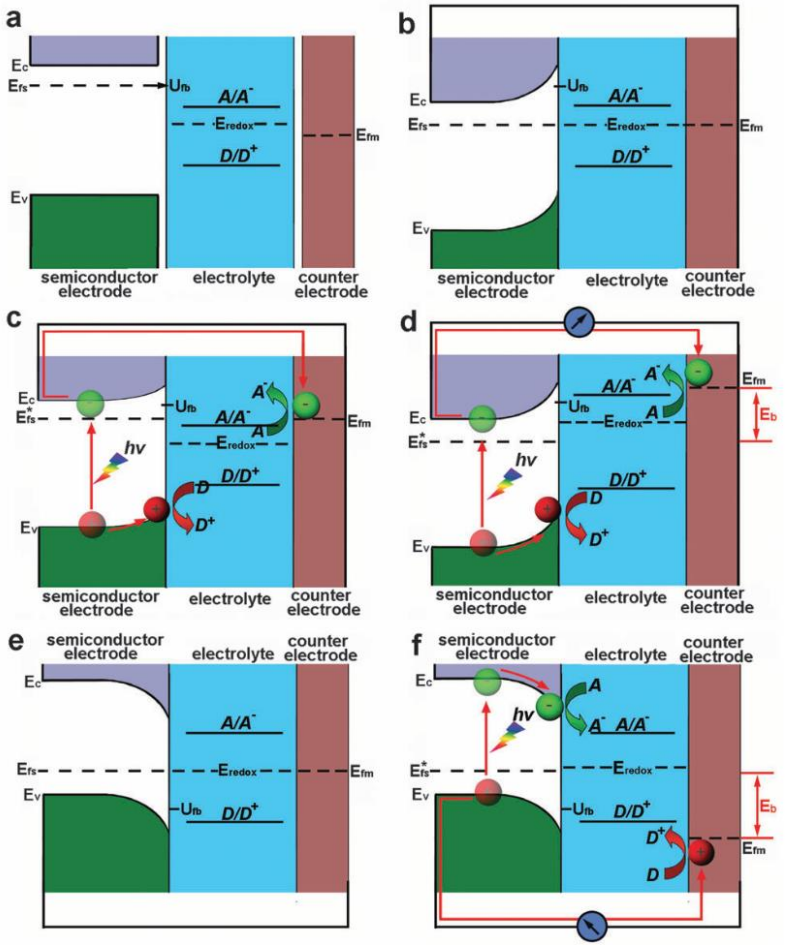

Figure 2.31. *Schematic band diagrams illustrating PEC processes: (a) before contact for an n-type semiconductor; (b) after contact for an n-type semiconductor*

in the dark; (c) n-type semiconductor under light irradia- tion without external bias; (d) n-type semiconductor under light irradiation with external bias; (e) after contact for a p-type semiconductor in the dark; and (f) p-type semiconductor under light irradiation with external bias. "A" indicates the electron acceptor species while "D" indicates the electron donor species. Taken from [106].

A reference electrode with a well-known electrode potential is often used in PEC measurements. By measuring the potential of the semiconductor with respect to that of the reference electrode, one can assess the reduction or oxidation power of the semiconductor electrode. As the two electrodes are in contact with the electrolyte, the E_f of the semiconductor and the metal should be kept in an equilibrium state with the E_f of the electrolyte (also the E_{redox}) (*Figure 2.31b*). Due to the presence of two redox couples in the electrolyte, the E_{redox} or E_f of the electrolyte is somewhere between the potentials of the redox couples, depending on the relative concentrations of reduction and oxidation products in the electrolyte. For the semiconductor (basically for *n*-type) with E_f higher than E_{redox}, the charge redistribution would lead to the bend-up of the semiconductor surface, forming a space charge layer on the semiconductor side [110].

When the semiconductor is excited by light, the internal electric field formed in the space charge layer can facilitate the separation of the photogenerated electrons and holes. The separated electrons can flow to the counter electrode through conducting wires, whereas the holes migrate toward the electrolyte. As a result, an internal photovoltage is formed, and the E_f levels of the semiconductor and the metal rise up to form a quasi-Fermi level of the semiconductor (E_{f*}). The band bending would decrease until the E_{f*} becomes higher than the potential of the reduction half reaction. Then the electrons on the counter electrode and the holes on the semiconductor can participate in reduction and oxidation reactions, respectively (*Figure 2.31c*). This condition is designated for the semiconductor with a large band gap, whose flat-band potential (U_{fb}) lies above the reduction potential of the electrolyte. The U_{fb} is the potential that needs to be applied to the semiconductor to reduce the band bending to zero. In other words, this potential denotes the E_f of the semiconductor with respect to the E_{redox} of the electrolyte before the contact and is the maximum E_{f*} possible for the semiconductor.

For the semiconductor with U_{fb} below the electrolyte reduction potential, an external positive bias (E_b) must be applied to raise the E_f of the metal above the reduction potential for the overall redox reactions (*Figure 2.31d*) [111]. In the meantime, the E_{f*} of the semiconductor declines, increasing the band bending and enhancing electron/hole separation.

In the PEC system with a semiconductor band bending up, as described above, the semiconductor electrode is the photoanode for the oxidation reaction, whereas the counter electrode is the cathode for the reduction reaction [111]. For the semiconductor (basically for *p*-type) with E_f lower than E_{redox}, instead the band bends down after the contact (*Figure 2.31*e) [112]. The charge transport directions driven by the formed internal electric field are thus contrary to the case of $E_f > E_{redox}$ (i.e., *n*-type). As a direct outcome, the E_f evolution by photovoltage and the locations for reduction and oxidation reactions are also reversed. When U_{fb} is higher than the electrolyte oxidation potential, a negative E_b has to be applied to lower the E_f of the metal electrode to carry out the overall redox reactions (*Figure 2.31f*) [106].

Generally, the VB of the n-type semiconductor and the CB of the p-type semiconductor can satisfy the demands on oxidation and reduction potentials of the electrolyte, so only the maximum reduction potentials for *n*-type semiconductors and oxidation potentials for *p*-type semiconductors are considered here. It is worth noting that the applied E_b should be smaller than the potential difference between the reduction and oxidation reactions in the electrolyte, such as 1.23 eV for water splitting. Otherwise, the E_b itself can drive the reactions without a photocatalytic process.

Moreover, the overpotentials have also to take into account in practical PEC reactions. The overpotential is defined as the difference between the thermodynamically determined reduction or oxidation potential of a half reaction and the potential at which the reaction is experimentally observed. The overpotential in a PEC reaction is a similar parameter to the activation energy in direct photocatalysis [106,113].

2.6.2 Metal-Semiconductor junction

Integration with metal is a commonly used configuration to harness the charge kinetics of a semiconductor. The metal may play a variety of roles in the improvement of photocatalytic performance. In terms of interfacial charge or energy transfer, there are mainly two mechanisms involved in metal–semiconductor hybrid photocatalysts: the Schottky junction and the plasmonic effect.

Depending on the photocatalytic systems (e.g., types of metals and semiconductors, and wavelengths of incident light), the two mechanisms may work together or separately. Only when a metal is in direct contact with a semiconductor can the Schottky junction be formed. Conversely, the plasmonic effect can affect the charge kinetics of a semiconductor even when an insulating interlayer is added between metal and semiconductor.

The noble metals, including Au, Ag and Cu, have strong plasmonic properties with bands located in the visible or the NIR region [114]. In comparison, some other metals, such as Pt and Pd, possess very small excitation cross sections for surface plasmon, and their plasmonic bands are mainly located in the UV region at small particle sizes (although they can be shifted to the visible light region by increasing the particle sizes) [115]. In the photocatalytic research field, without being particularly pointed out, only Au, Ag and Cu are commonly identified as plasmonic metals, whereas the others are considered as nonplasmonic metals. In addition to the metal type, the plasmonic properties of metal nanoparticles depend on their sizes and shapes as well as the dielectric properties of the surrounding media. This influence includes not only the wavelengths at which the plasmonic effect takes place but also the cross sections and field intensities. For instance, to make the plasmonic effect predominant, the sizes of metals should be controlled from tens to hundreds of nanometers in most cases [116].

Lastly, the surface plasmon can be excited only when the wavelengths of incident light fit the plasmonic bands of metals. Thus the plasmonic effect can only be operated under certain conditions, whereas the Schottky

junction is naturally formed as long as the metal and semiconductor have appropriate work functions and are in contact with each other [106].

2.6.3 Semiconductor-semiconductor junction

Semiconductor–semiconductor junctions are another type of hybrid structures used for steering the charge kinetics. As mentioned above, various semiconductor materials have characteristic band structures, which enable them to absorb light in diversified spectral regions and offer different capabilities in charge separation and transfer. The combination of different semiconductor materials may have complementary properties and create new materials with optimal performances (see section 2.5). For instance, forming unique semiconductor–semiconductor junctions can extend the spectral range for light absorption and enhance electron–hole separation. Depending on the band structure alignments of semiconductors and light excitation conditions, the charge dynamic models vary case by case [106].

Looking into the working mechanisms, one can identify that four different models of semiconductor–semiconductor junctions have been utilized to enhance the charge kinetics, including semiconductor sensitization [117], Type II [118], phase junction [119], and Z-scheme [120,121].

As explained in section 2.5, when only one semiconductor component is excited in a semiconductor–semiconductor junction, photogenerated charges may transfer to the other unexcited semiconductor. In this case, a semiconductor sensitization process takes place. In comparison, both semiconductor components are excited in the other three models. In the Type II structure, the electrons that are photogenerated from the semiconductor with a higher CB edge migrate to the one with a lower CB edge. Moreover, the photogenerated holes are transported from the low VB to the high VB between the semiconductors. The same charge flow works for the semiconductors with a phase junction, with the only difference being that the junction is formed by two different phases of a single semiconductor compound.

The three mechanisms, semiconductor sensitization, Type II and phase junction, are all based on direct electrical contact between two semiconductors. Similar to the metal–semiconductor contact in a Schottky junction, the interfacing of two semiconductors with different band structures leads to the charge redistribution equilibrating E_f (*Figure 2.32*).

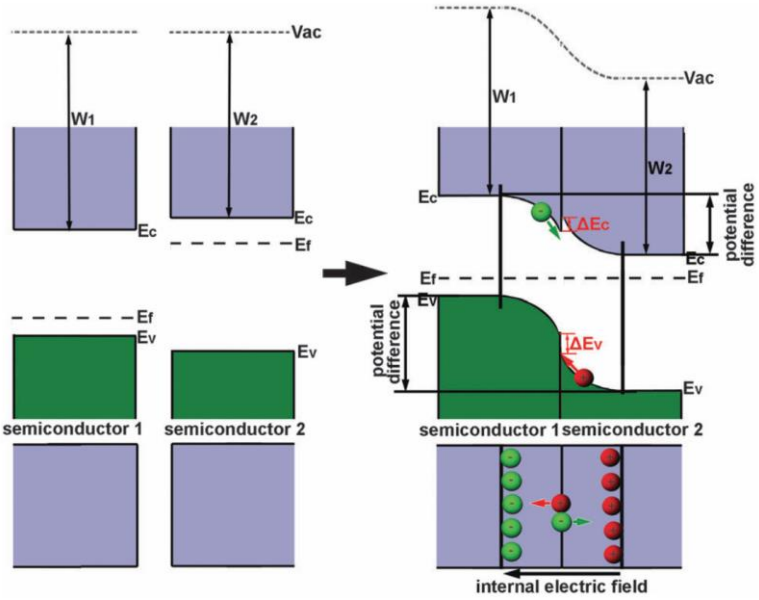

Figure 2.32. *Schematic band diagrams illustrating the formation of a semiconductor–semiconductor junction. Taken from* [106].

As a result, band bending has to occur in the space charge region, which creates an internal electric field and thus facilitates the separation of electrons and holes in the region. The directions of charge transfer depend on the relative edge positions of the CB and the VB of the two semiconductors. The electrons flow to the more positive position, whereas the holes diffuse to the more negative position. It should be noted that band discontinuity of the CB (ΔE_c) and the VB (ΔE_v) might be present after the E_f equilibration due to the difference in the flat-band CB and VB potential of the two semiconductors (*Figure 2.32*). However, to simplify the

discussion, this band discontinuity will not be particularly taken into account in the following sections [106].

2.6.3.1 Z-scheme

The model illustrated in this section is the Z-scheme structure. In this model, a conductor or a large number of defects exists at the contact interface of the two semiconductors, which may form ohmic contact with low contact resistance [121]. The photogenerated electrons from the semiconductor with a lower CB edge can directly recombine with the photogenerated holes from the other semiconductor with a higher VB edge through the ohmic contact [106].

In the entire semiconductor–semiconductor junctions described above, photogenerated electrons and/or holes migrate from one component to the other and lose energy during the process due to the band alignment. In this sense, their capabilities for redox reactions would be weakened. In other words, those junctions are designed to enhance the charge separation efficiency at the expense of charge redox ability. To circumvent this situation, a Z-scheme system has been considered by Song et al. [106], by mimicking the natural photosynthesis system, in recent years.

The Z-scheme structure is typically composed of two semiconductors with staggered alignment of band structures. The CB and VB of the two semiconductors do not satisfy the redox potential requirements for an overall reaction alone, but they can separately perform reduction or oxidation half reactions. In the Z-scheme, the photogenerated electrons from semiconductor 1 with a lower CB edge would recombine with the holes from semiconductor 2 with a higher VB edge. Moreover, the photogenerated electrons left in the CB of semiconductor 2 and the holes remaining in the VB of semiconductor 1 can be used for reduction and oxidation half reactions, respectively, constituting an overall redox reaction (*Figure 2.33a*) [121,122].

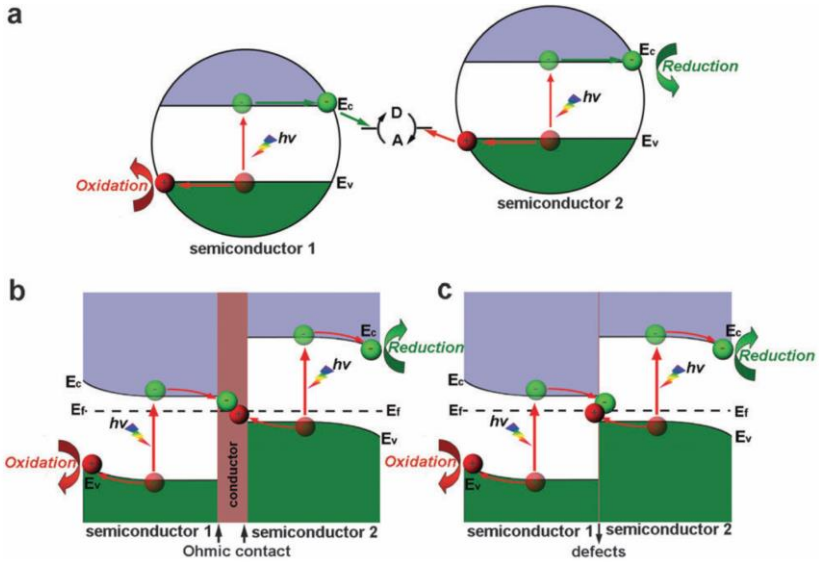

Figure 2.33. *Schematic band diagrams illustrating a Z-scheme structure: (a) indirect Z-scheme structure mediated by redox pairs; (b) semiconductor–conductor–semiconductor all-solid-state Z-scheme structure; and (c) semiconductor–semiconductor all-solid-state Z-scheme structure. Taken from [106].*

Apparently, the spatial separation of electrons from holes in this scheme will greatly contribute to charge recombination reduction. More importantly, the Z-scheme possesses an advantage that can be hardly attained by other designs: the remaining electrons and holes well maintain their energy levels so that the reaction activities will not be compro- mised. Furthermore, the semiconductors used in this design often have narrow band gaps for visible-light absorption. Thus the Z-scheme structure can harvest visible light to achieve an overall reaction, whose performance resembles that of a wide-bandgap semiconductor under UV illumination. In a Z-scheme system, the balance of catalytic rates for the two semiconductors is very important to the overall performance, as the overall reaction rates should be determined by the slower one. Moreover, its maximum efficiency for solar-energy conversion is half of that of a single-photon system, because a two-photon process is required to initiate the overall Z-scheme reactions [123].

In the early stage of the development of the Z-scheme, two separate semiconductors with electron acceptor–donor pair as mediators in solution constitute a typical indirect Z-scheme structure (*Figure 2.33a*) [122]. Upon the light excitation of the two semiconductors, the acceptor mediator is reduced to the donor mediator by accepting a photogenerated electron from the CB of semiconductor 1, whereas the produced donor mediator is oxidized back to the acceptor mediator by the holes from the VB of semiconductor 2 [106].

Then the photogenerated electrons in the CB of semiconductor 2 and the holes in the VB of semiconductor 1 participate in the photocatalytic reduction and oxidation reactions, respectively. However, in this indirect Z-scheme, backward reactions may also occur when the eletron acceptors and donor react with the designated electrons and holes, respectively. This feature would reduce the amount of electrons and holes preserved for photocatalytic redox reactions, and reduce the photocatalytic activity [106].

To solve this problem, an aceptor–donor pair free all-solid-state Z-scheme structure has been developed by employing a conductor as the electron mediator (*Figure 2.33*b) [120,121]. The conductor is inserted between the two semiconductors and forms ohmic contact with the semiconductors with low contact resistance. As a result, the electrons from the CB of semiconductor 1 can directly recombine with the holes from the VB of semiconductor 2 when they come across the conductor. The reported conductors include metals (Au, Ag, and Cd) [120,124,125], Visible Light Photocatalysts: Surface Plasmon Resonance and Z- Scheme Bridge) metal oxides (ITO) [126], and nonmetal materials (reduced graphene oxide, rGO [127].

Certainly, the electron mediator of conducting materials is not indispensable in the Z-scheme design. It has been reported that the direct contact between two semiconductor components may also formulate the all-solid-state Z-scheme model (*Figure 2.33c*) [128,129]. The key fact is the large number of defects existing at the solid–solid interface. It is known that interfacial defects are often the centers for charge recombination and

thus can play a similar role to the metal–semiconductor ohmic contact [106].

It should be noted that in the all-solid-state Z-scheme structure, the band bending (i.e., bending upward for semiconductor 1 and downward for semiconductor 2, from interface to surface) or other driving forces (e.g., co-catalysts) are often needed to facilitate the arrival of electrons (in semiconductor 2) and holes (in semiconductor 1) at the surface for redox reactions; otherwise, they may undergo recombination through the ohmic contact [120,125].

In general, as compared with the indirect Z-scheme, the all-solid-state Z-scheme structure greatly reduces the path length of charge transfer as well as the shielding effect caused by the aceptor–donor pair, offering better harnessed charge kinetics [106].

Chapter 3 Materials and Methods

This chapter presents the materials and methods used for the synthesis and characterization of either single phase or mixed oxide electrodes, prepared by different electrochemical techniques.

3.1 Synthesis of the nanostructured electrodes

This section summarizes the materials and methods employed for the preparation of either single TiO_2 or combined TiO_2-WO_3 electrodes. In the specific, the structure of the single-phases (TiO_2 or WO_3) as well as the distribution and reciprocal disposition of the semiconductors in the combined structure respect to the electric contact (Ti substrate) have been varied.

To form the proposed electrodes (Ti/TiO_2, *TiO_2 nanostructures*; Ti/TiO_2/WO_3, *WO_3 electrodeposited onto TiO_2 nanostructures*; Ti/TiO_2WO_3, *TiO_2-WO_3 nanotubes*; and Ti/TiO_2WO_3/WO_3, *WO_3 electrodeposited onto TiO_2-WO_3 nanotubes*), different nanostructures were developed on a Ti foil. In some cases, a second over-layer of WO_3 was deposited on the obtained nanostructures (see *Table 0.1* in the Abstract).

3.1.1 TiO_2-WO_3 mixed oxide electrodes

The preparation of the TiO_2-WO_3 electrodes, presented in this section, involves two processes for the production of strongly adherent nanoporous structures on the Ti substrate.

The first one is the formation of TiO_2 or TiO_2WO_3 nanostructured layers by oxidation of Ti foils; a description of the techniques used to prepare different nanometric structures will be presented in this section. In particular, compact TiO_2 layers were prepared by either thermal or electrochemical oxidation of Ti foils while the formation and growth of nanotubular TiO_2 or TiO_2WO_3 layers was carried out by titanium anodization in acid electrolyte containing fluorides.

The second process is the electrochemical deposition of WO_3 on the prepared nanostructures. A pulse potential technique was used in order to obtain a tungsten oxide over-layer on the different titania supports. Details about the deposition process are also reported in this section.

3.1.1.1 Chemicals and Materials

Chemicals: Titanium foils (1 cm x 7.5 cm x 0.025 cm, 99.7% metal basis) were used as raw material for the synthesis of the different TiO_2 or TiO_2WO_3 layers. Isopropanol (C_3H_8O), acetone (C_3H_6O) and methanol (CH_4O) were employed for the Ti foils degreasing pre-treatment. Glycerol (G), ethylene glycol (EG) and ammonia fluoride (NH_4F) were used as organic solvents and pitting agent in the anodization electrolyte, respectively. Sodium tungstate di-hydrate powder ($Na_2WO_4{\cdot}2H_2O$), hydrogen peroxide (H_2O_2), and nitric acid (HNO_3) were used to prepare the solution for the electrochemical deposition of WO_3. $Na_2WO_4{\cdot}2H_2O$ was also used for the preparation of TiO_2WO_3 nanotubes. All the chemicals were purchased from Sigma-Aldrich and used as received. Aqueous solutions were prepared using deionized (DI) water.

Materials: An ultrasonic cleaner (Model 9HTF, ASTRON) was used for the degreasing treatment of the Ti foils while a direct current supply device (GW Instek GPC-30300) was used for the anodization process. *Figure 3.1* shows a scheme of the conventional two-electrodes system used for the Ti foil anodization process: the Ti foils and a Pt grid were used as anodes and cathode, respectively.

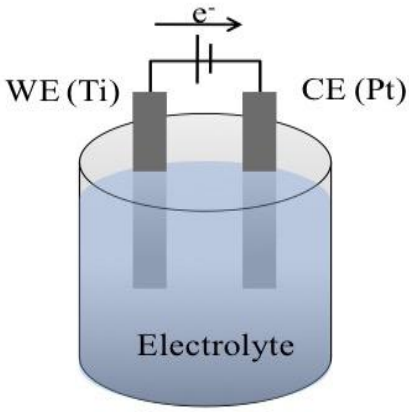

Figure 3.1. *Scheme of the two-electrode cell used for the anodization process.*

A Metrohm Autolab 302N potentiostat-galvanostat controlled by NOVA software (Metrohm, Switzerland) was employed for the electrochemical deposition of tungsten oxide, which was performed in a three-electrode cell; the TiO_2 or TiO_2WO_3 nanostructured materials were used as working electrodes, platinum constituted the counter electrode and a Saturated calomel electrode (SCE) was used as a reference.

3.1.1.2 Formation of TiO_2 and TiO_2WO_3 nanostructures: Ti/TiO_2 or Ti/TiO_2WO_3 electrodes

Prior to the oxidation processes, Ti foils were degreased by sonication in acetone, then in isopropanol and finally in methanol for a period of 10 minutes in each of the used solutions; then, they were rinsed with deionized water and dried in a Nitrogen stream.

Compact oxide layers - The compact TiO_2 was obtained by thermal oxidation of Ti foils at 500°C for 2h in air atmosphere or by electrochemical oxidation of Ti foils in glycerol organic solutions (in absence of fluoride ions). The electrochemical process was performed in a three-electrode cell. A potential ramp was imposed from the open circuit potential (OCP) to a fixed potential of 20 V with a scan rate of 100 mVs^{-1}. This potential value was kept constant for 3 hours.

Nanotubular layers - The TiO_2 and TiO_2WO_3 nanotubes were obtained by electrochemical oxidation of Ti foils, at room temperature, in the two-electrode cell reported in section 3.1.1.1. In particular, the oxidation process was performed in different organic solutions (see *Table 3.1*) containing a certain amount of ammonium fluoride ions, which was used as pitting agent for the formation of the nanotubular structures; either glycerol (G) or ethylene glycol (EG) were used as organic solvents.

To obtain the TiO_2WO_3 nanotubes, a certain amount of sodium tungstate was added to the oxidation bath. For all the cases, a potential ramp was imposed from the open circuit potential (OCP) to a fixed potential of 20 V with a scan rate of 100 mVs^{-1}. Then, depending on the samples, this potential value was kept constant for different times in order to obtain different dimensions of the nanotubes. *Table 3.1* summarizes the acronyms

of all prepared Ti/TiO_2 and Ti/TiO_2WO_3 electrodes along with their relative oxidation conditions.

Table 3.1. *Acronyms for the T/TiO_2 or Ti/TiO_2WO_3 electrodes along with the method employed for their synthesis and their relative oxidation conditions.*

Ti/TiO_2 Electrodes			
Acronym	**Method**	**Electrolyte**	**Time**
CTO	Thermal Treament	-	2 h
OC	Anodization	75% G / 25%H_20	3 h
NT	Anodization	75% G / 25%H_20 / 0.14M NH_4F	3 h
NT-05	Anodization	90% G / 10%H_20 / 0.14M NH_4F	0.5 h
NT-4	Anodization	90% G / 10%H_20 / 0.14M NH_4F	4 h
Ti/TiO_2WO_3 electrodes			
Acronym	**Method**	**Electrolyte**	**Time**
TW-6	Anodization	90% G / 10%H_20 / 0.14M NH_4F / 0.6mM $Na_2WO_4 \cdot 2H_2O$	4 h
TW-12	Anodization	90% G / 10%H_20 / 0.14M NH_4F / 12mM $Na_2WO_4 \cdot 2H_2O$	4 h
TW-25	Anodization	90% G / 10%H_20 / 0.14M NH_4F / 25mM $Na_2WO_4 \cdot 2H_2O$	4 h

*Details for the preparation of the electrodes used for the DOE technique are reported in section 4.2.

Except for method used to obtain the CTO electrode, the Ti oxidation processes were performed at room temperature and the resulting oxides were submitted to a final annealing treatment to transform the amorphous structure into a crystalline one. Thermal treatment was performed in air atmosphere at 400 °C for 1 h.

3.1.1.3 Electrochemical deposition of WO_3

Different procedures are reported in the literature to obtain tungsten oxide deposits. However, in this Thesis the electrochemical technique was adopted to obtain the WO_3 deposits. As reported in section 2.4.2.1, this method is widely used because the nanostructured WO_3 films can be tailored to exhibit desirable physical and chemical properties by varying the electrochemical synthesis parameters.

In this Thesis, the electrodeposition of tungsten oxide was performed at room temperature in a classical three-electrode cell in which a platinum grid was the counter electrode (anode). For specific purposes, some of the previously prepared electrodes (CTO, NT-4, NT-05, TW-12) were used as cathodes, while saturated calomel electrode (SCE) was the reference: all the potential values in this Thesis are referred to it. The distance between the cathode and anode was 0.5 cm. The electrodes were connected to a potentiostat-galvanostat (Metrohm Autolab 302N) controlled by NOVA software.

As reported in section **¡Error! No se encuentra el origen de la referencia.**, WO_3 films can be obtained by cathodic reduction of a tungsten peroxo precursor, equation 3.1, which was obtained by mixing a tungsten precursor with an excess of hydrogen peroxide. This procedure was adopted, in the present work, to obtain all the WO_3 deposits. In the specific, the deposition solution was prepared by dissolving sodium tungstate di-hydrate powder ($Na_2WO_4 \cdot 2H_2O$, 25 mM) in deionized water and by adding hydrogen peroxide (H_2O_2, 30 mM). The pH of the solution was adjusted to 1.5 by adding concentrated HNO_3.

The precursor was described as a dimer with the formula $W_2O_{11}^{2-}$ with a peroxide ligand. The oxidation state of W was +6 and the deposition reaction was described as:

$$\boldsymbol{W_2O_{11}^{2-} + (2+x)H^+ + xe^- \rightarrow 2WO_3 + (2+x)/2H_2O + (8-x)/4O_2} \qquad \textbf{(3.1)}$$

A preliminary voltammetric study was performed which allowed individuating the main reductive wave at -0.3 V (Figure 3.2), which can be related to the cathodic reduction of the tungsten peroxo precursor; i.e., the

deposition potential of WO_3 on the nanostructured supports. This potential value was adopted in the deposition process of tungsten oxide by potentiostatic runs.

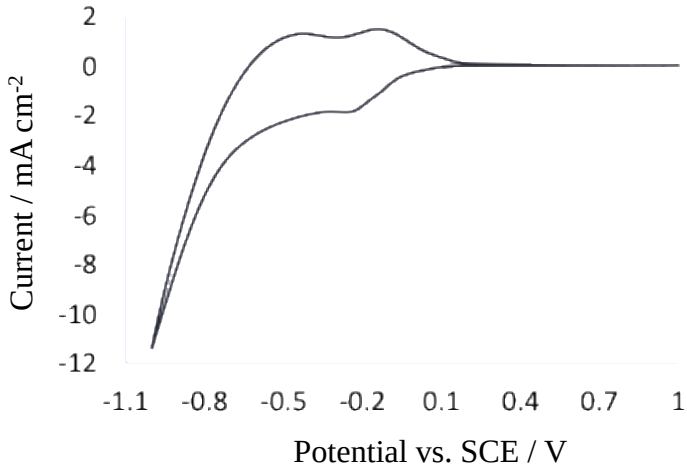

Figure 3.2. *Cyclic voltammogram of TiO_2 substrate in Na_2WO_4 (25 mM) and concentrated H_2O_2 (30 mM) solution.*

In order to establish an appropriate procedure and parameters for the electrochemical deposition of tungsten oxide on the TiO_2 nanotubular structures, a comparison between the photocurrents derived from preliminary experiments, in which the electro-deposition was performed both by step potential and pulse potential (PPT) techniques, was done in a previous work (data not reported in this Thesis, for more details see reference 147). Depending on the experimental technique, different morphologies of the deposit were obtained and in turn, different performances were measured in terms of photocurrent at the related samples. The obtained results indicated that the tungsten oxide deposition with the PPT seems to give better results, in terms of photoactivity.

Considering the results obtained in the previous work [147], a further research was also performed to evaluate the effect of different times of ON-OFF states (deposition-relaxing times) during the PPT: 1, 2, 5 and 10 were adopted as ON-time values, while 10, 7, 5 and 1 were selected as the relative OFF-time values for each adopted ON-time, respectively. The obtained data suggested that 1 s and 10 s were the optimum values for the times of

ON and OFF states, respectively. These values were adopted to obtain the tungsten oxide deposits in the Thesis.

Therefore, the PPT was used to obtain the tungsten oxide over-layer on the different substrates. During PPT, the potential was alternated swiftly between open circuit potential (OCP) and -0.3 V. A series of pulses of equal amplitude but different widths was performed. Each pulse consisted of an ON-time of 1 s during which -0.3 V was applied and an OFF-time of 10 s during which the electrode was maintained at the OCP value. During the PPT, the deposition solution was stirred (250 r.p.m) using a magnetic stirred to reduce or avoid concentration gradients by regenerating the W ion concentration at the cathode/solution interface.

Different WO_3 deposition times were adopted: from a 5 s up to 300 s. The number of pulses required to reach the proposed deposition times was calculated according to the ON-time duration. At the end of each experiment, the total amount of charge passed during the ON-Time intervals in the PPT runs was recorded.

Finally, the obtained Ti/*B*/WO_3 electrodes (where *B* indicates the TiO_2 or TiO_2WO_3 structures) were annealed in air atmosphere at 450 °C for 2 h. The adopted annealing temperature seems to not generate any changes on both the morphology or the TiO_2 phase of the prepared substrates (see section 4.4): under atmospheric pressure, anatase to rutile transformation in syntetic TiO_2 is usually observed at temperatures between 600 ˚C and 700 ˚C [170].

3.2 Characterization of the electrodes

3.2.1 Morphological characterization: SEM analysis

Morphological characterization of the samples and elemental mapping analysis were performed by means of scanning electron microscopy (SEM) equipped with EDX detector, (Zeiss Supra 40 FEG-SEM). Focused ion beam (FIB) was also used to obtain precise cross sections of the nanotubular samples for subsequent imaging via SEM.

3.2.2 Raman Measurements

Raman measurements were performed in order to reveal the crystalline phase of the different layers. These measurements were performed in air at room temperature using a BWTEK i-Raman Ex integrated system compact spectrometer, with an excitation wavelength at 1064 nm (provided by a Nd:YAG laser), in backscattering geometry. The spectra were collected with a very low power beam (< 5 mW) focalized in 1 mm^2 through a microscope objective Olympus x20 to avoid any heating effect.

3.2.3 Diffusive reflectance UV-vis spectra

Measurement of diffuse reflectance with UV-visible spectrophotometer is a standard technique in the determination of the absorption properties of materials. In the case of semiconductors for water splitting, one of the properties that can be estimated from the diffuse reflectance is the band-gap energy.

The diffuse reflectance UV-vis spectra of the synthesized electrodes were recorded by a spectrophotometer (Agilent Cary 100). The reflectance spectra were analyzed by using the Kubelka–Munk relation that transforms the measured reflectance, R, into a Kubelka-Munk function K that may be associated with the absorption coefficient:

$$\boldsymbol{K = F(R) = \frac{(1-R)^2}{2R}} \qquad \textbf{(3.2)}$$

The variation of the Kubelka-Munk function with photon energy, $(K\ h\nu)^{1/2}$ *vs* $h\nu$, was used to estimate the energy-gap of the samples.

3.3 Electrochemical and Photoelectrochemical characterization

This section reports the details of the electro- and photoelectro-chemical techniques used to evaluate the performance of the synthesized electrodes for the water splitting process. *Figure 3.3* shows a schematic representation of the experimental set up used for the electro- and photo-electrochemical tests.

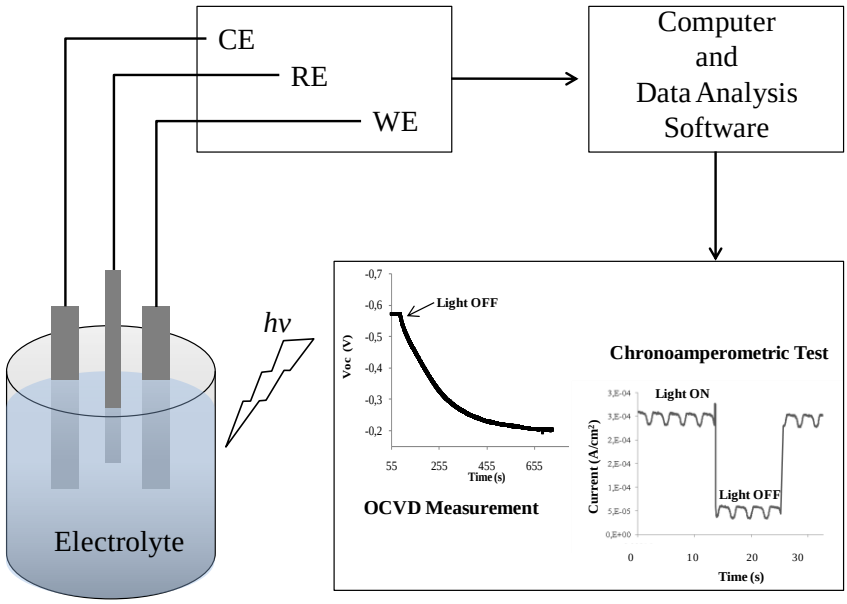

***Figure 3.3**. Set-up used for the characterization of the samples.*

The electrochemical and photoelectrochemical characterization of the synthesized photoanodes was carried out, in an undivided three-electrode cell equipped with a quartz window, at room temperature; the synthesized samples were used as working electrodes, Pt grid (metal coated on both

sides, 1,5 mm of thickness) as counter electrode and a Saturated Calomel Electrode (SCE) as reference. The electrical contact on the photoanodes was taken at the top section of the samples (section not immersed in the electrolyte), in which the oxide layer was previously scribed out. The distance between the WE and the CE was 1 cm. Different aqueous solutions were used as supporting electrolytes (0.1 M KOH or 0.1 M KNO_3). Depending on the experiments, glycerol was added to the electrolyte, as hole scavenger, to investigate on the extent of the photogenerated charges recombination in the examined structures. A fixed volume of electrolyte (40 mL) was employed in all the electro- and photoelectro-chemical experiments.

The photoactivity of the samples was tested under a light flux provided by a 300W Xe lamp (Lot Oriel) equipped with an IR water-filter. Suitable optical filters were used in order to select different wavelengths of the incident light (320 nm, 365 nm, 380 nm, 400 nm or 430 nm). In all cases, the active side (consisting of TiO_2 or TiO_2WO_3) of the electrodes in contact with the electrolyte was irradiated.

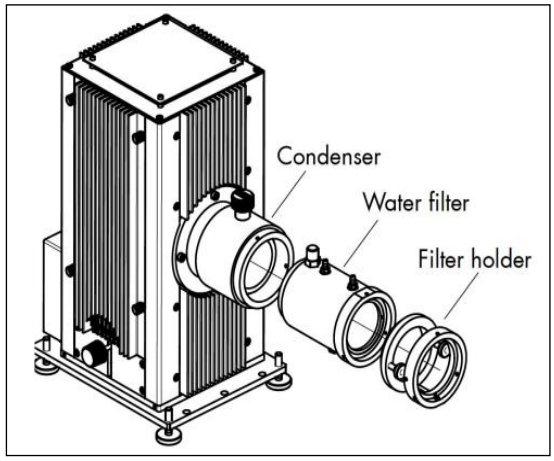

Figure 3.4. *Schematic representation of the 300W Xe lamp (Lot Oriel).*

3.3.1 Voltammetry Tests

The electron transfer kinetics and transport properties of electrolysis reactions can be derived from two related forms of voltammetry: cyclic or lineal sweep voltammetry.

Cyclic Volametry (CV) and Linear sweep voltammetry (LSV) tests were performed by measuring the current at the working electrode during a linear potential scan in absence or in the presence of irradiation. Depending on the experiment, different scan rates were used. The investigated potential range was adopted considering the specific aim of the electrochemical test: measurements were generally evaluated between -1.5 and 1.5 V.

The voltammogram represented by NOVA software shows the evolution of the current versus potential. With the analysis of this voltammogram it was possible to understand the electrochemical processes existing between the working electrode and the electrolyte.

3.3.2 Potentiodynamic Tests: Open Circuit Voltage Decay

A useful test for the calculation of the electron lifetime is the measurement of the Open Circuit Voltage Decay (OCVD) by using an optical excitation. This method requires the excitation of the band gap of the semiconductors with photons with equal or higher energy than their band gap.

The experiments were performed by irradiating the samples up to a stationary value of the OCV. At this point the illumination was turned off and the subsequent decay of open circuit voltage was monitored with time. A typical open circuit voltage decay measurement is represented in *Figure 3.5*

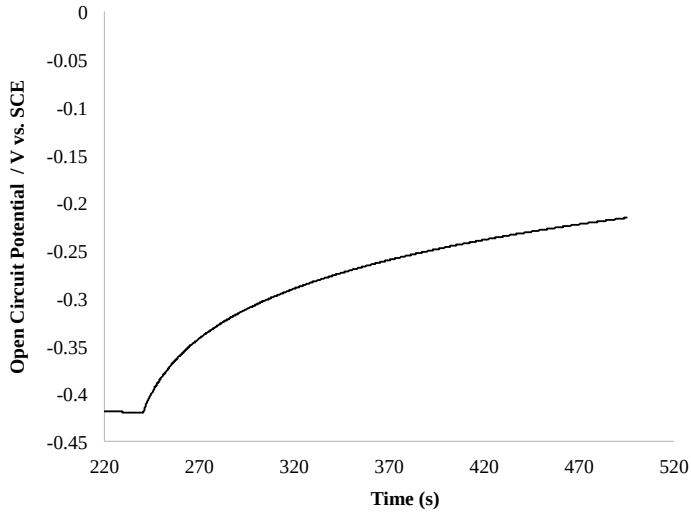

***Figure 3.5**. Open circuit voltage decay for a TiO_2 sample (λ=365nm).*

3.3.3 Chronoamperometric Test

Chronoamperometric tests were performed by applying different potentials to the PEC cell and by monitoring the corresponding current response. The tests were carried out either in a range of potential or at a bias potential enough to saturate the current (potential at which the current is independent of the applied potential).

The measurements were performed under chopped light irradiation: different optical filters were used in order to select different wavelengths of the incident light. *Figure 3.6* shows a typical chronoamperometric run performed at a fixed potential: under depletion conditions, negligible currents are generally generated under dark conditions while under illumination an increase of the current is observed.

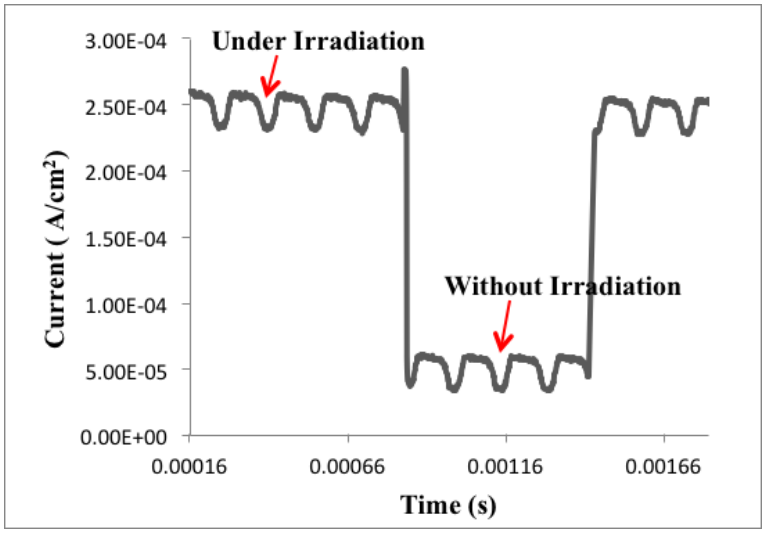

Figure 3.6. *Example of a typical photocurrent measurement.*

For all the cases, the photocurrent was calculated by subtracting the stable value measured in the dark from that obtained under irradiation. Photocurrent density values were calculated with respect to the nominal area. The incident power density (W/cm^2) of the light was measured by LP 471 UVU or LP 471 PAR quantum radiometric probes: its value was used as normalizing factor, when the comparison of the results obtained at the different wavelengths was needed (normalized photocurrent, NPC, calculated by equation 3.3). Depending on the filter, the average light power density striking on the surface of thee lectrode ranged from 1 to 11 mWcm^{-2}.

$$\boldsymbol{I_n(\lambda) = \frac{I_{light(\lambda)} - I_{dark}(\lambda)}{P(\lambda)}} \qquad \textbf{(3.3)}$$

where I_{light} *and* I_{dark} are the photocurrent density values (A m^{-2}) (calculated considering the nominal area of the electrode in contact with the electrolyte (and P is the incident power density (W m^{-2}).

The incident to current efficiency (IPCE), for a specific wavelength (λ) value, was calculated according to the following equation (see section 2.3.3).

$$IPCE(\%) = \frac{I(Am^{-2})1240}{P_{\lambda}(Wm^{-2})}\,100 \qquad (3.4)$$

3.3.4 Electrochemical Impedance Spectroscopy (EIS)

A frequency response analyser (FRA, Model 7200 Amel) with an excitation signal of 10 mV of amplitude was used to perform the EIS experiments. Measurements were performed in aqueous electrolytes (0.1 M KOH or 0.1 M KNO_3), under dark and different irradiation conditions. In some cases, EIS runs were also performed in 0.1M KNO_3 / 10% (v/v) glycerol solution. The investigated frequency range was from 10^5 Hz to 10^{-2} Hz.

By using the EIS method, two different tests were carried out:

In the first one, the impedance vs. frequency spectra was acquired under dark conditions at a potential range from -0.5 V to 0.5 V vs. the SCE electrode (using 10 potential increments of 0.1 V). The data measured in this test will be treated by the Mott-Schottky relationship to derive information about the electron carrier density (N_D) of specific electrodes (see section 4.1.5). The section 2.3.2.1 provides further detailed information about the Mott-Schottky method.

In brief, the imaginary component of the impedance Z" allowed to evaluate the space charge capacitance as C=1/2πfZ", and its trend with potential allows to derive information on the semiconductor behavior. In particular, the N_D values were determined following the equation 3.5 by using the EIS data obtained at a specific frequency and under depletion conditions (see background in section 2.3.2.1).

$$\frac{1}{C^2} = \frac{2}{N_D e \varepsilon \varepsilon_0}\left[\left(E_s - E_{fb}\right) - \frac{K_B T}{e}\right] \qquad (3.5)$$

In equation 3.5, C is the space charge capacitance in the semiconductor; N_D is the electron carrier density; e is the elemental charge value; ε_o is the

permittivity of a vacuum; ε is the relative permittivity of the semiconductor; E_s is the applied potential; E_{fb} is the flatband potential; T is the temperature; and K_B is the Boltzmann constant.

The second test consisted in the acquisition of the impedance vs. frequency spectra at the open circuit potential value, under different irradiation conditions (λ= 365 nm and 400 nm). The EIS data measured in this test will be adjusted to an equivalent electrical circuit: the circuital parameters will be used to give indications about the charge transfer mechanism in the nanostructured materials.

3.4 DOE technique

The design of experiments (DOE) is a powerful tool that can be used in a variety of experimental situations. DOE allows for several input factors (influent parameters) to be manipulated determining their effect on a desired output (objective functions). By manipulating the influential parameters at the same time, DOE can identify important interactions that may be missed when experimenting with one parameter at a time [130].

In this Thesis, it is desirable to understand the effect of the anodization bath composition on both the aspect ratio and the photoelectrochemical performance of the nanotubular structures. In particular, the effect of all possible combinations between the considered influential parameters (organic solvent, water content and fluoride concentration) on the proposed objective functions (aspect ratio and PEC performance) will be investigated by a full factorial design.

Chapter 4 Results and Discussion

This chapter reports the results derived from the morphological, electro- and photoelecro-chemical tests performed at the synthesized electrodes. The results will be compared in order to establish efficient nanostructured materials for solar cell applications.

4.1 TiO_2 Nanostructures: Ti/TiO_2 electrodes

The electro- and photoelectro-chemical properties of semiconductor materials depend highly on their morphology. This section is focused on the study of the morphology of single-phase TiO_2 nanostructurated materials in context of their application as photo anodes in PEC systems. Different TiO_2 morphologies (Nanotubular and Compact TiO_2 nanometric structures) were synthesized by anodization of Ti in specific electrolytic baths. Scanning Electron Microscopy was used to analyze the morphology of the assembled electrodes while several parameters of the samples were investigated, using chronoamperometric and potentiodynamic tests, to give indications of the charge transport in the semiconductor structure and the lifetime of the photo-generated electrons.

4.1.1 Preparation of the Ti/TiO_2 electrodes

All the samples were obtained from Ti foils (0.25mm thick, 99.7% metal basis, Aldrich). A preliminary treatment was performed in which Ti foils were degreased by sonication following the procedure explained in section 3.1.1.2.

To obtain the nanotubular TiO_2 electrodes (NT), after this preliminary treatment, the Ti foils were electrochemically oxidized in a two-electrode cell (see *Figure 4.1*) at 20V for three hours (1 cm^2 of Ti nominal area in contact with the electrolyte) in (25%) H_2O / (75%) glycerol organic solution with 0.14 M of NaH_4F. Then, the samples were rinsed with distilled water and ethanol and annealed 1 h at 400˚C in air in order to increase the crystalline structure of the materials. The compact TiO_2 electrodes (OC) were prepared with the same procedure described above, but without fluorides in the oxidation bath. *Figure 4.1* shows a schematic representation of the expected OC and NT structures.

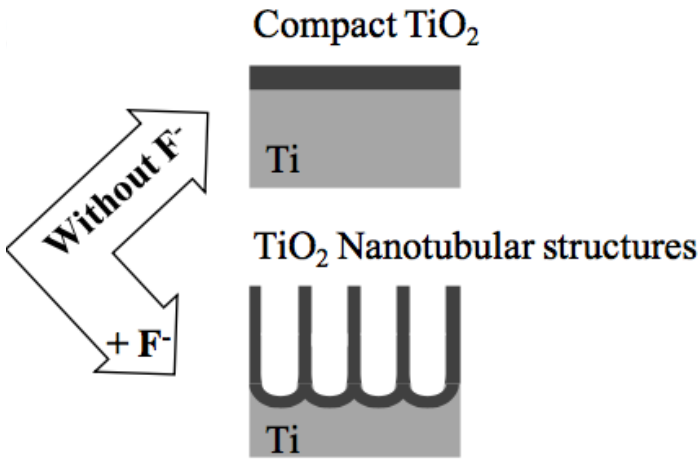

Figure 4.1. *Sechematic representation of the expected OC and NT nanostructures.*

4.1.2 Morphological Characterization of the Ti/TiO_2 electrodes

The morphology of the different nanostructures was investigated by means of Scanning Electron Microscopy (SEM). *Figure 4.2* reports the micrographs of the synthesized TiO_2 compact layer and the TiO_2 nanotubular structures.

The use of fluoride anions (F^-) in the anodization electrolyte allowed the formation of TiO_2 nanotubes while in the absence of F^- the compact layer is formed; in most neutral and acidic electrolytes, the anodization process leads to the formation of a compact TiO_2 layer on the Ti foil while in the presence of F^- in the electrolyte, highly ordered nanoporous or nanotubular oxide layers can be obtained [131].

The change of the compact layer into nanotubes can be explained as follows: initially, fluorides induced the dissolution of the formed TiO_2 and the formation of TiO_2 nanotubes. Then, the growth of the oxide, which takes place at the inner interface, and the chemical dissolution of the oxide layer occur simultaneously.

Finally, an steady state is established when the pore growth rate at the metal oxide interface is equal to the thickness reducing dissolution rate of the oxide film at the outer interface [131,132].

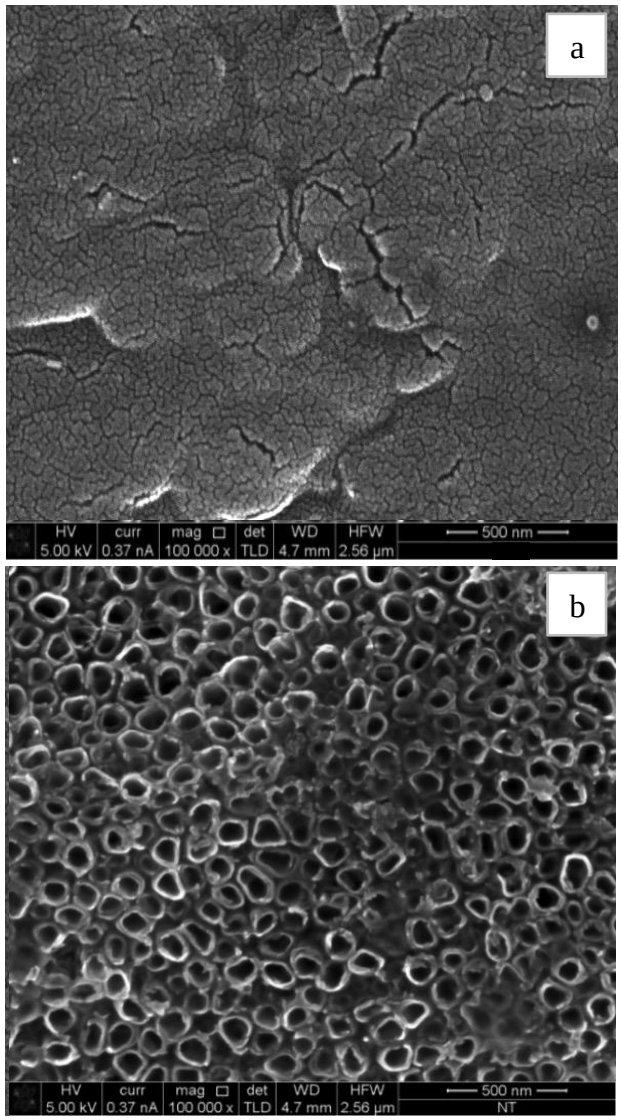

(SEM micrographs of Ti/TiO_2 electrodes, figure 4.2)

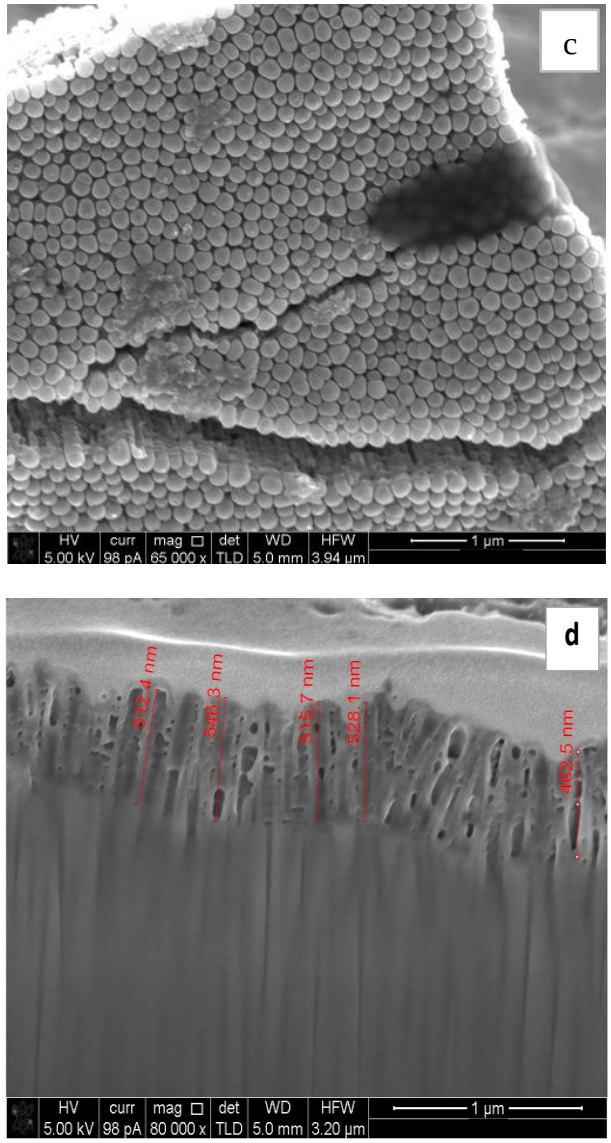

***Figure 4.2**. SEM micrographs of Ti/TiO_2 electrodes: OC sample (a); top (b), bottom view (c) and (d) SEM micrograph of FIB cross sections of the nanotubes at the NT sample.*

The morphology of the surface of the compact TiO_2 layer (see *Figure 4.2a*) is characterized by a granulated structure; this sample seems to be composed of nanoparticles interconnected in a porous network. However, as shown in *Figure 4.2b*, ordered nanotubular structures with an outer

diameter in the range of 70-90 nm are obtained at the NT sample [133]. The nanotubes were characterized by a mean length of about 500nm. It must be also considered that the dimensions of the nanotubes can be affected, among other influential parameters, by the composition of the anodization solution; this aspect, will be investigated more in detail in section 4.2.

The nanotubular ordered porous architecture of the NT sample is expected to provide a larger surface area in contact with the electrolyte, increasing the phocatalytic activity of the TiO_2 material as compared to that of the compact oxide layer. Moreover, the 1-D nanostructures may improve the electron transport properties due to unidirectional smooth electron mobility, thereby accelerating the electron flow to the external circuit. In order to verify these assumptions, photoelectro-chemical characterization of the samples was performed.

4.1.3 Chronoamperometric Test: electron transport

The PEC performance of the OC and NT nanostructures was evaluated using the samples as photoanodes for the water splitting reaction in 0.1M KOH solution (ph:10). *Figure 4.3* summarizes the photo-response obtained at different wavelengths for the two investigated samples, in terms of normalized photocurrent (NPC). It is worth noting that the NPC values were calculated considering the nominal area of the electrodes in contact with the electrolyte. Therefore, differences observed between the NPC values of the analyzed electrodes can be also influenced by this fact.

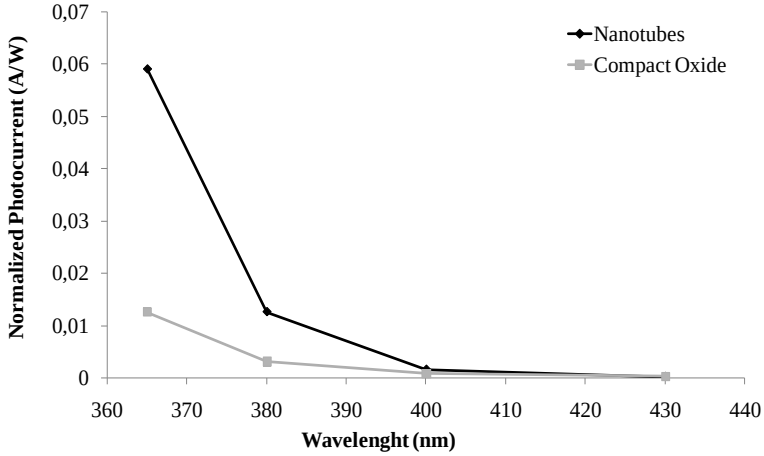

Figure 4.3. *Normalised Photocurrent for the OC and NT samples at different wavelength values.*

For both the samples, highest NPC values were obtained at the shorter wavelengths, due to their more energetic character. Moreover, when the TiO_2 material changes from compact to tubular structure, progressive enhancement of the photocurrent of the sample is observed: the NT sample showed consistently higher photocurrent values under the same condition than those presented by the OC (see black line in *Figure 4.3*). As an example, at 365nm, a five-fold increase of the incident photon to current efficiency (IPCE) of the TiO_2 material was achieved when the NT sample was employed as photoanode (IPCE of the OC: 4.35 % and IPCE of the NT: 22.65 %).

The observed behavior can be mainly due to the higher specific area of the NT sample but also to a faster flow of the photogenerated charges through the material: kinetic and dynamic studies, reported in literature, of dye sensitized solar cells composed of nanoparticulate TiO_2 films evidence that the limiting factors for a well performance of the system are the random path processes of the charges and trapping/detrapping of electrons through the porous network [134]. In the case of the OC sample, the random morphology of the crystalline TiO_2 nanoparticles may exhibits high defect density, which leads to the electron losses via recombination and in turns lower electron collection efficiency can be expected. However, the nanotubular structures are aligned in a regular array perpendicular to the

back contact (Ti) leading to a faster unidirectional electron transport with a reduction of the recombination, if compared with the OC structure (see scheme in *Figure 4.4*).

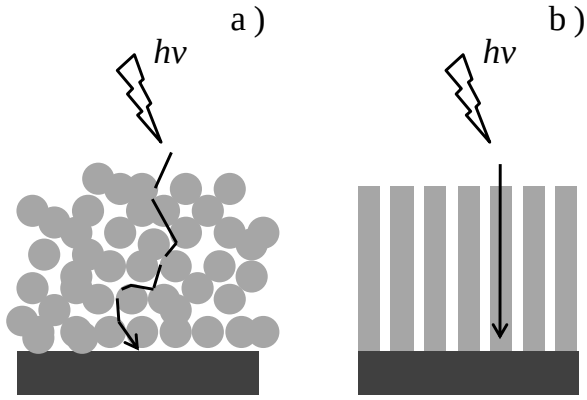

***Figure 4.4**. Schematic representation of electron flow in the OC (a) and (b) the NT photoelectrodes.*

4.1.4 Open circuit voltage decay (OCVD): electron lifetime

The OCVD measurement provides useful information about the electron-hole recombination process at the TiO_2 material. The excitation of the TiO_2 band gap, with photons with equal or higher energy than its band gap, results in charge separation (band gap of TiO_2 : 3.2 eV for anatase and 3.0 eV for rutile) [135,136]. In the absence of a hole scavenger, photo-generated holes react with hole acceptor species in the electrolyte at the TiO_2/electrolyte interface, while the accumulation of the photogenerated electrons occurs within the TiO_2 layer. The electron accumulation causes a shift of the Fermi level to more negative potentials, and an increase of the open circuit voltage (OCV) is observed. A maximum value of the OCV is reached when the equilibrium between the electron accumulation and the charge recombination is achieved. Upon stopping the illumination, the OCV decays as the photogenerated electrons accumulated within the TiO_2 can react with electron acceptor species in the electrolyte, or recombine with trapped holes. Therefore, information about the charge recombination

process at the investigated TiO_2 samples, and in turns about the electron lifetime (τ_n), can be provided by monitoring the OCV decay after stooping the UV illumination [137].

The interpretation of the OCVD data involves the extraction of the electron lifetime *via* equation 4.1, which is related to the time derivate of the OCV decay [138].

$$\boldsymbol{\tau_n = -\frac{K_B T}{e}\left(\frac{dV_{OC}}{dt}\right)^{-1}} \qquad \textbf{(4.1)}$$

where τ_n is the electron lifetime, K_B is the Boltzmann's constant, T is the temperature in K, e is the charge of a single electron, and V_{oc} is the open circuit voltage at time t.

A comparison of the electron lifetimes derived from the OCVD data is represented in *Figure 4.5*.

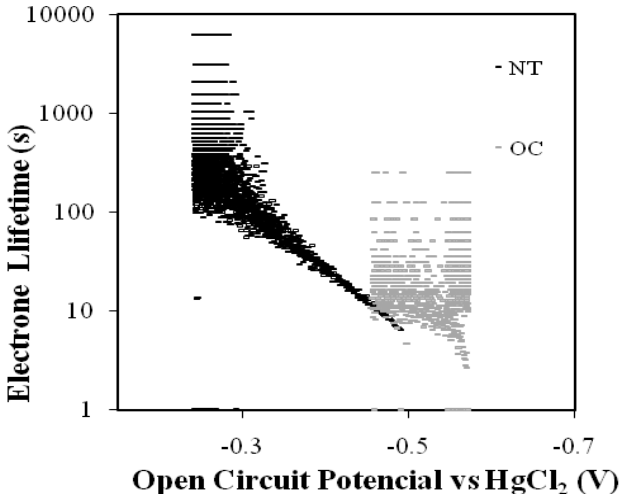

Figure 4.5. *Electron lifetimes as extracted from OCVD measurements for the OC and NT electrodes.*

The electron lifetimes for both the investigated samples exhibit similar trends but different values. As discussed in section 4.1.3, the use of well

ordered nanotubular structures reduces the recombination rate at the TiO_2 material, leading to longer electron lifetimes; the electron lifetime values for the OC electrode oscillate around the tens of seconds, thereby indicating a lower lifetime of the photogenerated electrons at this electrode, i.e. this sample may present faster charge recombination rate with respect to the NT electrode.

4.1.5 Mott-Schottky Analysis: electron carrier density

A preliminary study was done to select a frequency value to apply the Mott-Schotty (MS) method, which was used to derive information about the electron carrier density (N_D) at the OC and NT samples. As an example, *Figure 4.6* shows the trend of the capacitance as a function of the voltage and frequency for the NT sample.

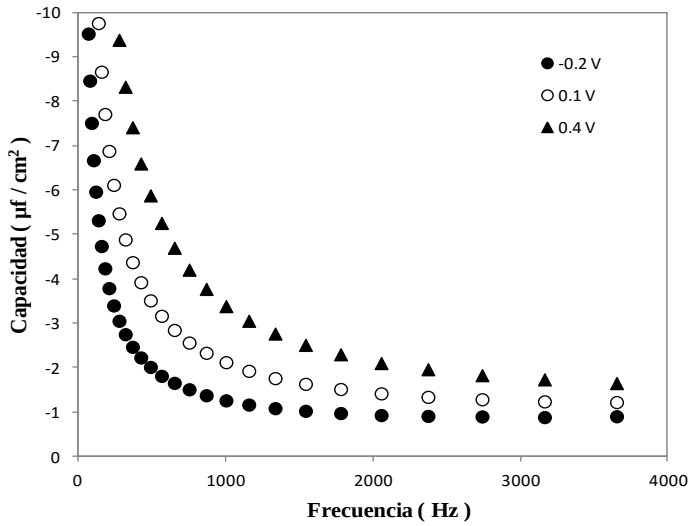

Figure 4.6. *Trend of the capacitance as a function of voltage and frequency for the NT sample.*

As it is possible to observe in *Figure 4.6*, the capacitance is independent of potential and frequency at frequency values higher tan 2.5 kHz: at lower

values the variation of the capacitance may generate significant experimental errors during the determination of the electron carrier density of the TiO_2 semiconductor material. On this basis, 3 kHz was adopted as frequency value to analyse the EIS measurements by the MS relationship.

For an ideal capacitive behavior of an n-type semiconductor, a positive slope of the linear trend of $1/C^2$ versus potential is expected, and donor concentration of the semiconductor can be derived from this trend. It should be noted that MS analysis is strictly applicable to regular compact oxides and under depletion conditions of the space charge layer. However, it is often applied also to irregular geometries with porous surfaces as well as to nanotubular layers [139]. *Figure 4.7* presents the linear parts of the curves of the MS plot as $1/C^2$ vs. potential; $1/C^2$ values were calculated as explained in section 3.3.4).

As shown in *Figure 4.7*, the positive slopes indicate the typical behaviour of n-type semiconductors [140].

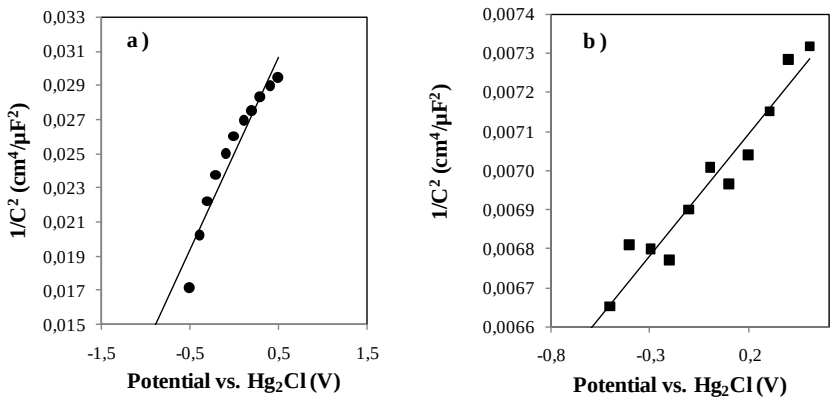

Figure 4.7. *Mott-Schottky plots at a fixed frequency of 3KHz on (a) OC and (b) NT electrodes. The linear fit to each curve is given by the following linear relation: (a) y = 0.0113x+0.025 (b) y = 0.006x+0.007.*

Considering that the term K_BT/e is negligible, the N_D, was determined from the slope (m) of the data depicted in *Figure 4.7* using the following equation:

$$N_D = \frac{2}{e\varepsilon\epsilon_o m} \quad \textbf{(4.2)}$$

Using e = 1.6 x 10^{-19} C, ε = 48 and ε_0 = 8.86 x 10^{-12} F m^{-1} for the TiO_2 anatase phase, the calculated electron carrier densities for the OC and NT electrodes were $2.98 \cdot 10^{20}$ and $1.53 \cdot 10^{21}$ respectively.

As reported in literatute [140], the higher N_D value observed for the NT sample may confirm a better charge transport in the TiO_2 material, if compared to the OC, and it can also shift the Fermi level of the semiconductor toward its conduction band, which further facilitates the charge separation at the semiconductor/electrolyte interface, improving the PEC performance.

4.1.6 Conclusions

The proposal anodization technique is an effective strategy for the preparation of TiO_2 nanostructured electrodes. The SEM results have demonstrated the formation of compact or nanotubar titania layers.

The photo electrochemical performances of TiO_2 based photoanodes were investigated in this section. The nanotubular structured surface of the titania electrode led to higher values of photocurrent, which are correlated to a higher superficial area of the resulting sample, but also to a better electron transfer.

The TiO_2 nanotubular structures offer large surface areas with a smooth electron transport along the length of the nanotubes, thereby, minimizing the charge losses occurred due to the trapping of electrons through the boundaries of the nanoparticles of the OC sample: electron transfer through the nanotubes is superior to electron percolation through the random particulate layer. The enhancement in electron charge transport in the NT sample is assessed by the results derived from the chronoamperometric tests, OCVD measurements and MS analysis: if compared with the compact oxide, higher IPCE, τ_n and N_D values were observed for the NT sample.

4.2 Effect of the synthesis conditions on the morphology and photoactivity of TiO_2 electrodes

This section presents the results of an experimental study on the effects of the anodization bath composition used in the synthesis of the TiO_2 nanotubular structures. The experiments were carried out in a systematic way trough the design of experiment (DOE) technique [130]. In particular, the organic solvent, the fluoride concentration and the water content in the anodization bath were selected as influent parameters, and their effect on both the structure and photoelectrocatalytic performance of TiO_2 nanotubes in the PEC water splitting reaction was study. For this purpose the DOE technique has been adopted with the aim of identifying the minimum number of experiments required to evaluate both single and combined effects of the investigated parameters on the aspect ratio of the tubes (defined by the ratio between length and diameter) and the photocurrent, which were assumed as objective functions.

4.2.1 Preparation of the TiO_2 Nanotubes: Ti/TiO_2 electrodes

Each sample obtained from Ti foils was previously polished using the procedure previously indicated in section 3.1.1.2. Then, the samples were submitted to an oxidative process in which the formation and growth of different TiO_2 NT structures were performed. The anodization process was carried out in water/organic solution, which always contained a certain amount of fluoride ions as pitting agent. The anodization was carried out using the conventional two-electrode system in which the Ti foil was used as anode and a Pt grid as cathode at room temperature (see section 4.1.1). A potential ramp was applied from open circuit voltage (OCV) to a fixed potential (20 V) with a scan rate of 100 mVs^{-1}; then, the applied potential was maintained at this fixed value for 3 h. A final annealing treatment (400°C, 1 h) was required in order to transform the amorphous structure into crystalline one.

4.2.2 DOE technique: Set of experiments

The DOE technique was used to plan the set of the experiments in which the organic solvent (S), water content (W) and fluoride concentration (F) were considered as influent parameters, and they were varied on two levels in a full factorial design. *Table 4.1* shows the values of the coded parameters at the minimum (-1) and maximum (+1) levels.

Table 4.1. *Coded parameters for the DOE analysis.*

Parameter		**Fluoride Concentration**	**Water content**	**Solvent**
Unit		Mol/L	vol%	-
Symbol		**F**	**W**	**S**
Level	-1	0.05	0.5	EG
			20	G
	1	0.14	3	EG
			30	G

In particular, as far as the solvent was concerned, it being a non-quantitative parameter, the low and high levels were arbitrarily chosen: low level (-1) was assigned to ethylene glycol (EG), and high level (+1) to glycerol (G). Two different ranges of water content were considered, depending on the kind of organic solvent used in the anodization solution. A range of water content around 30-40 vol% has been considered in the case of G solvent, but low levels have been used in the case of EG. According to the literature [141], the presence of high water contents in EG based electrolytes may destroy the NT structure, generating cotton-like structures on the substrate. Considering this fact, for the EG, 0.5 vol% and 3 vol% of water content were used as low and high values. Two fluoride concentrations of 0.05 M and 0.14 M were considered, representing the lowest and highest levels for this factor.

For a full factorial design, in which n parameters are considered at L levels, the minimum number of samples N which are needed to correctly apply the DOE technique is derived as $N=L^n$. In the specific case in which 3 factors were varied at 2 levels, 8 samples were synthesized under different experimental conditions. The performance of each sample was evaluated by measuring the values of aspect ratio γ, defined by the ratio between length and diameter ($\gamma = l/\varphi$) of the tubes, and the photocurrents measured

at wavelengths of 365 nm (i_{365}) and 400 nm (i_{400}) which were adopted as objective function in the analysis.

Table 4.2 represents the DOE matrix which illustrates the whole plan of the experiments: the composition of the bath solution for the synthesis of the 8 samples was derived by the first three columns, in which the coded parameters were combined to indicate the specific conditions of each experiment. Y_{ij} reported in the DOE matrix indicate the response obtained at the *j*-th sample for the *i*-th objective function.

Table 4.2. *DOE matrix for the calculation of the experimental conditions.*

Sample	Parameters			Codes for combined effects				Objective function
	F	W	S	FW	FS	WS	FWS	Y_i
1	1	1	1	1	1	1	1	y_{i1}
2	-1	1	1	-1	-1	1	-1	y_{i2}
3	1	-1	1	-1	1	-1	-1	y_{i3}
4	-1	-1	1	1	-1	-1	1	y_{i4}
5	1	1	-1	1	-1	-1	-1	y_{i5}
6	-1	1	-1	-1	1	-1	1	y_{i6}
7	1	-1	-1	-1	-1	1	1	y_{i7}
8	-1	-1	-1	1	1	1	-1	y_{i8}

As indicated by the technique, the influence of the *p*-th parameter (effect E_p) on the objective function Y may be evaluated by the following equation:

$$\boldsymbol{E_p = \bar{y}^{(+)} - \bar{y}^{(-)} = \frac{\sum_p y_p^{(+)} - \sum_p y_p^{(-)}}{4}} \qquad \textbf{(4.3)}$$

where $\bar{y}^{(+)}$ and $\bar{y}^{(-)}$ represent the mean of the values of the responses obtained from runs in which the *p*-th parameter was set at the highest (+1) and lowest (-1) levels, respectively.

In order to evaluate the combined effects between two parameters *p* and *q*, Eq. 4.3 can be still used if the related columns (*pq*) in *Table 4.2* are considered to identify the maximum and the minimum levels of the

combination of parameters. The related responses obtained in the planned experiments are schematically represented in *Figure 4.8*. A typical cube representation is adopted where the dimension of dots in the corners indicates the relative magnitude of the related objective function values.

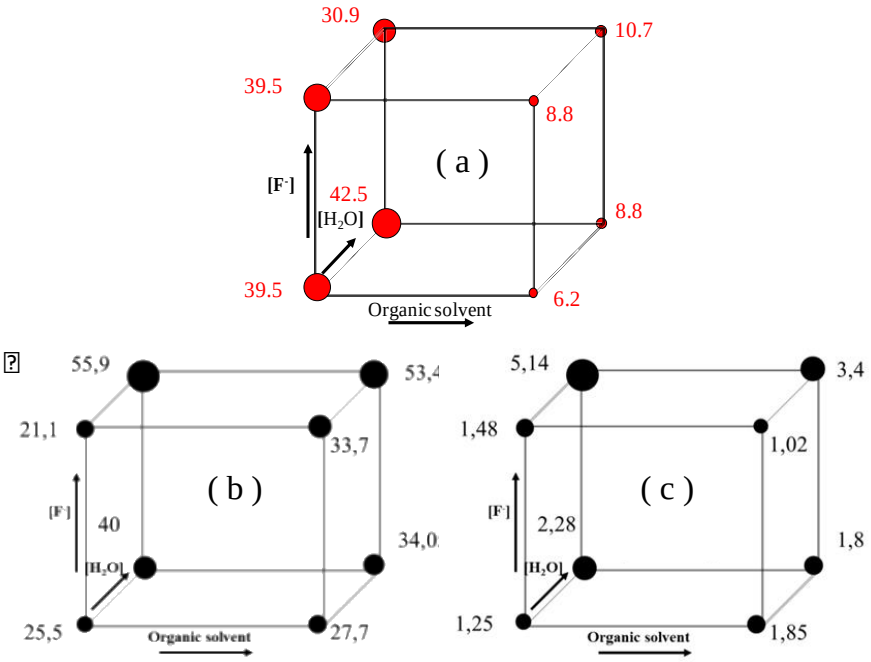

Figure 4.8. *Cube representation of the objective functions values for all the synthesized sample: nanotube aspect ratio (a), normalized photocurrent at 365 nm (b) and (c) at 400 nm (values in mA/W).*

4.2.3 Effect of the anodization bath composition on the aspect ratio

Figure 4.9 depicts the effects calculated by equation 4.3. As can be observed, W content and F concentration in the anodization bath appear not to influence the morphology, while the most influential parameter on the nanotubes aspect ratio is the solvent [142].

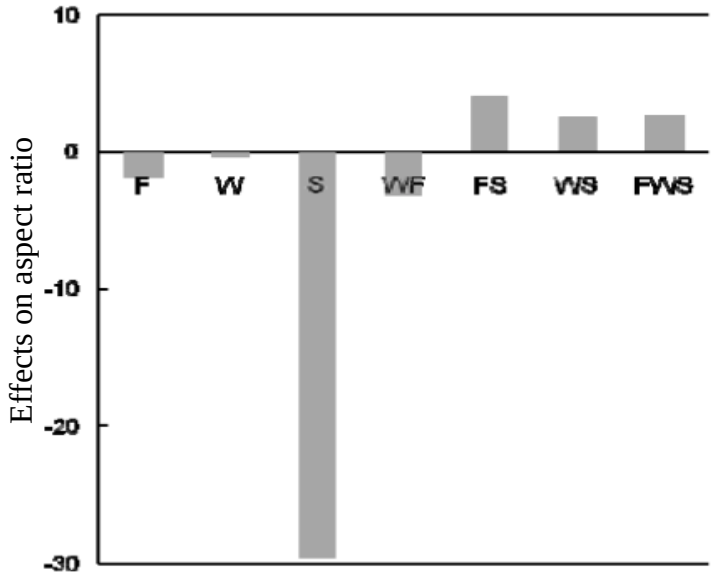

Figure 4.9. *Effects of the parameters and their interactions on the aspect ratio (F: fluoride concentration; W: water content; S: solvent).*

Accordingly, SEM analysis (*Figure 4.10*) showed longer tubes with narrow diameters for samples anodized in EG rather than in G. For this objective function (aspect ratio), the combined effects may be considered non-significant.

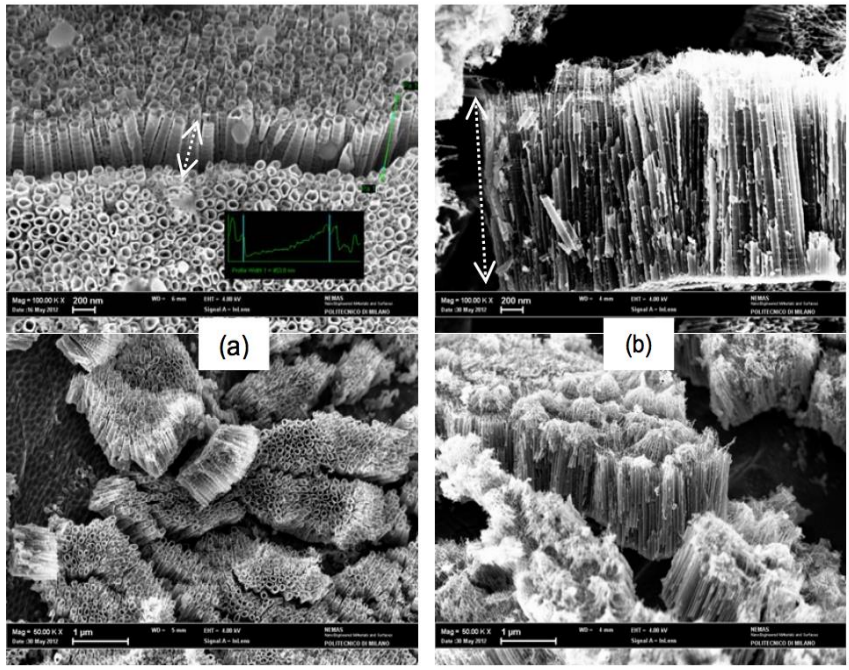

Figure 4.10. *SEM images of the samples synthesized in G (a) and (b) in EG.*

4.2.4 Effect of the anodization bath composition on the photocurrent

Concerning the photocurrents, for both the cases the triple effects are negligible and the most relevant single effect is that of water. Moreover, combined binary effects seem to be effective for these objective functions (i_{365} and i_{400}).

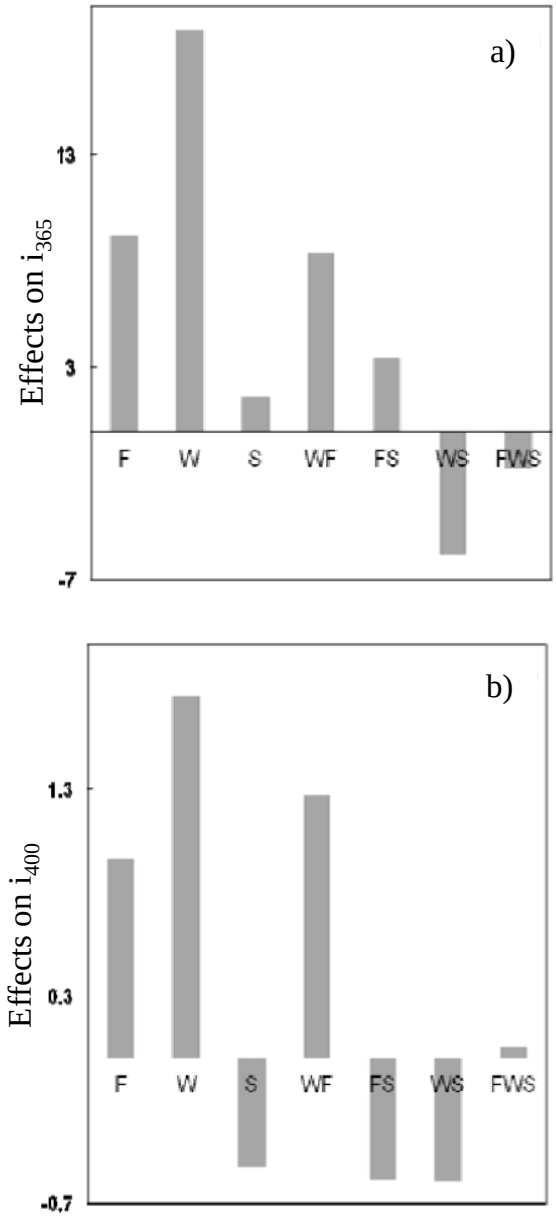

Figure 4.11. *Effects of the parameters and their interactions on the the photocurrent responses at λ=365 nm (a) and (b) at λ=400 nm. (F: fluoride concentration; W: water content; S: solvent)*

In order to quantify the related importance of these effects, the half-normal probability plot has been considered, in which all the ordered (largest to smallest) absolute values of the estimated effects for the main factors are reported. As an example, *Figure 4.12* shows the plot related to the i_{365} objective function. W is the most important effect, the related point being the only one displaced with respect to the linear trend. The analogous plot for the i_{400} function also indicated a relevant WF binary effect (data not shown).

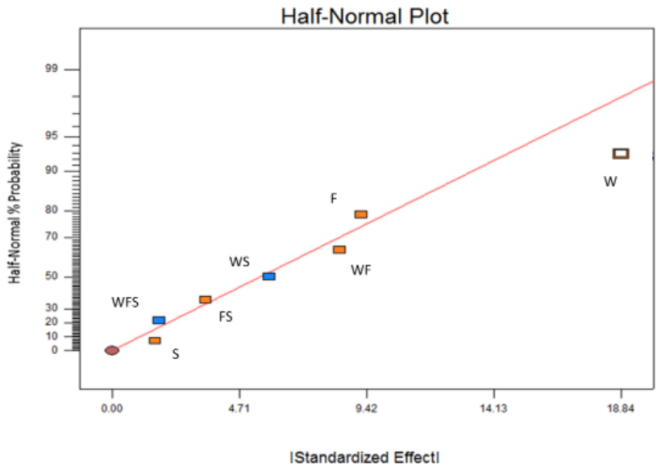

Figure 4.12. *Half normal probability plot of effects for the i_{365} objective function.*

On this basis, the study has been extended by obtaining new samples in which, other conditions being the same, the content of water in the electrolytic anodization bath was varied over a wider range as reported in *Table 4.3*. In particular, an intermediate percentage of water content was selected for samples obtained in EG, whereas two values were selected externally to the previously investigated range, for those obtained in G.

Table 4.3. *Anodization conditions for the three representative samples.*

Sample	Parameter / Unit		
	Fluoride Concentration / M	Water Content / vol%	Solvent / -
9	0.14	10	G
10	0.14	40	G
11	0.14	1	EG

The photocurrents measured at these samples under UV irradiation are reported in *Figure 4.13* along with the previous results as a comparison. Due to the different range of water content in the two solvents, data in *Figure 4.13*a) and *Figure 4.13*b) have been separately considered for G and EG, respectively. Also, photocurrents under white light were measured to test possible application of these samples in the visible range of light.

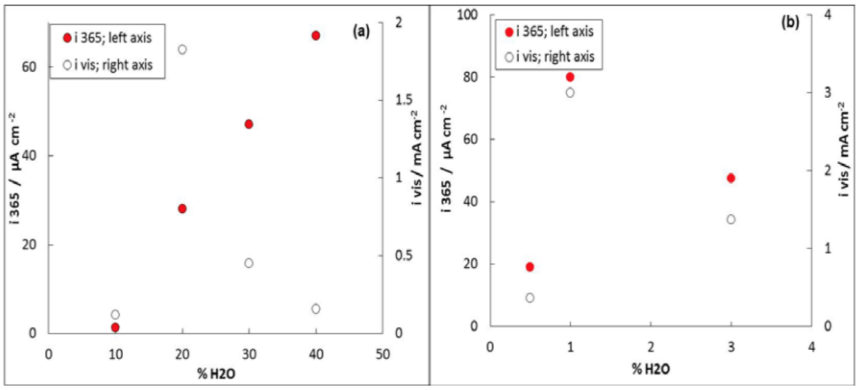

Figure 4.13. *Photocurrent values measured at λ=365 nm and under visible light for samples synthesized in G (a) and (b) in EG solutions with different water content.*

The data reported in *Figure 4.13* may suggest that a water content of about 1 vol% could be used in the bath EG solution to obtain samples performing well under UV and visible light. However, for the samples prepared in G, *Figure 4.13*a indicates that 20 % water content could be the best for samples working in the visible range. A better performance can be obtained under UV irradiation if the percentage of water is increased beyond the 40 vol% [142].

4.2.5 Conclusions

DOE analysis proved to be a useful and viable method to investigate the effects of different parameters on both the structure and the performance of nanotubular samples. The kind of solvent was the most important factor determining the aspect ratio of nanotubes, while water content was the most influential parameter on the photocurrent measured at samples in the UV range. Data indicated water content of about 1 vol% to be used in the ethylene glycol bath solution to obtain samples performing well under UV and visible light. For samples prepared in glycerol/water solution, 20 % water seems to be a good choice for visible light. The increasing trend of photocurrents obtained for samples prepared in glycerol with increasing water content, may suggest that inorganic solvents could be a better choice to obtain improved performance in the UV range.

On the basis of the results obtained from the data derived by the DOE technique, different considerations have to be taken into account in order to guarantee a good working of combined TiO_2-WO_3 systems, which are proposed in this Thesis as photoanodes in solar cells.

If the electrochemical deposition of WO_3 is considered, nanotubular structures with relative high pore diameter (low aspect ratio) are desirable, so that G seems to provide the required pore dimensions: high pore diameters are expected to favour the diffusion of the WO_3 deposition solution inside the nanotubular structures. In that way, larger surface area of the TiO_2 material will be in contact with the deposition solution, and therefore available during the electrodepositon of WO_3.

On the other hand, when the photoactivity of the samples under white light irradiation (i_{vis}) is considered, results indicate that for both the organic solvents higher photocurrents were achieved when low concentrations of water are used in the anodization bath solution. In particular, when G was used as organic solvent, a maximun photocurrent value was observed at a 20% of water content. Nevertheless, experimental studies have also evidenced that 20% or higher water content leads to an uncontrolled synthesis of the nanotubular structures, resulting in the formation of nanotubular layers with cracks and disordered structures. The excessive

generation of O_2 at the Ti foil during the anodization process may be the reason of this observation. This fact could be a limiting factor if a scale up of the oxidation process, to obtain the nanotubular structures, is considered.

Under these considerations, a solution containing a 90% of glycerol, 10% of water and 0.14 M of NH_4F was chosen for the synthesis of the nanotubular structures reported in the rest of this Thesis.

4.3 Scale up of the oxidation process to obtain TiO_2 or TiO_2WO_3 nanotubes

The basic properties of the nanotubular structures, such as regular architecture, straight path for photogenerated carriers and high specific surface, have confirmed the better performance of the TiO_2 tubular structures in the UV range of light, if compared to the compact oxide layer (see section 4.1). In those cases, a nominal 1 cm^2 of active surface was synthesized and the presence of nanotubes was assessed by the SEM analysis. However, if an uniform distribution of the nanotubular structures and a reproducible synthesis process is required, the manufacturing of TiO_2 nanotubes becomes even more difficult and not very suitable for large-scale applications. Up to date, most of the anodic oxide layers, both commercially available ones and academic, typically more highly ordered ones, are of limited size (on the order of several mm^2 or cm^2) [143]. A two-step procedure is reported in the literature for the preparation of TiO_2 photoanodes with an active area of 16 cm^2. The first step (anodization of Ti foils) is the synthesis of 16 discs (1cm^2) of TiO_2 nanotubes, which were then fixed on a porous layer by applying a small pressure [171].

However, this section reports the results of an experimental work in which an attempt is made to scale up the one-step anodization process for growing well-ordered TiO_2 or TiO_2WO_3 nanotubar arrays on large surface (15 cm^2 nominal surface). In particular, the feasibility of the shynthesis process was studied by testing the homogeneity of the titania nanotubular structures in terms of morphology and photoactivity.

4.3.1 Electrochemical cell design

The electrochemical anodization is a group of interconnected processes and factors, in which each one of them have its specific weight on the final morphology of the nanotubes and in turns, on the performance of the photoanode. The effect of anodizing parameters, such as anodization time [144], voltage [145], temperature [146] or the composition of the electrolyte [142], on the photoactivity of TiO_2 based electrodes have been studied by several authors. But it is also worth considering that the configuration of the electrochemical cell represents an important factor in the anodizing

procedure. For example, an adequate distribution of the electric field, which can be affected by the disposition of electrodes in the electrochemical cell, can strongly affect the uniformity of the morphology of the nanotubes. This requirement can be also considered a limiting factor during the anodization process, for the generation of highly ordered TiO_2 electrodes.

On the basis of these criteria, attention has been paid in the disposition between the Ti foil and the Pt grid as well as in the electric contact with the Ti foil; the design of the electrochemical cell was made in order to guarantee a favorable distribution of the electric field.

Figure 4.14 shows a schematic view of the two-electrode cell (made of Teflon), used to obtain the nanotubular samples, composed by one cylindrical chamber containing the electrolytic solution. Electrical contact with the Ti foil was realized by means of an aluminum disc (d=5 x h=0.5 cm) located at the bottom side of the cell. The electrode/electrolyte contact area was 15 cm^2 and the electrolyte volume was 30 mL. A platinum grid cathode with a circular-shape (ø44 mm x 1.5 mm) was set at a 1 cm distance, in front of the anode.

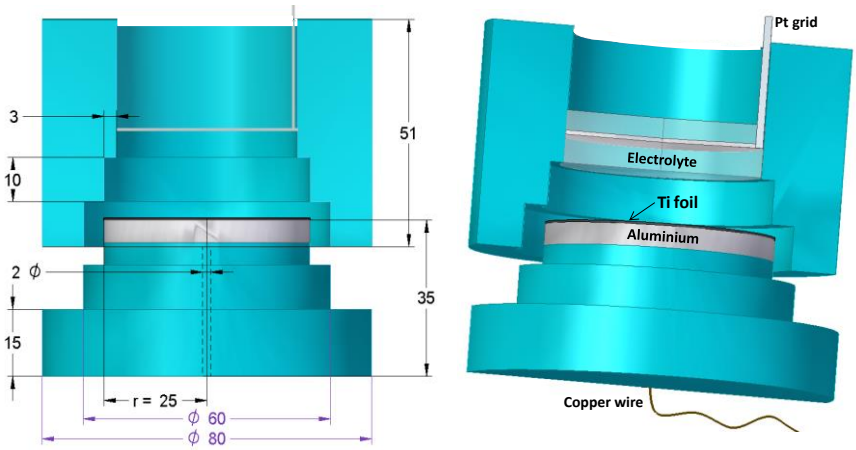

(Scheme of the electrochemical celll, figure 4.14)

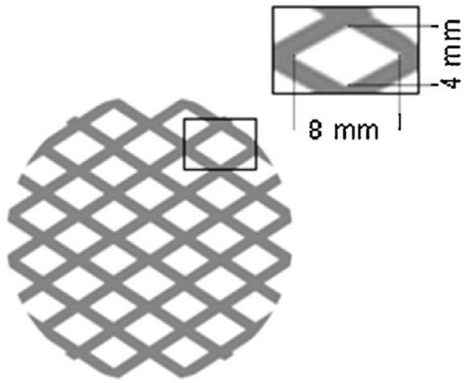

Figure 4.14. *Scheme of the electrochemical cell used for the synthesis of the nanotubular structures structures (dimensions are expressed in mm). Detail of the Pt grid is also reported in figure.*

4.3.2 Preparation of the TiO_2 Nanotubular structures on 15cm^2 of surface area: Ti/TiO_2 electrodes

The nanotubular structures were obtained following the procedure described in section 3.1.1.2. Briefly, disks of Ti of 5 cm diameter were used as the raw material. Prior to the electrochemical oxidation, Ti foils were degreased by sonication; finally, they were rinsed with deionized water and dried in a Nitrogen stream. Then, the Ti foils were electrochemically oxidized in the two-electrode cell described in Figure 4.14 at 20V for four hours (15 cm^2 of Ti nominal area in contact with the electrolyte). As explained in section 4.2.5, the composition of the electrolytic bath used to obtain the TiO_2 nanotubes was: (10%) H_2O / (90%) glycerol and 0.14 M of NaH_4F. Finally, the samples were rinsed with distilled water and annealed 1 h at 400°C in air in order to increase the crystalline structure of the materials.

The uniformity of the nanotubular structures and its photoactivity was also tested in a three-electrode cell: chronoamperometric tests and cyclic voltammetries were performed at 9 points of the obtained sample (see *Figure 4.15*) in 0.1M KOH electrolyte. A home-made teflon mask was used to individuate one point a time to be exposed to the electrolyte and to the irradiation. To prepared the teflom mask, a teflon foil of 5 cm of diameter

was holed (hole diameter 1.12 cm); then O-rings with different dimensions were fixed at one side of the holed teflon foil. The O-rings were used not to damage the nanotubular structures and also to limit the solution only to the section to be analysed (1 cm^2). During the characterization of the individual sections, the rest of the holes (not analysed sections) were covered in order to avoid the contact of the electrode surface with the electrolyte or the irradiation (see figure 4.15).

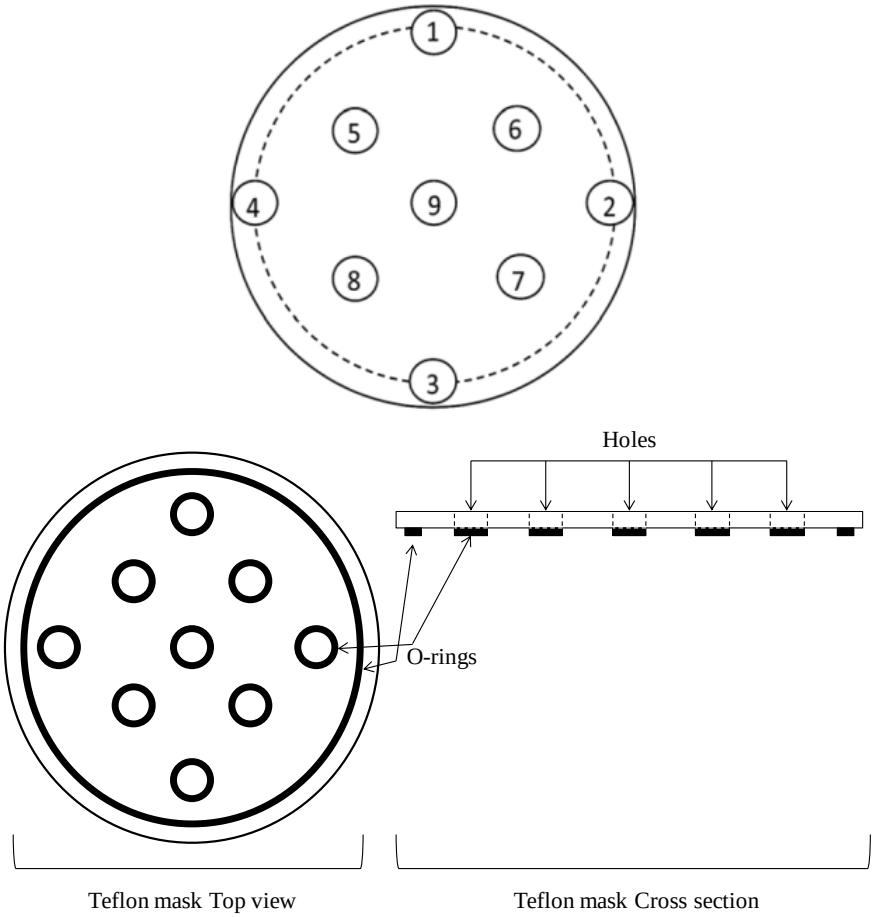

***Figure 4.15**. Investigated points of the synthesized sample of 15cm^2 of nominal area. Scheme of the Teflon mask used to individuate and characterized one section at time.*

4.3.3 Morphological Characterization: Uniformity of the nanotubular structures

The adopted electrochemical cell, described in the section 4.3.1, allowed us to obtain an electrode with an active surface of 15 cm^2. *Figure 4.16* shows some examples of the results of the SEM analyses performed at different points of the synthesized electrode in order to verify the uniformity of the nanotubular structures.

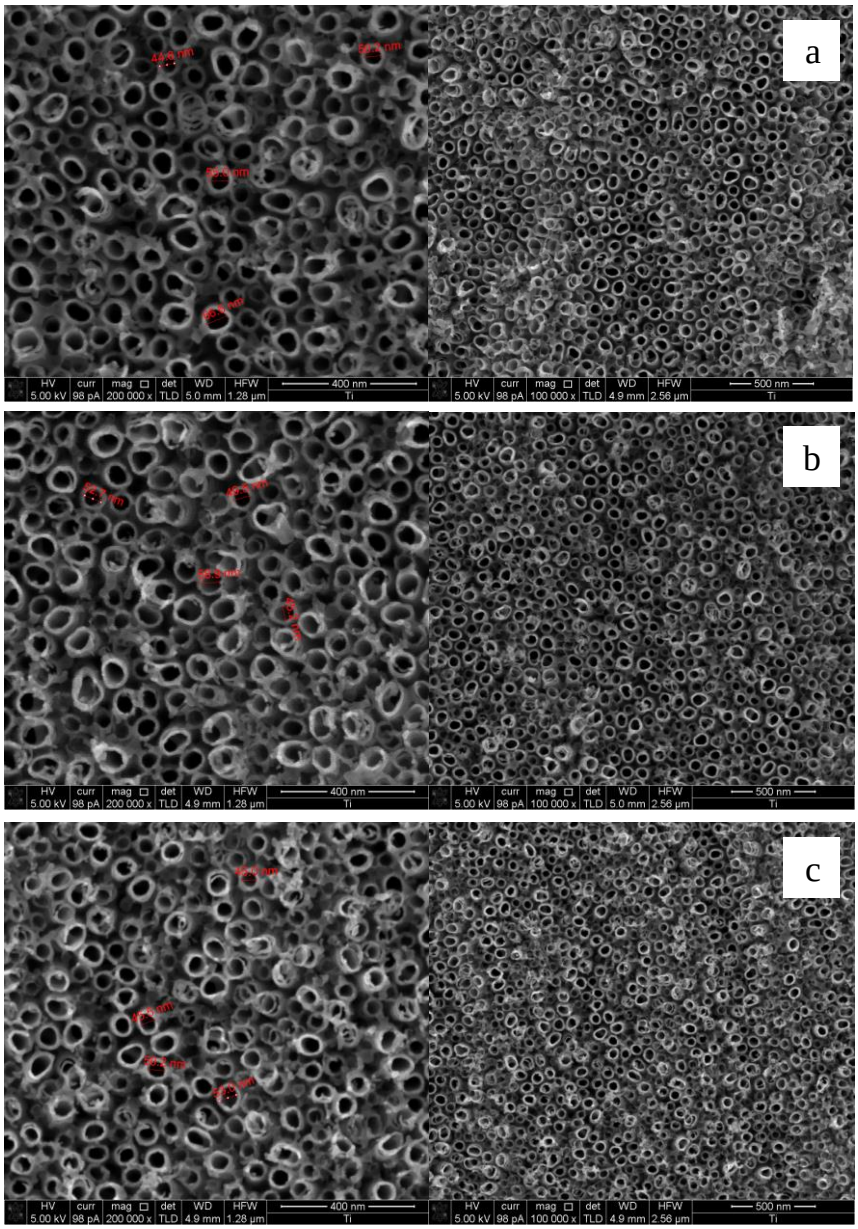

Figure 4.16. *SEM micrographs of synthesized sample at 3 investigated points, obtained at different magnifications: a) point 4, b) point 9 and c) point 2.*

If the border line effects are excluded (about 5mm corresponding to the thickness of the wall of the cylindrical cell), an almost regular structure of

the nanotubes was observed with a mean tube diameter around 50-60 nm measured in different points of the sample [147]. Similar results were also derived from the morphological characterization performed at different electrodes that were obtained under the same experimental conditions (data not shown). As shown in *Figure 4.17*, the average length of the nanotubes is 700 nm.

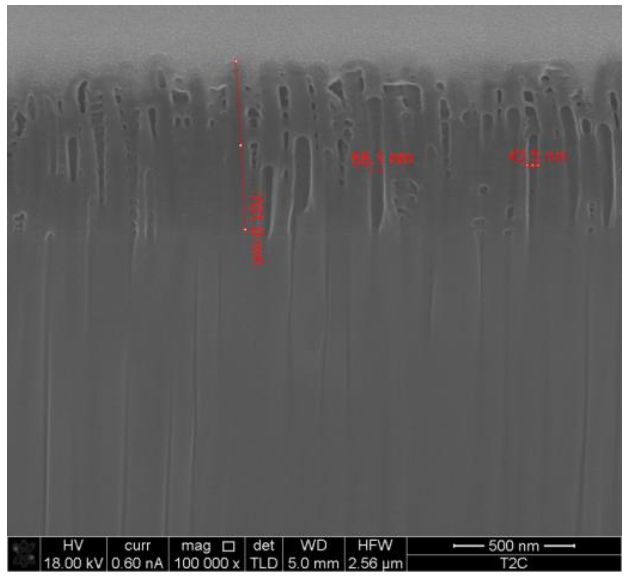

Figure 4.17. *SEM micrographs of FIB cross sections of the obtained TiO_2 nanotubes.*

4.3.4 Chronoamperometric and Voltammetric Tests

Specific runs were performed in which a teflon holed mask allowed one section a time to be exposed to the solution and to the irradiation of a Xenon lamp (nominal power: 300W). The photocurrent density values were recorded at the different individuated points of the active surface area when the sample was irradiated with white light.

Figure 4.18 resumes the values of photocurrent measured at the different points of the active surface. Also in this case is possible to observe a quite regular trend, most in the central part of the surface, while peripheral points 1,2,3,4 exhibit lower values: border effects are also visible from the data reported in *Figure 4.18*. However, in this case, the effect could result not

only from this reason, but also from a higher concentration of the light irradiation in the central part of the spot emitted by the Xenon lamp. Accordingly, the peripheral part of the disks can be eliminated, so that only the uniform central part of the samples will be used.

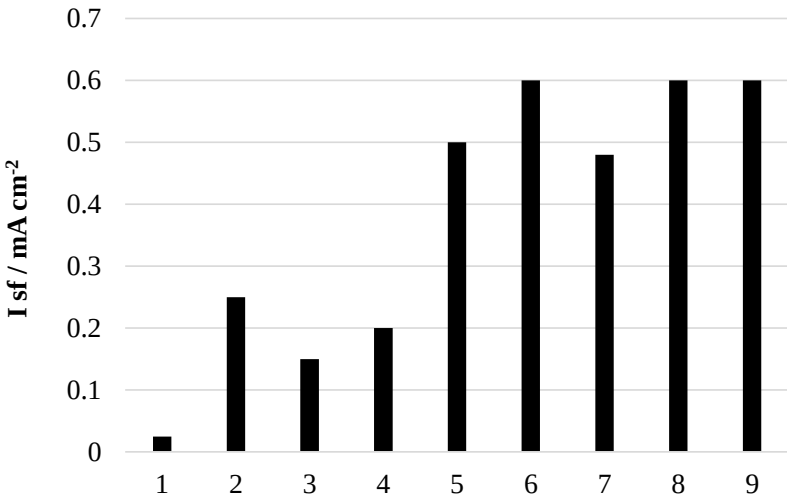

***Figure 4.18**. Photocurrents density distribution at the nanotubular sample obtained by irradiating with the Xenon lamp without filter (data obtained at the 9 investigated sections of the electrode).*

The photocurrent density values derived from different chronoamperometric tests, which were performed several times for the same analysed section of the electrode, demonstrated the reproducibility of the results.

Slight morphological differences observed in different points of the sample also resulted in a slight shift of the peak current densities in the cyclic voltammetries, as shown in *Figure 4.19*, while no variation of the peak potential position was observed; the peak may be attributed to the phase transition, T^{+4}/T^{+3}. Similar results were obtained at the different samples prepared under the same conditions, confirming a good uniformity and, overall, a good reproducibility of the synthesis [147].

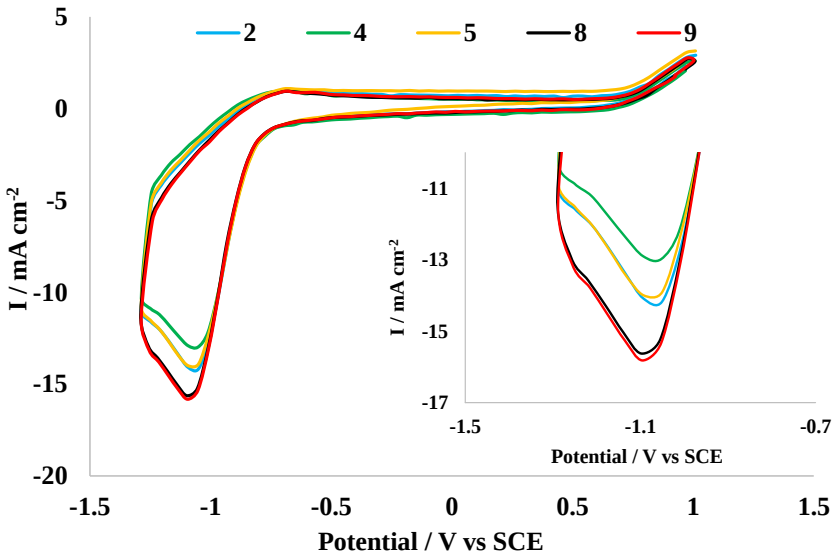

Figure 4.19. *Cyclic voltammetries of the notubular sample recorded in different points of the surface; scan rate: 100 mV* s^{-1}.

4.3.5 Conclusions

This section reports the results of an experimental work in which an attempt is made to scale up the process of oxidation of Ti foils, obtaining electrodes of 15 cm^2 nominal surface. The projected electrochemical cell allowed to obtain a photoanode constituted by a uniform array of TiO_2 nanotubes: the results confirm the quite regular structure of the samples, in terms of morphology and photoactivity. So that it is possible to obtain a uniform active area 15-fold larger than the one obtained in previous sections.

Such samples can now be exploited either as final electrodes for photoelectrochemical applications or as basic supports for the electrochemical deposition of WO_3. Moreover, the obtained results are encouraging and can be considered for a further scale up of the anodization process, and the use of the TiO_2 nanostructures electrodes on a scale that goes beyond the academic setting.

4.4 Combined systems: $Ti/TiO_2/WO_3$ electrodes

This section reports the results from the investigation on the photoelectrochemical properties of TiO_2-WO_3 mixed metal oxides, used as anodes for the photoelectrosplitting of water. TiO_2 is used as the support under-layer in form of either compact or nanotubular structure in order to analyze the role of the TiO_2 under-layer structure in the morphology of WO_3 deposits.

The synthesis of TiO_2 nanotubes was performed by Ti anodization using the projected electrochemical cell (see section 4.3.1), while the compact oxide was formed by thermal oxidation of Ti foil. The over-layer of WO_3 was obtained via cathodic electrodeposition, by means of pulse potential technique (PPT). The performances of the samples in neutral supporting electrolyte are compared when samples are irradiated with light at two wavelengths, 365 nm and 400 nm. The effect of the WO_3 loading on the performance and the charge transfer mechanism at the $Ti/TiO_2/WO_3$ electrodes are also investigated. The results from runs carried out in solutions containing glycerol are used to study the possible role of the WO_3 over-layer in the whole working mechanism of the combined structure.

4.4.1 Preparation of TiO_2 nanostructures: Ti/TiO_2 electrodes

TiO_2 compact oxide (CTO) and nanotubular TiO_2 structures were prepared as supports. CTO were obtained by thermal oxidation of Ti foils at 500 °C for 2h in air atmosphere, while the nanotubes were obtained by electrochemical oxidation, as previously explained in section 3.1.1.2, which allowed producing strongly adherent nanoporous layers on the Ti substrate. In particular, the oxidation process was performed in (10%) deionized water / (90%) glycerol organic solution with 0.14 M of NH_4F at room temperature. A potential ramp was imposed from the open circuit potential (OCP) to a fixed potential of 20 V with a scan rate of 100 mVs^{-1}. Then, depending on the samples, this potential value was kept constant for either 0.5 or 4 hours in order to obtain different dimensions of the nanotubes. In the rest of the text the two kinds of samples will be referred to as NT-05 and NT-4, respectively.

A final annealing treatment was required in order to transform the amorphous structure into a crystalline one (in air atmosphere at 400 °C for 1 h). For reasons of homogeneity of the nanotubular structures in terms of mhorphology and photoactivity, the peripheral part of the disks was cut, so that only the uniform central part of the samples was used (see section 4.3.4). The resulting structures were used either as final electrodes or as basic supports for the deposition of tungsten oxide; to obtain titania-tungsten oxide modified electrodes ($Ti/TiO_2/WO_3$).

4.4.2 Electrochemical deposition of WO_3

The electrodeposition of tungsten oxide was performed at room temperature in a classical three-electrode cell in which a platinum grid was the counter electrode. While the previously prepared supports were used as working electrodes, a saturated calomel electrode (SCE) was the reference. A PPT was used in order to obtain the oxide over-layer on the different substrates. During the PPT, the potential was alternated swiftly between open circuit potential (OCP) and -0.3 V. The details for the electrochemical deposition of tungsten oxide are explained in section 3.1.1.3.

Specific samples were also prepared in order to investigate the effect of the tungsten oxide amount on the photoactivity of the samples. For practical reasons, rather than progressively loading the same support, different samples (2 cm^2) derived from the same disk (15 cm^2) were used at which different loading times were applied. This procedure prevented the effects of the characterization tests of each deposit from somehow affecting the stability of the deposit itself, and its subsequent response to additional loading. NT-4 structure was selected for this kind of experiment: WO_3 deposition times from a few seconds up to 300 s were adopted (see section 4.4.7). The number of pulses required to reach the proposed deposition times was calculated according to the ON-time duration.

The obtained $Ti/TiO_2/WO_3$ modified electrodes were annealed in air atmosphere at 450 °C for 2 h.

Final samples on which deposits of tungsten oxide was obtained are indicated in the rest of the text as X/W_y, where "X" indicates the type of substrate and "y" the deposition time of the tungsten oxide, in seconds.

4.4.3 WO_3 electrochemical deposition process

As the synthesis of mixed oxide samples is considered, different mechanisms could be involved during the electrochemical deposition of tungsten oxide [81,148,149]. *Figure 4.20* depicts the trend of the charge passed during WO_3 deposition at the CTO, NT-05 and NT-4 samples, adopted as support in the present work; values between 0.07 and 1.85 C/cm^2 were calculated with respect to the nominal geometric area. A regular increasing trend of the electrical charge is measured for the nanotubular structures, which could correspond to an increasing in the amount and/or thickness of the oxide layer. However, the plateau measured at CTO could not be interpreted as a passivation state of the sample because, although charge is not increased, the deposition might have occurred through precipitation, due to possible pH gradients originated in the vicinity of the electrode surface [81].

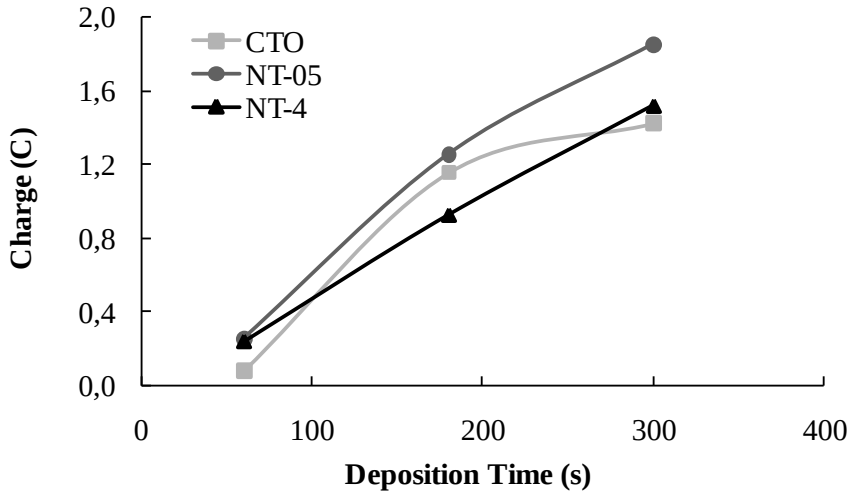

Figure 4.20. *Charge (C) passed during different WO_3 electrodeposition times at the CTO, NT-05 and NT-4 supports.*

The increasing amount of the deposit, obtained at NT-4 support is assessed by the results in *Figure 4.21*, where the trend of the linear sweep voltammetry (LSV), obtained in acidic solution is reported. At all the

tungsten oxide modified samples, two reduction peaks appear at -0.2 V and -0.45 V, the height of which increases in samples where WO_3 deposition time was higher. The two peaks may be attributed to the phase transition, W^{+6}/W^{+5} (peak I) and W^{+5}/W^{+4} (peak II), while the sharp increase of the cathodic current at -0.55 V may be related to hydrogen evolution [150].

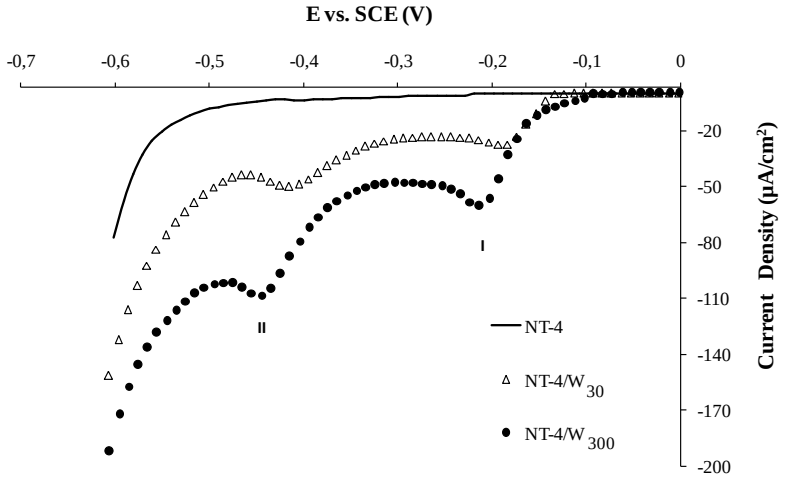

Figure 4.21. *LSV recorded at NT-4/W_y (y=30 and 300 s) in 0.1M HNO_3 aqueous electrolyte. The scan at NT-4 bare support is also reported as a comparison (continuous black line). Potential scan rate: 1mV s^{-1}. Data recorded under dark conditions.*

4.4.4 Raman measurements: analysis of the TiO_2 and WO_3 phases at the Ti/TiO_2/WO_3 electrodes

Figure 4.22 gives an example of the Raman spectra of NT-4 support, as a bare structure, or with 300 s of tungsten oxide loading. Data confirms that Anatase is the prevailing phase of the supports, while different phases are present in the tungsten oxide over-layer. In fact, the spectrum registered on the TiO_2 electrodes reveals the well-known Raman features of the Anatase phase: 144 (Eg)*, 197 (Eg), 399 (B1g)*, 513−519 cm^{-1} (A1g mode superimposed with B1g mode)*, and 639 (Eg)* cm^{-1}, with the strongest vibrations identified by asterisk [151]. As the support modified by tungsten oxide is considered, new peaks appear at about 270 and 320 cm^{-1}, and in

the 715 and 810 cm^{-1} range, due to the overlapping of the contributions from the different phases of tungsten oxide (bending and stretching vibration of the O–W–O modes).

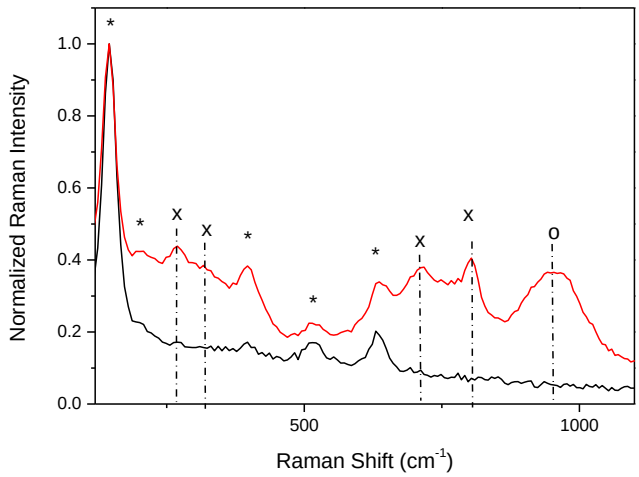

Figure 4.22. *Raman spectra of TiO_2 (black line) and NT-4/W_{300} (red line). (*) identifies the peaks from TiO_2 Anatase phase; (x) indicates the peaks related to WO_3 phases, while (o) indicates the Raman feature related to WO_5 and WO_6 phases.*

In particular, the features related to the WO_3 γ-phase (monoclinic, space group P21/n) and the β-phase (orthorhombic space group Pnma) are the most probable [152]. The presence of both phases is somewhat an expected result with the transition temperature (350 °C) being very close to the annealing temperature utilized (450 °C) [153,154]. The broad peak at about 950 cm^{-1} is not related to any phase of the WO crystal, but to the overlapping of defect modes related to the presence of other oxides in which tungsten has a higher coordination level (such as WO_5 or even WO_6) [155,156]. For this reason, in the rest of the text, the over-layer tungsten oxide will be indicated as WO_x.

4.4.5 Diffusive reflectance UV-vis spectra

Figure 4.23 reports the trend of the Kubelka-Munk function with photon energy, $(K\ hv)^{1/2}$ *vs hv*, recorder at the NT-4/W_{300}, NT-4/W_{60} and NT-4 samples.

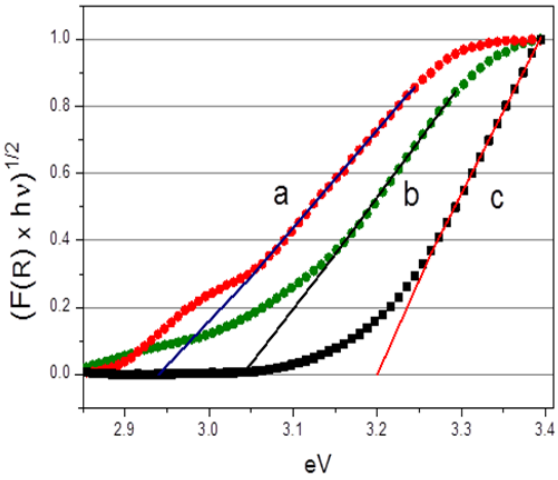

Figure 4.23. *Normalized Absorbance curves (F(R) * hν)$^{1/2}$ vs hν (eV) for the NT-4/W_{300} (a), NT-4/W_{60} (b) and (c) NT-4 electrodes.*

As it can be observed, increasing deposition times of the tungsten oxide, causes an apparent narrowing in the measured band gap. This behavior can be attributed to the different thickness of the tungsten oxide layer: a decrease of the band gap from about 3.05 to 2.6 eV was reported, when the thickness of the WO_3 layer passed from 200 to 1400 nm [82].

Moreover, a second active zone (see *curve a* in *Figure 4.23*) in the spectrum region of low energies (*hv* < 3.05 eV) is observed at highly loaded sample, that could be due to intra-gap states, related to the different oxide species (evidenced by the Raman spectra), which can be differently involved depending on the wavelength considered. However, an increase of the incident light absorption capacity is not directly related with an increase of the system photoactivity. In fact, to improve the photocatalytic response of

the material, low recombination rates between the photogenerated charges and good charge transport capability are also required [157].

4.4.6 Morphological characterization

In order to investigate on the possible effects of the substrates, *Figure 4.24* shows an example of the morphology of the compact and nanotubular structures used as support for the subsequent WO_x deposition.

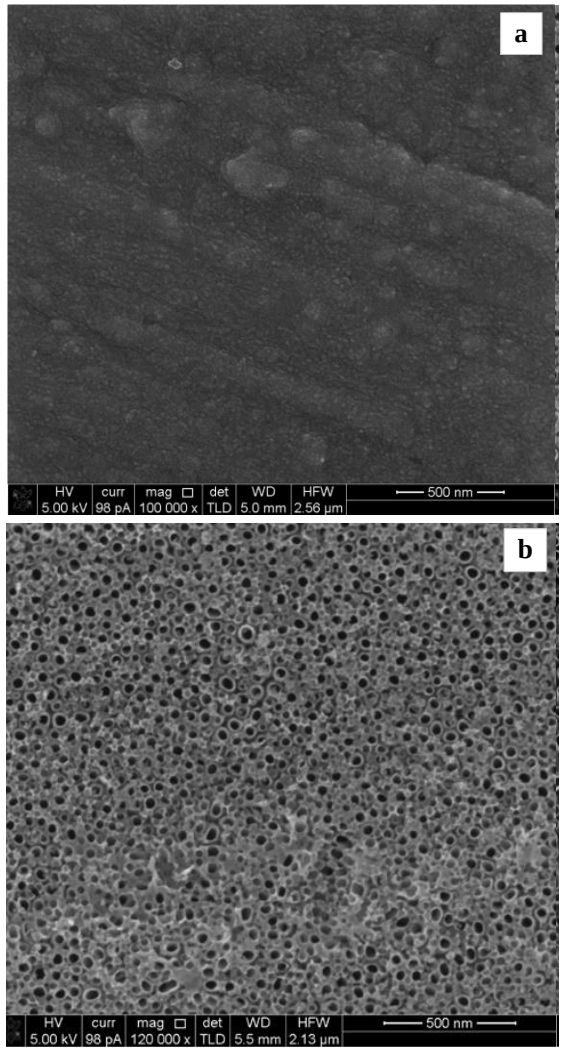

(SEM micrographs of TiO_2 bare supports, see figure 4.24)

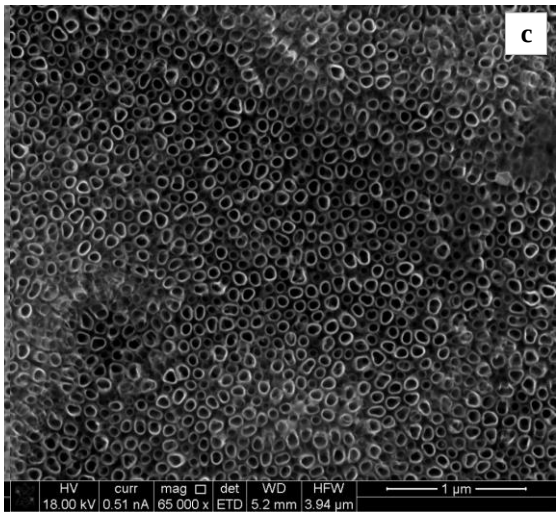

Figure 4.24. *SEM micrographs of TiO_2 bare supports: CTO (a), NT-05 (b) and (c) NT-4.*

A granulated structure is revealed at CTO, while nanotubes of different dimensions (mean diameter ranging from 20 to 80 nm) were obtained depending on the oxidation time. Moreover, an enhancement in the uniformity of the pore distribution, as well as in the definition of the nanotubular structures was observed at longer anodization times (*Figure 4.24*c). According to the literature [158–160], experimental conditions such as kind of electrolyte and anodization time may actually influence both the diameter and the length of tubes: in the present case the average length of the nanotubes increased from about 200 to 600 nm with increasing anodization time from 0.5 to 4 hours (*Figure 4.25*).

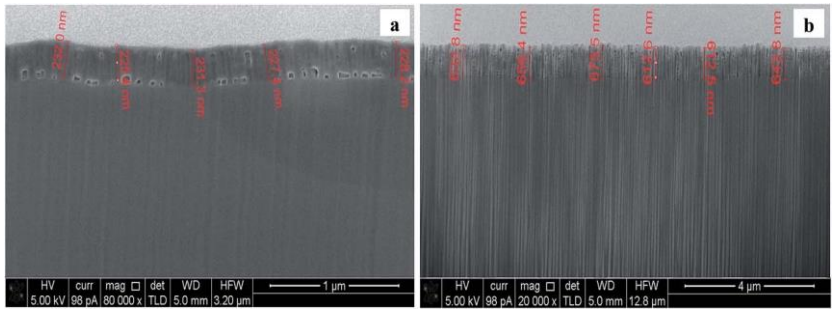

Figure 4.25. *SEM micrographs of FIB cross sections of the TiO_2 nanotubes obtained at the NT-05 (a) and (b) NT-4 supports.*

The nature of the substrate can influence the eventual size and shape, as well as the final electrodeposition efficiency [161]. SEM micrographs of the relative WO_x deposits obtained at the different supports are reported in*Figure 4.26*: a high loading of tungsten oxide is considered (y = 300 s) to have a better picture of the morphology. A predominant compact tungsten oxide layer is representative of the CTO/W_{300} sample (*Figure 4.26a*). A full coverage of the initial nanotubular structures is observed for both nanotubular samples (*Figure 4.26b* and *Figure 4.26c*), at which different crystal shapes are observed: the deposit at the NT-05/W_{300} sample growths as 2D nanoplates like crystals, which remains fairly distinguishable during deposition time, while an aggregation of spherical nanoparticles is observed at the NT-4/W_{300}.

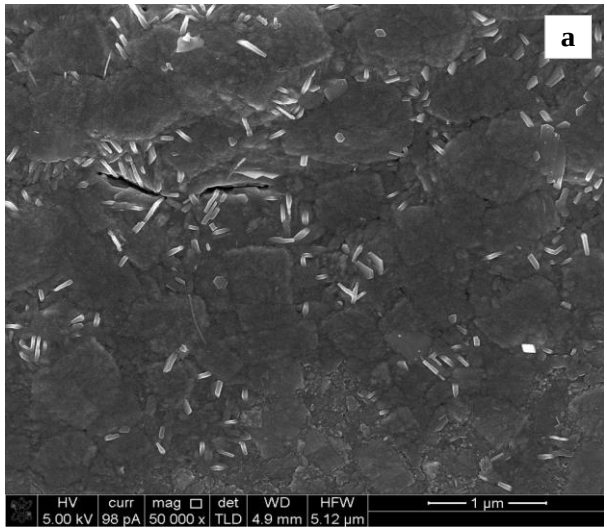

(SEM micrograph of WO_x modified supports, see Figure 4.26)

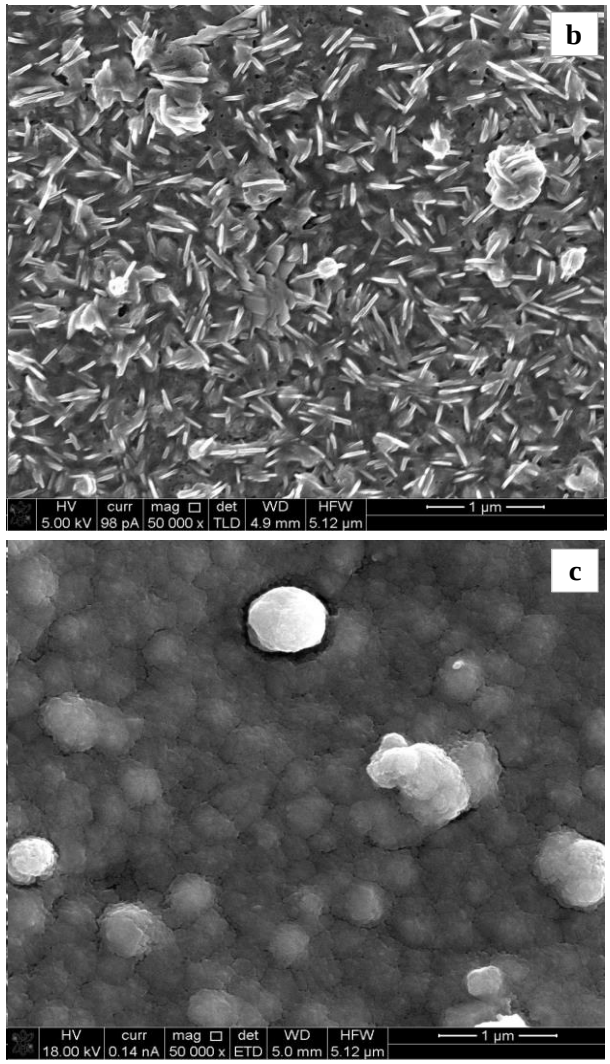

Figure 4.26. *SEM micrographs of WO_x modified supports: CTO/W_{300} (a), NT-05/W_{300} (b) and (c) NT-4/W_{300}.*

The elemental map of the NT-4/W_{300} sample along with the corresponding SEM micrograph is reported in *Figure 4.27*. As expected, it was verified that the main component of the WO_x deposit obtained was tungsten.

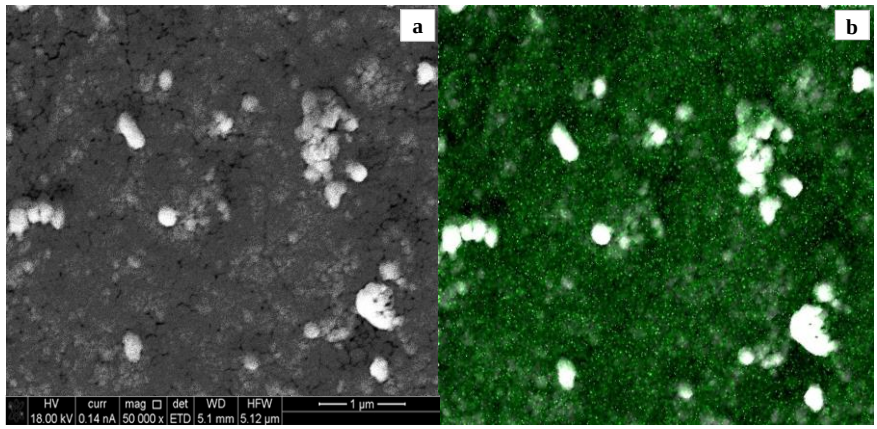

Figure 4.27. *SEM micrograph of the NT-4/W_{300} scanned area (a) and (b) elemental map of the tungsten (green dots) at the WO_x deposit.*

4.4.7 Photoactivity of the synthesized samples

As the photoactivity is concerned, *Figure 4.28*, shows an example of the polarization curves obtained at a WO_x modified sample: in all the cases, negligible current values are observed under dark conditions, while the working of the structure is assessed under illumination. The NPC reaches a saturation value at about 0.3 V, while oxygen evolution starts to occur at a potential higher than 1.4 V. The inset of the same figure reports an example of a chronoamperometric test performed at 0.5 V of overpotential from the OCP, from which the values of NPC were derived for the comparison of the performances of the different samples.

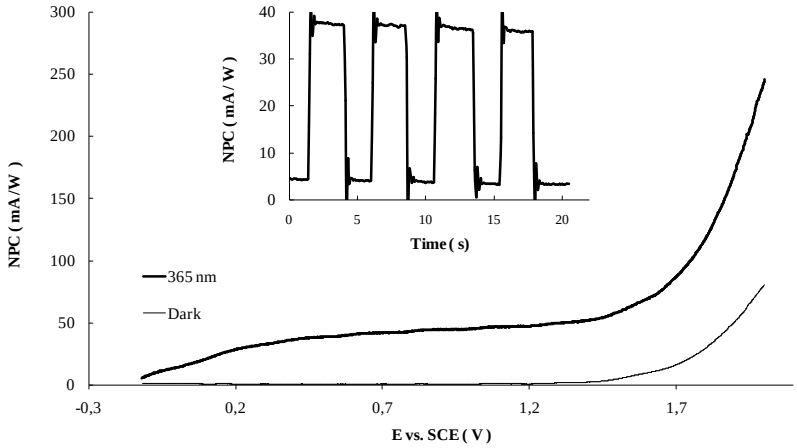

Figure 4.28. *Example of the Polarization curves recorded at NT-4/W_{10} in a 0.1M KNO_3 aqueous electrolyte. The potential was ramped (10mV s^{-1}) from the OCP to 2V; Inset: example of the chronoamperometry test performed at the NT-4/W_{10} sample. Data recorded under irradiation (365 nm) and dark conditions.*

Data resumed in *Table 4.4* also demonstrate that samples are photoactive, regardless the kind of support where WO_x is deposited.

Table 4.4. *NPC values (mA/W) for the bare (CTO, NT-05 and NT-4) and modified supports (CTO/W_{300}, NT-05/W_{300} and NT-4/W_{300}) obtained at 365 and 400 nm in 0.1 M KNO_3.*

Sample	CTO	CTO/W_{300}	NT-05	NT-05/W_{300}	NT-4	NT-4/W_{300}
NPC_{365} (mA/W)	3,02	0,99	7,57	1,60	11,83	6,80
NPC_{400} (mA/W)	0,36	0,27	0,63	0,27	0,93	2,11

The observed behavior seems to be in contrast with that expected for the $Ti/TiO_2/WO_x$ combined structure (see section 2.5). With this disposition, if the photogenerated charge transfer mechanism were only determined by the reciprocal position of the energy levels of the band edges of the semiconductors, the activity of the combined structure could be negatively

affected. Transfer of electrons accumulated in the CB of WO_x, towards the counter electrode, and the capture of holes in the VB of the TiO_2 by electron donors in solution could be difficult, in particular at high WO_x cover levels, when the inner surface of the nanotubes is not easily reachable by the electrolyte, or the TiO_2/electrolyte interface is limited.

Two factors may determine the observed behavior of the $Ti/TiO_2/WO_x$ electrodes. Actually, when a suitable light irradiates the WO_x particles that cover the TiO_2 sites, an increase of the quasi-Fermi level of WO_x may be originated by the injection of electrons in its CB, and this could reverse the charge transfer mechanism (*Figure 4.29a*). But also, it is worth to consider the porous structure of nanotubular support may play an important role. Due to the high concentration of defects which may be present at the surface of nanotubes [162], the interlayer between the two semiconductors may result quite conductive, so that also a Z-mechanism could activate the charge transfer (see section 2.6.3.1). In this way electrons left in the CB are free to be sent to the Ti substrate (to which the anodic potential is applied), and in turn to the counter electrode. In the meanwhile, free holes in the VB of WO_x may oxidize water (*Figure 4.29b*). Depending on the wavelength, one or both the mechanisms could be active in determining the charge transfer flow at mixed oxide sites. Obviously, at TiO_2 not covered by WO_x, the charge transfer can occur, by the mechanism expected at n-type semiconductors, by which holes are made free at the VB, to react with the electrolyte, provided it is able to contact the electrode interface.

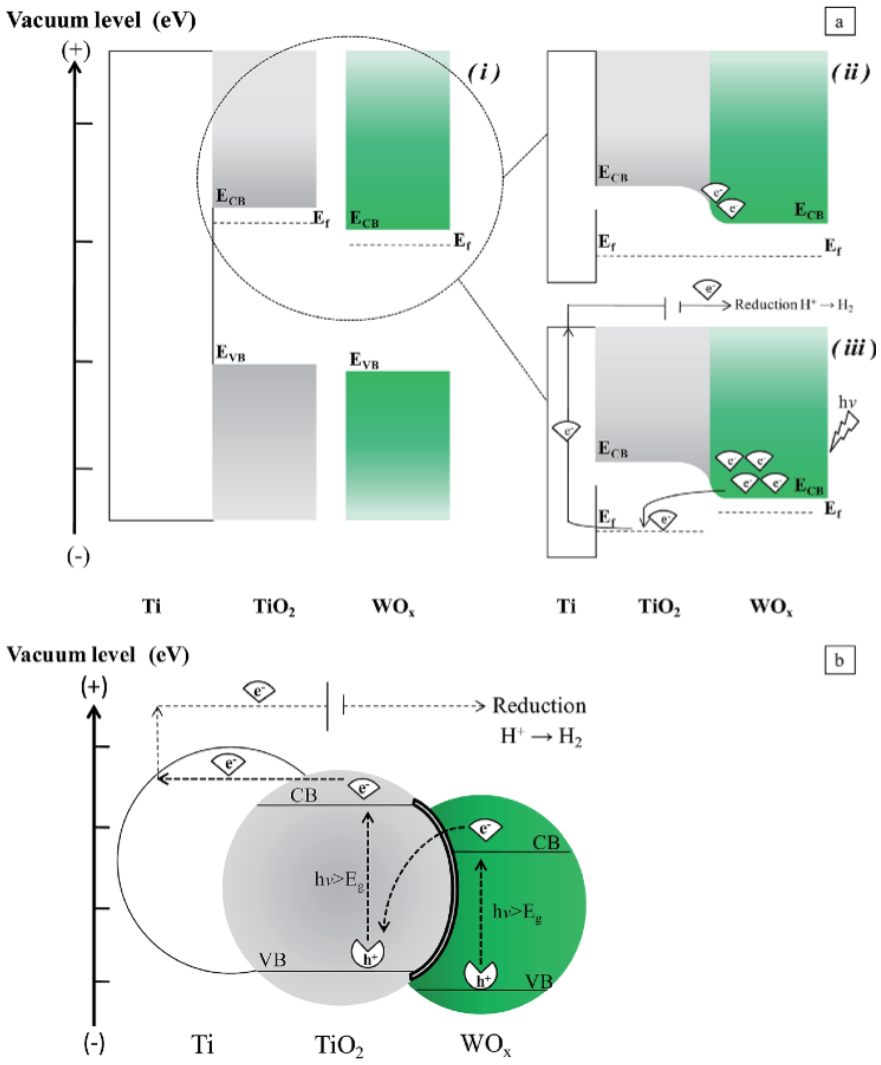

Figure 4.29. *Scheme of the proposed charge transfer mechanisms at Ti/TiO_2/WO_x. (a): shift of quasi-Fermi level: before (i) and after (ii) the contact of the phases, under dark conditions;(iii) under irradiation. (b): Z-scheme.*

Some further consideration may be done, on the basis of data in *Table 4.4*. If the data of bare TiO_2 are considered, since the heterogeneous character of the involved reactions, as confirmed in *section 4.1*, when passing from compact to tubular structure, a significant enhance of the performance is obtained, mainly due to the high specific area of the porous nanotubular

support; also, a faster charge transport can be achieved, so that an enhancement in the photocurrent is observed. Moreover, data evidence the benefit of using the well-defined nanotubular structures, also as the supports in the combined oxide samples: at both wavelength values, the longer the oxidation time in the synthesis of nanotubes, the higher the measured photocurrent in the resulting sample. However, when compared with the relevant bare supports, the behavior of the mixed oxide samples was not so encouraging. Actually, adding the second oxide resulted to be convenient only at NT-4 support and at 400 nm of light wavelength.

However, it must be observed that high coverage level was achieved in all samples in *Table 4.4*, so investigation on the effect of the amount of WO_x, kind of support being the same, was further undertaken. To this aim, the best performing structure, with the most regular deposition curve (NT-4, see *Figure 4.20*), was selected as support: deposition times were ranged from 2 s to 300 s. *Figure 4.30* resumes the results obtained at the two wavelengths.

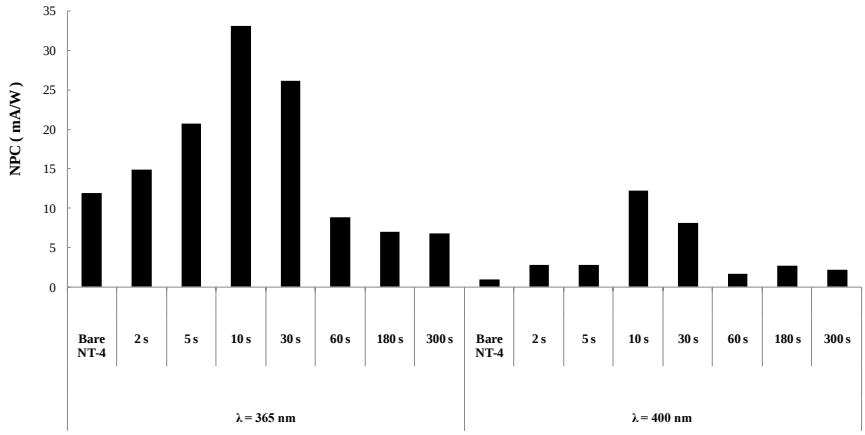

Figure 4.30. *NPC (mA/W) for the bare and WO_x modified NT-4 samples. Data obtained at 365 and 400 nm in 0.1M KNO_3.*

Similar trends of photocurrents were observed at the two wavelengths, confirming that in both the cases, an optimum in the deposit was reached, at which the use of mixed oxides was convenient: the sample treated for 10 s resulted the best performing at both the wave lengths. As shown in *Figure 4.31a*, at the beginning of the electrodeposition process (5 s), the WO_x

particles seem to be deposited around the walls of the TiO_2 nanotubes. After 10 s, the SEM analysis (*Figure 4.31b*) indicated that at the NT-4/W_{10} sample the nanotubular structure is still evident, deposition of WO_x occurring mostly at the walls of tubes. However, longer deposition times generate a cracked compact layer of WO_x at the top of the nanotubes (*Figure 4.31c*).

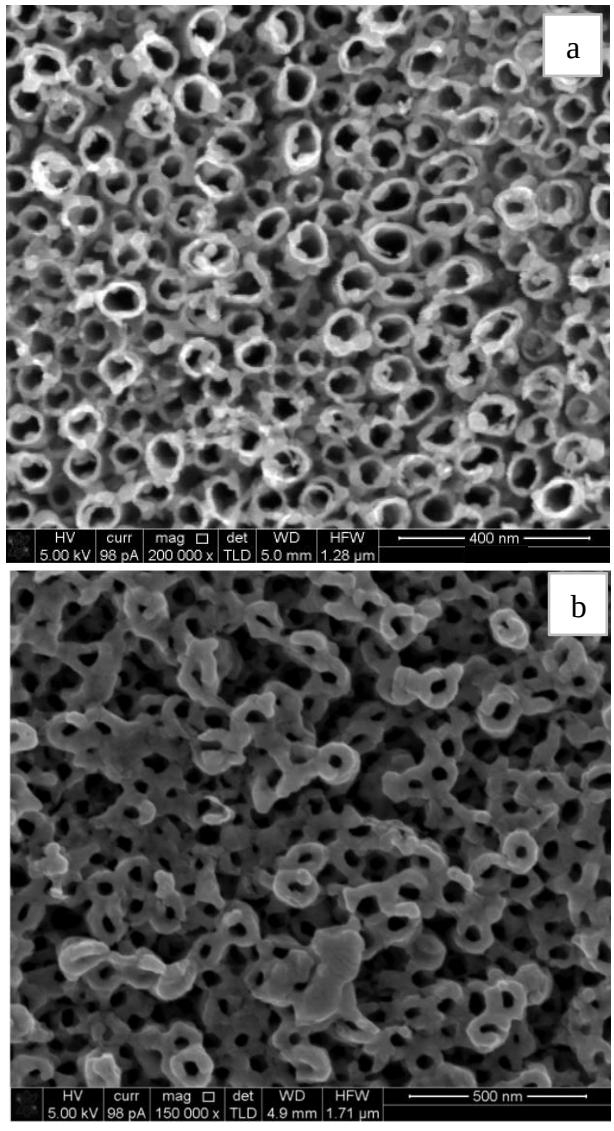

(Sem micrographs of the NT-4/W_5 and NT-4/W_{10} samples, see figure 4.31)

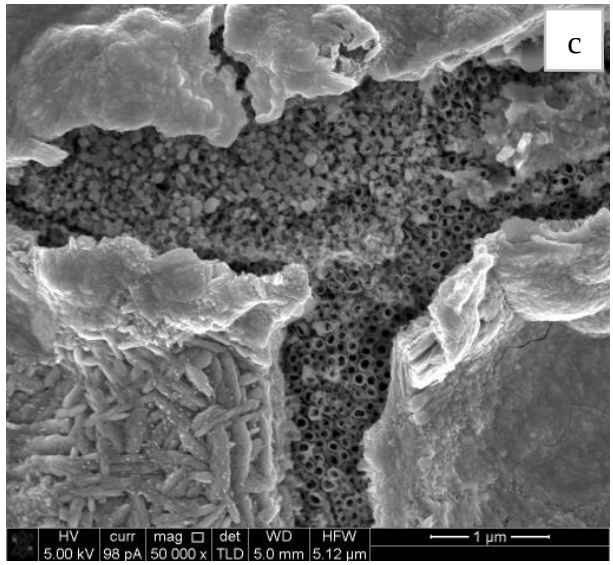

Figure 4.31. *SEM micrographs of the NT-4/W_5 (a), NT-4/W_{10} (b) and (c) NT-4/W_{300} electrodes.*

The negative effect observed at higher loading could be due either to an increase in the CR, or to a decrease in the specific area of the electrode: plugging of NTs by WO_x particles could reduce the TiO_2/electrolyte interface.

4.4.8 Indications about the charge recombination: Use of glycerol as hole scavenger

On the basis of the photocurrent data reported above, an investigation was performed on the photoactivity in the presence of a hole scavenger, such as glycerol, allowing for the derivation of indications on the mechanism of the charge recombination (CR) at the Ti/TiO_2 and Ti/TiO_2/WO_3 electrodes.

Figure 4.32 compares the performances, in terms of photocurrent, obtained in the presence of glycerol when the NT-4/W_y samples were irradiated at 365 nm and 400 nm. Data related to the bare NT-4 support is also reported in the graphs as a comparison. To make the comparison straightforward, the parameter γ has been introduced, defined as the ratio between the values

measured in the presence of the scavenger and in the supporting electrolyte. This parameter can be considered as a measurement of the CR in the original sample: a high value of γ indicates the beneficial effect obtained by adding glycerol, which was able to scavenge the holes.

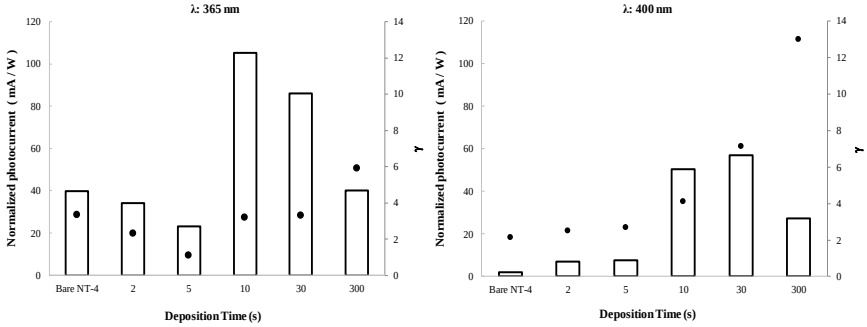

Figure 4.32. *NPC (white bars) at NT-4 and NT-4/W_y samples, measured at 365 and 400 nm in 0.1M KNO_3 / 10% glycerol electrolyte. γ values (black points) are defined as ratio between the photocurrents measured in the presence of the scavenger and in the supporting electrolyte.*

In all the experimental conditions, in the presence of glycerol, a significant enhancement of the performance of all the samples was observed (γ>1), indicating a strong effect of the scavenger at both investigated wavelengths. The γ value at NT-4/W_{300} could give an indication of the extent of the recombination at WO_x: as indicated by the SEM analyses (*Figure 4.31b*), at this deposition time, all of the NT-4 nanotubular structure is covered by the WO_x layer, so that it is the only phase contacting the electrolyte. A comparison between γ values at NT-4 and NT-4/W_{300} indicates that at both the wavelengths, CR at WO_x is higher than at TiO_2. Although WO_x is able to absorb the radiation, a high concentration of defects, which act as CR sites, could be the reason of this result [163].

However, if the trend of γ is considered as the WO_x loading is increased (*Figure 4.32*), a different importance of the CR may be derived at the two wavelengths. At 400 nm, the TiO_2 substrate has a negligible photoactivity with respect to that of WO_x: an initial nearly constant trend of γ is

calculated, then its value is nearly doubled after the first 10 s of deposition, and it further increases for samples with higher loading. In this case, although the addition of small amounts of WO_x involves a benefit in terms of photocurrent, it does not seem to affect the performance of the sample in terms of CR. In fact, the nearly constant γ values, observed at low WO_x coverage, indicate that the increase of the recombination sites due to the WO_x deposit, is negligible compared to original CR at the surface of TiO_2.

At 365 nm, when the incident light activates both the phases, a minimum may be observed. Two contrasting effects can be considered to justify this trend: on the one hand, at low coverage levels, the presence of WO_x reduces the CR due to the possible interactions between electronic bands, as described above, which allows a higher separation of the photogenerated charges. By contrast, as the coverage level increases, the TiO_2 surface is being partially covered by a less active material (WO_x): CR at WO_x becomes the prevailing negative effect. Thus, after a certain coverage degree, when all the TiO_2 nanotubular structure is practically covered, WO_x is the only phase in contact with the electrolyte. In such a situation, the decrease in the photocurrent in KNO_3 (*Figure 4.30*) at both wavelengths may be mainly due to a decrease in the electrode active surface. The increase in the γ values indicates that, for these loadings, high WO_x deposit amounts also results in a significant increase of recombination sites: actually, for these samples the positive effect of glycerol is the highest.

4.4.9 EIS analysis of the best performing sample: NT-4/W_{10}

Further information about the charge transfer at the best performing sample was obtained from the P-EIS measurements in the presence and absence of glycerol. The relevant impedance spectra of the NT-4 and NT-4/W_{10}, under illumination (λ= 365 nm and 400 nm), measured at the open circuit potential are shown in *Figure 4.33* in terms of Nyquist plots. Two semi-circles are generally identified, respectively at the high and medium frequency region. Depending on the case, a third element appeared in the impedance spectra.

As a qualitative comparison is concerned, at both the wavelengths, the P-EIS spectra recorded at the combined system (NT-4/W_{10}) are lower than that related to the single phase (NT-4), which suggests that the presence of WO_x at the NT structure enhances the TiO_2 phase performance. Moreover, for both the investigated samples, the positive effect of glycerol is evidenced: lower P-EIS data are obtained in the presence of the scavenger, with respect to those obtained in the absence of the organic solute.

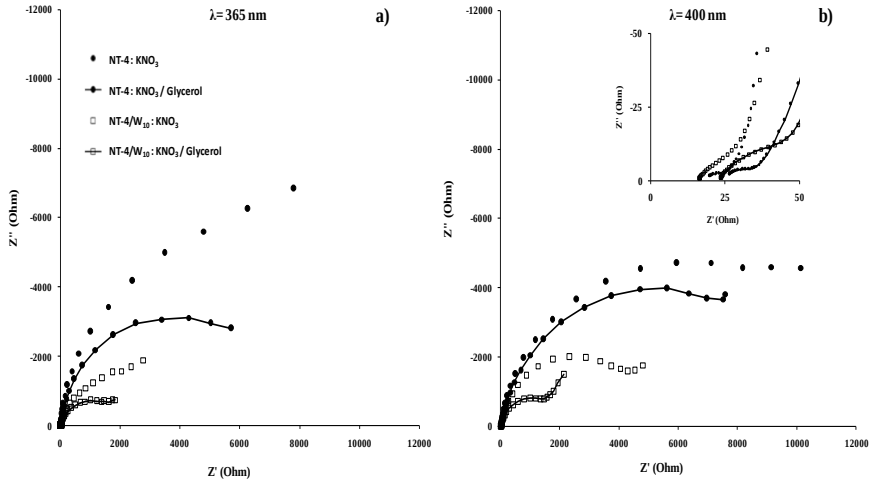

Figure 4.33. *Nyquist plots of the NT-4 and NT-4/W_{10} samples obtained at the open circuit potentials at 365(a) and (b) 400 nm in 0.1M KNO_3 or 0.1M KNO_3 / 10% glycerol electrolytes.*

The quantitative analysis of the data was performed using the equivalent circuit approach. Two electric circuits were selected to fit the P-EIS data derived from the measurements performed at the NT-4 and NT-4/W_{10} samples, and to obtain the circuital parameters. *Figure 4.34a* shows the equivalent circuit employed to describe the NT-4 behavior: two RQ elements in series with a R_s, correlated with the solution resistance (mean value around 20 Ω), were employed to describe the performance of the NT-4 sample. Constant phase elements, CPE ($1/Z= Q(j\omega)^n$), rather than perfect capacitance were used, where the displacement from unity of the exponent

"*n*", accounts for the non-ideality of the capacitor. In the presence of the second oxide (WO_x), an additional impedance, a Warburg element, was needed to fit the data at the lowest frequencies for the NT-4/W_{10} system (see *Figure 4.34b*)

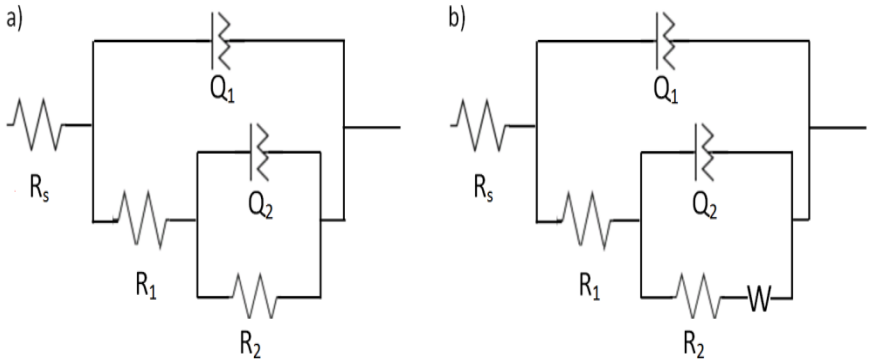

Figure 4.34. *Equivalent circuits used to fit the EIS data obtained at the open circuit potentials under irradiation conditions (365 and 400 nm) in 0.1M KNO_3 or 0.1M KNO_3 / 10% glycerol electrolytes for the NT-4 (a) and (b) NT-4/W_{10} samples.*

The parameters of the proposed circuits are summarized in

Table ***4.5***. The time constants values, calculated a $\tau_1 = (R_1 Q_1)^{1/n_1}$ and $\tau_2 = (R_2 Q_2)^{1/n_2}$, also reported in the same table, allowed to individuate the different steps involved in the processes.

Table 4.5. *Circuital parameters values derived from the fit of the EIS data obtained at the NT-4 and NT-4/W_{10} samples under irradiation (365 nm and 400 nm).*

Sample NT-4										
Electrolyte Solution	**Wavelength**	**R_1**	**Q_1 x 10^5**	**n_1**	**τ_1 x 10^3**	**R_2**	**Q_2 x 10^5**	**n_2**	**τ_2**	
	nm	**Ω cm^2**	**$S{\cdot}s^n cm^{-2}$**		**s**	**Ω cm^2**	**$S{\cdot}s^n cm^{-2}$**		**s**	
0,1M KNO_3	365	19,1	9,1	0,72	0,14	28313	29,1	0,98	8,64	
	400	22,8	6,2	0,69	0,07	24000	9,9	0,96	2,46	
0,1M KNO_3/ 10%Glycerol	365	31,3	9,7	0,78	0,56	13804	32,4	0,97	4,72	
	400	33,9	5,3	0,67	0,08	18750	10,3	0,90	2,08	

Sample NT-4/W_{10}										
Electrolyte Solution	**Wavelength**	**R_1**	**Q_1 x 10^5**	**n_1**	**τ_1 x 10^3**	**R_2**	**Q_2 x 10^5**	**n_2**	**τ_2**	**W**
	nm	**Ω cm^2**	**$S{\cdot}s^n cm^{-2}$**		**s**	**Ω cm^2**	**$S{\cdot}s^n cm^{-2}$**		**s**	**S $s^{1/2}$**
0,1M KNO_3	365	35,7	22,5	0,71	1,18	4393	85,3	1	3,75	0,00470
	400	40,9	5,8	0,80	0,52	6696	19,2	1	1,28	0,00269
0,1M KNO_3/ 10%Glycerol	365	48,4	20,3	0,69	1,20	2093	61,8	1	1,29	0,00447
	400	67,6	10,3	0,70	0,85	2128	40,5	1	0,86	0,00282

According to the data shown in
Table 4.5, R_1Q_1 can be related to the CR process occurring at the bulk of the semiconductor material: under the experimental conditions adopted in this work, the related time constants (τ_1) values in the order of milliseconds were actually obtained, which are consistent with the lifetime of the photogenerated charges [164].

The time constants (τ_2) related to the R_2Q_2 element indicate a slower process, which may be referred to a charge transfer process, at the electrode/electrolyte interface. Therefore, the R_2 can be described by a charge transfer resistance (R_{CT}) [165].

In the case of the NT-4/W_{10} sample, the Q_2 is a perfect capacitor (n=1), and the related τ_2 decreases if compared to the values obtained at the bare support. However, the presence of a third element (Warburg impedance) in the equivalent circuit may evidence the existence of diffusion effects, perhaps caused by the presence of WO_x nanoparticles inside the nanoporous structure, which may limit the diffusion of the electrolyte within the nanotubes.

The obtained results confirmed that both the recombination resistance (R_1) and the lifetime of the charges (τ_1) increase at both the wavelength when WO_x is present in the sample, and a further increase is observed, especially at 400 nm when glycerol was used as hole scavenger. Lower R_{CT} values are obtained when the combined structure was used: a better separation of the photogenerated carriers may lead to a greater availability of holes for the oxidation of either water or organic compound, which can be confirmed by

the subsequent decrease of R_{CT} values in the presence of the scavenger. τ_2 data also confirms a faster charge transfer process occurring at the NT-4/W_{10} surface/electrolyte interface (rather than the one observed at the NT-4 sample), and especially the improvement due to the presence of glycerol which acts as scavenger.

4.4.10 Conclusions

The presented results gave evidence on the effectiveness of combining tungsten oxide with well-developed TiO_2 nanotubes. However, a real benefit is obtained only if a partial coverage by the WO_x is maintained, whereas at the highest coverage degree, the prevailing effects are the increasing of charge recombination at WO_x, and the decreasing extent of the interface electrode/electrolyte, due the plugging of nanotubes.

The NT-4/W_{10} was individuated as the best performing sample, which at both the wavelengths represented a good compromise to obtain high photocurrents in KNO_3, keeping CR as low as possible.

Taking into account for both the light and the anodic potential to which the samples are submitted, the benefit obtained at the Ti/TiO_2/WO_x electrodes, has been explained as due to two main mechanisms.

On one hand, the Z-scheme may be activated thanks to the conductive nature of the nanotubular surface. It may constitute a suitable interlayer which activates a charge transfer mechanism, allowing electrons at TiO_2 CB and holes at WO_x VB, to be transported to the counter electrode, or available for the electrolyte, respectively. Such a mechanism may be the most favored under the irradiation of λ=365 nm, when both the semiconductors are photoactivated. On the contrary, at λ=400 nm, when the photoactivity of WO_x is predominant compared to that of TiO_2, the main charge transfer mechanism could be activated by the shift of the quasi-Fermi level. Due to the irradiation, a non-equilibrium state could be originated by the “hot” electrons injected into the WO_x CB, so that the quasi-Fermi level of WO_x could become higher than that of TiO_2 (Fermi level of TiO_2 remained about constant, due to its scarce photoactivity at 400 nm).

4.5 Combined systems: $Ti/TiO_2WO_3/WO_3$ electrodes

This section studies the influence of the presence of WO_3 in the nanotubular structure on the photoactivity of different TiO_2-WO_3 systems. As explained in section 4.4.7, due to the disposition of the semiconductors at the $Ti/TiO_2/WO_x$ electrodes (NT-4/Wy samples), transfer of electrons photogenerated at the tungsten oxide phase to the external circuit occur only trough the titania phase (see the schemes for the proposed charge transfer mechanisms depicted in *Figure 4.29*): a direct electron transfer from the WO_x to the titanium conductive layer is forbidden. On the other hand, although a benefit was observed at low WO_x coverage levels (see *Figure 4.30* in section 4.4.7), it is also to be considered that a direct contact between the WO_x and the Ti conductive layer and a specific disposition of the semiconductors respect to the Ti layer may favour the separation and transfer of the photogenerated charges at the TiO_2-WO_3 system. In such a situation, an enhancement of the photoelectrochemical performance of the combined system may be achieved (if compared to that of the $Ti/TiO_2/WO_3$ configuration).

On the basis of these assumptions, an attempt is made in order to prepare TiO_2-WO_3 systems in which the tungsten oxide phase will be in direct contact with the Ti conductive layer. In particular, mixed TiO_2WO_3 nanotubes are synthesized by one-step anodization of Ti to obtain Ti/TiO_2WO_3 electrodes: different amounts of sodium tungstate were added to the anodization solution, in order to incorporate the tungsten oxide in the nanotubular matrix during the formation of the nanotubes. In some cases, the nanotubular structures were also used as support under-layers for the preparation of $Ti/TiO_2WO_3/WO_3$ electrodes. The over-layer of WO_3 was deposited on the nanotubular structures via cathodic electrodeposition, by using the PPT explained in section 3.1.1.3.

The effect of the concentration of sodium tungstate in the oxidation bath on the morphology and the photoactivity of the support under-layer was study; the PEC behaviour of the samples after the cathodic electrodeposition of WO_3 was also investigated. The performances of the samples in neutral supporting electrolyte are compared when samples are irradiated with light at two different wavelengths: 365 nm and 400 nm.

4.5.1 Preparation of the TiO_2WO_3 Nanotubes: Ti/TiO_2WO_3 electrodes

The TiO_2WO_3 nanotubular structures were prepared by one-step electrochemical oxidation of Ti foil (disk of 15 cm^2 of nominal area), as previously explained in section 4.3.2, in a mixture electrolyte containing different concentration of $Na_2WO_4 \cdot 2H_2O$ (0.6mM, 12mM and 25mM). As comparison, also TiO_2 single phase nanotubes were growth following the same procedure but in absence of sodium tungstate in the anodization bath. The same anodization conditions (20V, 4h at room temperature) were employed for the synthesis of all the nanotubular structures. *Table 4.6* summarizes the composition of the electrolytes used for the synthesis of the samples. The samples are indicated in the rest of the test as "X-J", where "X" indicates the composition of the nanotubular structure and "J" indicates the concentration of the sodium tungstate in the anodization bath, in mM.

Table 4.6. *Composition of the anodization solution for the preparation of the X-J samples; T: TiO_2 and TW:TiO_2WO_3.*

Sample	Composition of the Electrolyte
T	90%Glycerol / 10%H_20 / 0.14M NH_4F
TW-0.6	90%Glycerol / 10%H_20 / 0.14M NH_4F / 0.6mM $Na_2WO_4 \cdot 2H_2O$
TW-12	90%Glycerol / 10%H_20 / 0.14M NH_4F / 12mM $Na_2WO_4 \cdot 2H_2O$
TW-25	90%Glycerol / 10%H_20 / 0.14M NH_4F / 25mM $Na_2WO_4 \cdot 2H_2O$

A final annealing treatment was performed in air atmosphere at 400 °C for 1 h. The resulting structures were used either as final electrodes or as basic supports for the deposition of tungsten oxide.

4.5.2 Electrochemical deposition of WO_3 to obtain the Ti/TiO_2WO_3/WO_3 electrodes

The electrodeposition of WO_3 was performed following the procedure explained in section 3.1.1.3. In the specific, the electrochemical deposition

was carried out at room temperature in a classical three-electrode cell in which the TW-12 sample was used as working electrode (nominal area 2 cm^2) while a Pt grid and a SCE were the counter and reference electrodes, respectively.

The PPT was used in order to obtain the WO_3 over-layer on the TW-12 support. As explained in detail in section 3.1.1.3, during PPT, the potential was alternated swiftly between open circuit potential (OCP) and -0.3 V. A series of pulses of equal amplitude but different widths was performed. On the basis of the previous results (see section 4.4.10), low electrodeposition times (5 s and 10 s) were adopted, so that 5 or 10 pulses were required to reach the proposed deposition times. The obtained WO_3 modified samples were annealed in air atmosphere at 450 °C for 2 h.

Final samples on which deposits of tungsten oxide were obtained will be indicated as TW-12/W_y, where "y" indicates the deposition time of the tungsten oxide, in seconds.

4.5.3 Characterization of the TiO_2 and TiO_2WO_3 Nanostructures

This section reports the results derived from the characterization of the Ti/TiO_2 and Ti/TiO_2WO_3 nanostructured electrodes. The crystalline phase, optical properties, morphology, and photoactivity of the synthesized structures were characterized by Raman, UV-vis diffuse reflectance spectra, SEM and chronoamperometric analysis respectively.

4.5.3.1 Raman Measurements: analysis of the TiO_2 and WO_3 phases

The presence of WO_3 in the synthesized nanostructures was assessed by the Raman measurement performed at the TW-J electrodes. As an example, *Figure 4.35* reports the Raman spectra of TW-12 support; data related to the bare NT-4/W_{10} support is also reported in the graph as a comparison.

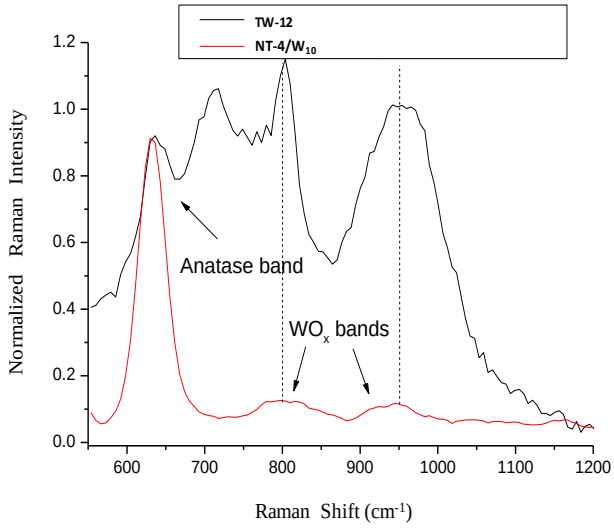

Figure 4.35. *Raman spectra of TW-12 (black line) and NT-4/W_{300} (red line). The peaks from TiO_2 anatase phase and the peaks related toWO_x phases are indicated with narrows.*

If the TW-12 electrode is considered, data confirms that anatase is the prevailing phase of the TiO_2 semiconductor material, while different phases of the tungsten oxide are presented in the sample. The spectrum registered on the electrode reveals the Raman feature of the anatase phase: 639 (Eg)* cm^{-1} [151]. As the tungsten oxide is considered, two peaks appear at about 800 and 950 cm^{-1}, due to the overlapping of the contributions from the different phases of tungsten oxide (bending and stretching vibration of the O–W–O modes). In particular, the peak at 800 cm^{-1} may be related to the WO_3 ϒ-phase (monoclinic, space group P21/n) and the β-phase (orthorhombic space group Pnma) are the most probable [152]. As explained in section 4.4.4, the presence of both phases is an expected result because the WO_3 ϒ to β-phase transition temperature (350°C) is very close to the annealing temperature utilized (450 °C) [153,154]. The broad peak at about 950 cm^{-1} is not related to any phase of the WO crystal, but to the overlapping of defect modes related to the presence of other oxides in which tungsten has a higher coordination level (such as WO_5 or even WO_6) [155,156]. For this reason, the tungsten oxide phase will be also indicated in this case as WO_x.

The obtained results, confirms the formation of structures composed of a mix of titania and tungsten oxides (Ti/TiO_2WO_x electrodes): somehow the tungsten oxide was incorporated to the TiO_2 matrix during the titanium foil anodization process and the subsequence annealing treatment [166].

No specific analysis about the homogeneity of the tungsten oxide particles inside the nanotubular matrix was performed. Maybe, during the growth of the nanotubular structures (anodization process: 4 h at 20 V), an undesired nucleation of tungsten oxide could generate a non-homogeneous distribution of the tungsten oxide in the nanostructures. However, the aim of this Thesis was the incorporation of tungsten oxide inside the nanotubular structures (or the formed oxide) by one-step anodization of Ti. This fact, was demonstrated by the Raman spectra of the TW-12 sample (TiO_2-WO_3 system) reported in Figure 4.35.

4.5.3.2 Diffusive reflectance UV-vis spectra

This section studies the optical properties such as band gap energy of the TiO_2 and TiO_2WO_x synthesized structures. *Figure 4.36* reports the trend of the Kubelka–Munk function with photon energy, $(F(R)\,h\nu)^{1/2}$ vs. $h\nu$, recorded at the T, TW-0.6 and TW-12 samples. As it can be observed, the increasing of the concentration of sodium tungstate causes a progressively narrowing in the measured band gap. This behavior can be attributed to the different amount of WO_x in the resulting mixed oxide layer: a decrease of the band gap from about 3.2 to 3.15 eV was observed, when the nanostructures were prepared in an anodization solution containing 12 mM of sodium tungstate.

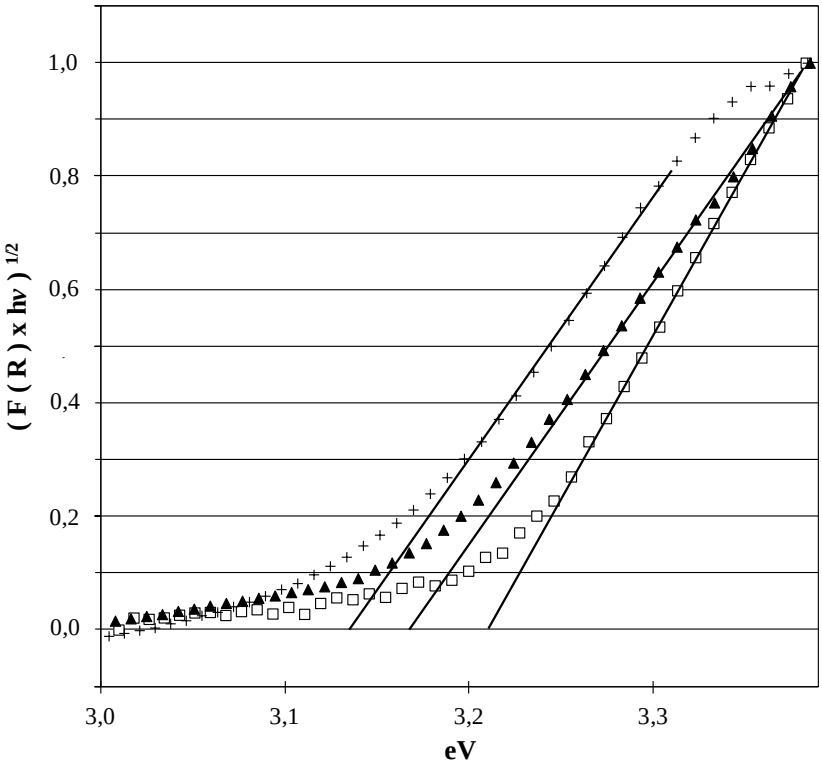

Figure 4.36. *Normalized Absorbance curves (F(R) * hv)$^{1/2}$ vs hv (eV) , from thr right to the left, for the T (a), TW-0.6 (b) and (c) TW-12 electrodes.*

The results indicate that the presence of WO_x in the structures decreases the band gap of the conventional TiO_2 nanotubes. However, as explained in section 4.4.5, to improve the photocatalytic efficiency of the material, low recombination rates between the photogenerated charges and good charge transport capability are also required [157]; so that the morphology of the synthesized structures, which were used as supports for the subsequent tungsten oxide deposition, will be study in the next section.

4.5.3.3 Morphological characterization of the TiO_2 and TiO_2WO_x nanostructures

Figure 4.37 represents the morphology of the structures obtained after the electrochemical anodization of the Ti foil in different electrolytic baths.

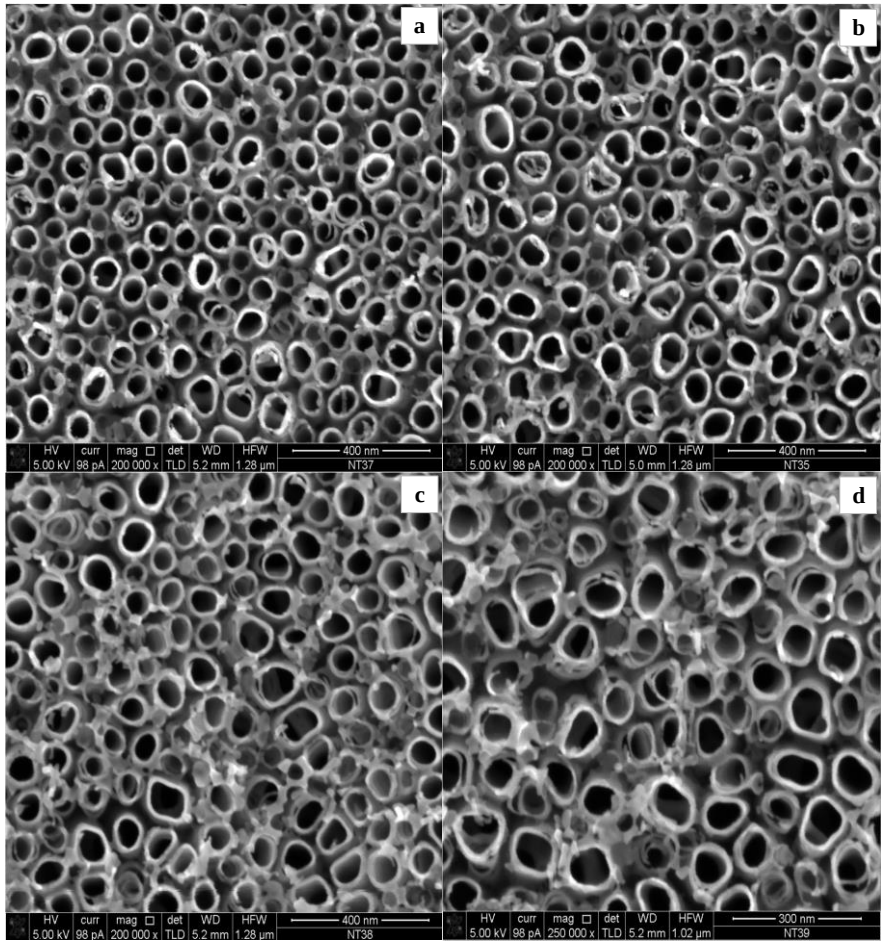

Figure 4.37. *SEM micrographs of the T (a), TW-0.6 (b), TW-12 (c) and (d) TW-25 electrodes.*

The top view of the unmodified samples clearly shows the formation of nanotubes with different dimensions (mean diameter ranging from 70 to 90 nm) depending on the sodium tungstate concentration used in the anodization electrolyte.

As expected, highly ordered TiO_2 nanotubes with a pore diameter around 70 nm were formed in the absence of sodium tungstate (*Figure 4.37a*). On the other hand, considering TiO_2WO_x nanotubular composite electrodes prepared by one-step electrochemical anodization in organic solutions, literature reports the losing of the nanotubular structure and the formation of compact TiO_2WO_3 films when the sodium tungstate concentration in anodization solution is equal or higher than 1.8 mM [167]. However, in the present work, the nanotubular structure still evidence also when higher concentrations of sodium tungstate are used during the anodization process. Besides, less regular nanotubular morphology is observed when the sodium tungstate concentration in the anodization solution increased from 0.6 mM to 25 mM: higher diameters of the pores and also a decrease in the definition of the circular shape of the pore were observed at higher sodium tungstate concentration values.

Nevertheless, the method employed for the synthesis of the TW-J underlayers leads to the formation of TiO_2WO_x nanotubar structures, which have demonstrated to offer large surface areas with a smooth electron transport, thereby, minimizing the recombination between the photogenerated charges (see section 4.1).

4.5.3.4 Photoactivity of the samples: TiO_2 and TiO_2WO_x nanotubes

As the photoactivity of the nanotubular structures is concerned, *Figure 4.38* shows the normalized photocurrent values (NPC) derived from the chronoamperometric test performed at the T, TW-0.6, TW-12 and TW-25 electrodes, at 0.8 V of overpotential from the OCP of each electrode; it was verified that such bias potential was enough to saturate the photocurrent.

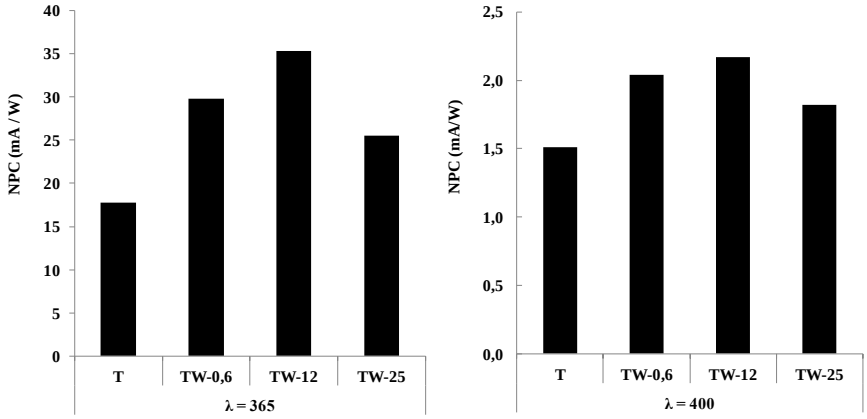

Figure 4.38. *NPC (mA/W) for the T, TW-0.6, TW-12 and TW-25 electrodes. Data obtained at 365 nm and 400 nm in 0.1M KNO_3.*

The obtained data reported in *Figure 4.38*, confirms that samples are photoactive at the two investigated wavelengths, and also that the photocurrents measured at the TiO_2WO_x nanotubular structures are always higher than those measured at the TiO_2 single phase electrodes. If compared to the TiO_2 based structures, the increase of the NCP values obtained at 400 nm (photocativity of TiO_2 remained about constant, due to its scarce photoactivity at 400 nm) may be attribuited to the presence of a new active phase (WO_x) in the nanotubular structures.

Moreover, similar trends of photocurrents were observed at the two wavelengths, confirming that in both the cases, an optimum in the photoactivity was reached, at which a specific concentration of sodium tungstate was convenient. In particular, the electrode prepared with a concentration of 12 mM $Na_2WO_4 \cdot 2H_2O$ resulted the best performing at both the wavelengths, suggesting that an appropriate concentration of sodium tungstate may be important for the development of TiO_2WO_x nanotubular layers with appropriated photoelectrochemical properties. The effects of the presence of WO_x in the nanotubular structures on the transfer of the photogenerated charges at the TiO_2-WO_3 systems will be study more in detail in section 4.6.

On the basis of the obtained results, a new batch of electrodes was prepared in order to investigate on the PEC performance of $Ti/TiO_2WO_x/WO_x$ systems, when tungsten oxide is present in the nanotubes: the best performing electrode, TW-12, was selected as under-layer support for the electrochemical deposition of the tungsten oxide over layer.

4.5.4 Tungsten oxide modified TiO_2WO_x nanotubes: $Ti/TiO_2WO_x/WO_x$ electrodes

The PPT was adopted to deposit tungsten oxide on the TiO_2WO_x nanotubular composite sample. To this aim, different samples (2 cm^2) derived from the TW-12 electrode (15 cm^2) were used, at which different tungsten oxide loading times were applied. As explained before (see section 4.5.2), 5 s and 10 s were selected as deposition times in order to obtain the WO_x modified samples and maintain at the same time the original nanotubular structure of the TW-12 sample.

This section reports the results derived from the characterization of the WO_x modified TW-12 electrodes (TW-12/W_5 and TW-12/W_{10}). The morphology and photoactivity of the synthesized structures were characterized by means of SEM and chronoamperometric tests.

4.5.4.1 Morphological characterization

Figure 4.39 shows the morphologies of the TiO_2WO_x nanotubular layers (TW-12 sample) after the electrochemical deposition of WO_x. The SEM micrograhps reveal that tungsten oxide deposits may occur at the walls of the nanotubular structures, obtaining WO_x nanoparticles dispersed on the outside and inner parts of the nanotubes.

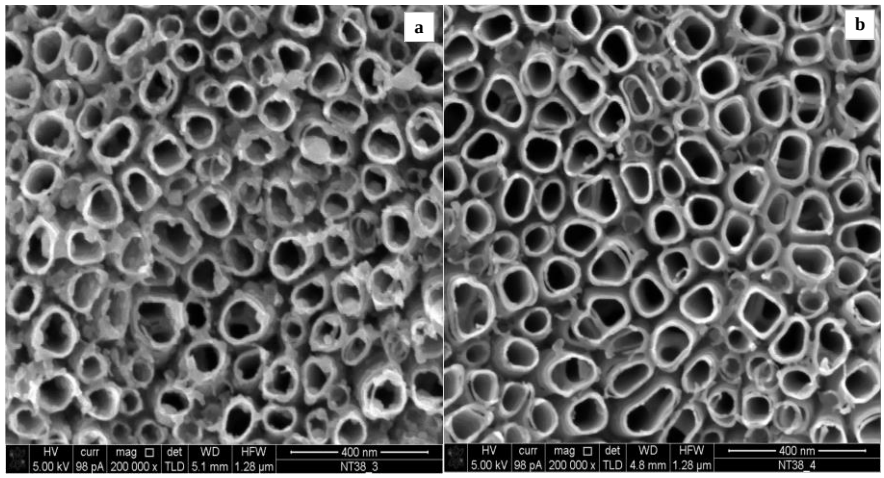

Figure 4.39. *SEM micrographs of the TW-12/W_5 (a) and TW-12/W_{10} (b).*

Moreover, the extent of the interface electrode/electrolyte seems to not be significantly affected after to deposit WO_x: no plugging of the nanotubular structures is observed at this deposition times. It is possible to observe that the nanotubular structures are still characterized by an open top pore, without losing their architecture after the deposition of WO_x. This fact is essential to obtain electrodes with good photocatalytic activity: previous results (section 4.4.7) demonstrated that the real benefit of combining WO_x with highly ordered nanotubes can be achieved only if a partial coverage by WO_x is obtained, at which the prevailing effects are the decrease of charge recombination at the TiO_2-WO_3 system and the maintenance of an appropriate extent of the interface electrode/electrolyte.

4.5.4.2 Photoactivity of the WO_x modified sample

Table 4.7 summarizes the normalized photocurrents, measured at different wavelengths, for the bare TW-12 support and the WO_x modified samples (TW-12/W_5 and TW-12/W_{10}).

Table 4.7. *NPC values (mA/W) for the bare (TW-12) and modified supports (TW-12/W_5 and TW-12/W_{10}) obtained at 365 and 400 nm in 0.1 M KNO_3.*

Sample	TW-12	TW-12/W_5	TW-12/W_{10}
NPC_{365} (mA / W)	35,35	28,53	27,94
NPC_{400} (mA / W)	2,17	5,09	6,99

If the data obtained at 365 nm are considered, when compared with the bare TW-12 support, a decrease of the photoactivity of the WO_x modified electrodes is observed. The obtained results seem to be in contrast with the behavior reported for the tungsten oxide modified NT-4 under-layer ($Ti/TiO_2/WO_x$ electrodes): at low WO_x coverage levels (2, 5 and 10 seconds), increasing trend of the photocurrents was observed at 365 nm (see section 4.4.7) in KNO_3. However, in this case, the composition and disposition of the semiconductors in the under-layer (Ti/TiO_2WO_x) is different. Therefore, even at low WO_x deposition times, the effect of the second oxide over-layer on the photoactivity of the combined system may differ from the expected trend. The TiO_2 phase at the surface of the TW-12 electrode may is partially covered by a less active material (WO_x): as reported in section 4.4.8, charge recombination at WO_x is higher than at TiO_2. This fact may be the reason of the NPC_{365} trend reported in *Table 4.7*.

On the other hand, at 400 nm, the addition of small amounts of tungsten oxide resulted to be always convenient: as expected (see section 4.4.8), an enhancement of the NPC_{400} values is observed when passing from 5 to 10 s of WO_x deposition time. As reported in *Table 4.7*, a 3-fold increase of the NPC value is observed after 10 seconds of deposition. However, although the adition of WO_x involves a benefit in terms of photocurrent, it not has to be related with a decrease of the charge recombination at the TW-12/W_y samples (see section 4.4.8).

4.5.5 Conclusions

The results reported in this section demonstrated the formation of both TiO_2 and TiO_2WO_x nanotubes by using a one-step anodization process. The morphology and the photoactivity of the bare TiO_2WO_x nanotubes seem to be influenced by the concentration of sodium tungstate in the anodization solution. 12 mM resulted to be the optimum concentration of sodium tungstate, to be used in the anodization solution, in order to obtain nanotubular structures with good photoactivity under the investigated wavelengths of light. Compared to the bare TW-12, the WO_x modified electrodes exhibited enhanced photocatalytic activity only at 400 nm.

Moreover, it must be considered that the experiments reported up to now are only performed at two specific wavelengths of the solar spectrum, so further investigation on the PEC performance of the best performing electrodes, when the samples were illuminated by a wider range of the incident light, was further undertaken in the next section.

4.6 Photoelectroactivity of the best performing electrodes under UV-vis simultaneous irradiation

The optical, electrochemical and photoelectrochemical characterization of the synthesized electrodes have allowed individuating the best performing electrodes for PEC applications. Considering the bare nanotubular structures and their anodization conditions, NT-4 and TW-12 showed the best activity under the investigated wavelengths (365 nm and 400 nm). On the other hand, after the electrochemical deposition of WO_x on the nanotubular surface, NT-4/W_{10} and TW-12/W_{10} have demonstrated also good performance. *Table 4.8* summarizes the composition and disposition of the semiconductor materials in the best performing electrodes.

Table 4.8. *Best performing samples: composition and the disposition of the semiconductor materials.*

Sample	**Composition and disposition of the semiconductors**
NT-4	Ti/TiO_2
NT-4/W$_{10}$	$Ti/TiO_2/WO_x$
TW-12	Ti/TiO_2WO_x
TW-12/W$_{10}$	$Ti/TiO_2WO_x/WO_x$

This section reports the PEC performance of the electrodes reported in *Table 4.8*, when they were used as photoanodes and were irradiated simultaneously by UV-vis light. In particular, photocurrent measurements were performed using a 300W xenon lamp equipped with air mass (AM) 0 and 1.5 D filters, which were used to simulate the solar irradiation. The transmittance spectrum for the filter set is plotted in *Figure 4.40*.

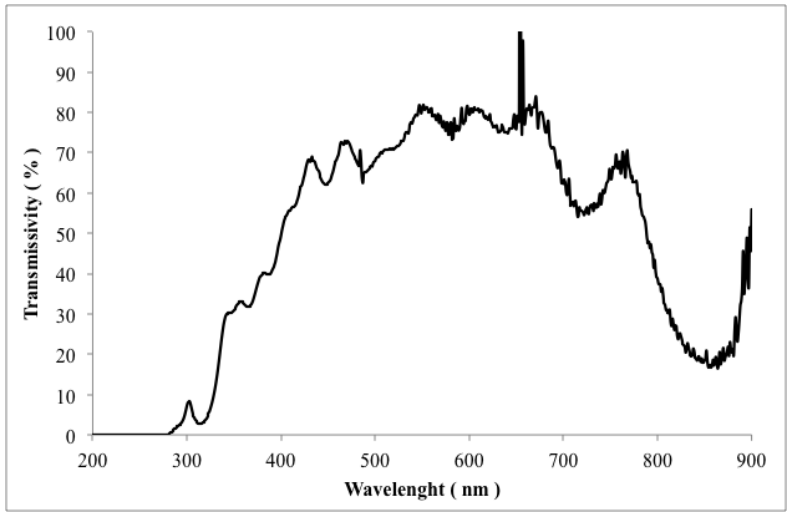

Figure 4.40. *Transmittance spectrum for the AM (0) and (1.5D) filter set.*

In particular, the disposition of the WO_x phase in the combined structures was considered in order to explain the differences of the PEC performances of the investigated electrodes.

4.6.1 Photoactivity of the best performing electrodes

Figure 4.41 reports the photocurrent densities as a function of potential of the NT-4, NT-4/W_{10}, TW-12 and TW-12/W_{10} electrodes, when they were exposed to radiation from a 300 W Xenon lamp equipped with AM (0) and (1.5D) filters.

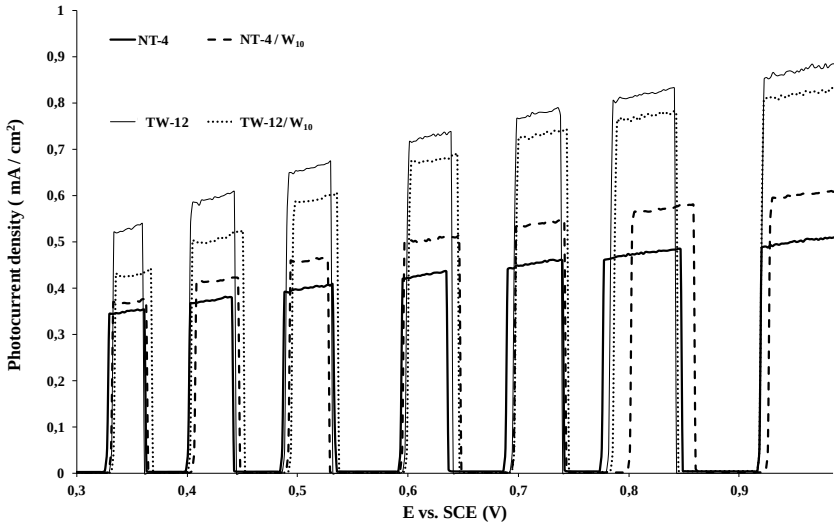

Figure 4.41. *Photocurrent density (mA/cm^2) for the best performing samples: NT-4, NT-4/W_{10}, TW-12 and TW-12/W_{10}. Data obtained when the samples were simultaneously irradiated with UV-vis light, in 0.1M KNO_3.*

In all the cases, the dark current can be negligible; thus, measured current under illumination could be refereed as a pure photocurrent. Moreover, it is worth to be noting that the enhancement of the generated photocurrent is positively influenced by the presence of WO_x, either when this oxide is incorporated into the nanotubes or is electrochemical deposited onto the nanotubular surface: the NT-4 electrode sample shows the worst PEC performance. As explained in previous sections, the observed behaviour can be attributed to a decrease of the recombination rate and charge transfer resistance but also to an enhanced light absorption in the visible range of the TiO_2-WO_x systems, if compared to bare TiO_2.

Among all the analysed electrodes, the TW-12 was the best performing sample in the wide potential range under simultaneous use of UV and visible light. The improved PEC properties could be atributed to the incorporation of WO_x into the nanotubular matrix, which leads to bandgap narrowing (see section 4.5.3.2), photogenerated charge transfer improvement, and limitation of the charge recombination processes in the TiO_2-WO_x system.

Taking into account the disposition of the semiconductors at the TW-12 electrode, the energy of the incident light (both the semiconductors are photoactivated) and the anodic potential to which the sample is submitted, the observed behavior can be explained as follows.

If a direct contact of WO_X with the Ti surface (to which the anodic potential is applied) was generated during the synthesis of the nanotubes, the photogenerated charge transfer mechanism may be determined by the reciprocal position of the energy levels of the band edges of the semiconductors; transfer of electrons accumulated in the CB of WO_x, towards the counter electrode, and the capture of holes in the VB of the TiO_2 by electron donors in solution can occur at the combined structure (see scheme in figure *Figure 4.42*).

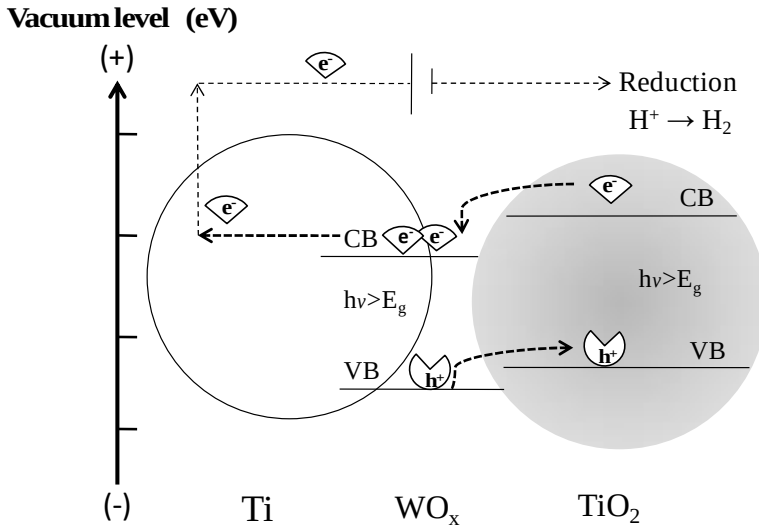

Figure 4.42. *Scheme of the proposed charge transfer mechanisms at the TW-12 electrode.*

However, if a different disposition of WO_x is additionally obtained in the TW-12 structure (e.g., WO_x covering the TiO_2 phase or WO_x phase is not in direct contact with the Ti substrate ($Ti/TiO_2/WO_3$ disposition)) a more complex situation has to be considered to describe the charge transfer process occurring at the TW-12 electrode. In these situations, the flow of the photogenerated charges can be activated also by the two proosed mechanisms reported in section 4.4.7 (Z-scheme or shift of the quai-Fermi level).

4.6.2 Conclusions

In summary, among all the investigated configurations of the TiO_2-WO_x systems, the suitable disposition of the semiconductors at the TW-12 seems to offer an effective combination of the oxides in order to guarantee good performances under solar light irradiation; i.e. the presence of WO_x in the nanotubular structures may provides an efficient path for the transport of the electrons from the CB of the tungsten oxide phase to the external circuit, allowing holes at WO_x VB available for the electrolyte.

Chapter 5 Final Conclusions

This Thesis has reported the study of the PEC behavior of different TiO_2-WO_3 combined structures during the photoelectrosplitting of water. The presented results gave evidence on the effectiveness of combining tungsten oxide with well-ordered TiO_2 nanotubes.

Taking into account both the energy of the incident light and the disposition of the semiconductors in the TiO_2-WO_x system, the transfer of the photogenerated electrons towards the counter electrode and the flow of hole to the semiconductor/electrolyte interface can be determided by different mechanisms.

On the one hand, when the Ti/TiO_2/WO_3 configuration is considered, the Z-scheme may be activated thanks to the conductive nature of the nanotubular surface. It may constitute a suitable interlayer which activates a charge transfer mechanism, allowing electrons at TiO_2 CB and holes at WO_x VB, to be transported to the counter electrode, or available for the electrolyte, respectively. Such a mechanism may be the most favored when both the semiconductors are photoactivated. On the other hand, when the photoactivity of WO_x is predominant compared to that of TiO_2, the main charge transfer mechanism could be activated by the shift of the quasi-Fermi level: due to the irradiation, a non-equilibrium state could be originated by the "hot" electrons injected into the WO_x CB, so that the quasi-Fermi level of WO_x could become higher than that of TiO_2 (Fermi level of TiO_2 remained about constant, due to its scarce photoactivity at 400 nm). In such a situation transfer of electron from the WO_x CB to the TiO_2 CB may occur.

Moreover, with the Ti/TiO_2WO_3 configuration, if a direct contact of WO_X with the Ti substrate (to which the anodic potential is applied) was generated during the synthesis of the mixed oxide nanotubes, the photogenerated charge transfer mechanism may be determined also by the reciprocal position of the energy levels of the band edges of the semiconductors; a direct transfer of electrons accumulated in the CB of WO_x, towards the counter electrode, and the capture of holes in the VB of the TiO_2 by electron donors in solution can occur at the combined structure.

In all the proposed configurations, at TiO_2 not covered by WO_x, the charge transfer can occur by the mechanism expected at n-type semiconductors, by which free holes at the VB can react with the electrolyte, provided it is able to contact the electrode interface (in the case of the $Ti/TiO_2/WO_3$ or $Ti/TiO_2WO_3/WO_3$ configurations at low WO_x coverage degrees).

Among all the investigated configurations of the TiO_2-WO_x systems, the suitable disposition of the semiconductors at the TW-12 electrode seems to offer an effective combination of the oxides in order to guarantee good performances under solar light irradiation. The presence of WO_x in the nanotubular structures may provides an efficient path for the transport of the electrons from the CB of the tungsten oxide phase to the external circuit.

References

[1] BP, BP Statistical Review of World Energy - Full report, (2016) 1–48.

[2] L.M. Peter, K.G. Upul Wijayantha, Photoelectrochemical water splitting at semiconductor electrodes: Fundamental problems and new perspectives, ChemPhysChem. 15 (2014) 1983–1995. doi:10.1002/cphc.201402024.

[3] M. Momirlan, T.N. Veziroglu, Current status of hydrogen energy, 6 (2002) 141–179.

[4] J. Juodkazyte, G. Seniutinas, B. Šebeka, I. Savickaja, T. Malinauskas, K. Badokas, K. Juodkazis, S. Juodkazis, Solar water splitting: Efficiency discussion, Int. J. Hydrogen Energy. (2016) 1–14. doi:10.1016/j.ijhydene.2016.05.079.

[5] K. Sivula, F. Le Formal, M. Grätzel, Solar Water Splitting: Progress Using Hematite (α-Fe_2O_3) Photoelectrodes, ChemSusChem. 4 (2011) 432–449. doi:10.1002/cssc.201000416.

[6] J.A. Turner, A Nickel Finish Protects Silicon Photoanodes for Water Splitting, Science (80). 342 (2013) 811–812. doi:10.1126/science.1246766.

[7] C.G. Morales-Guio, S.D. Tilley, H. Vrubel, M. Grätzel, X. Hu, Hydrogen evolution from a copper (I) oxide photocathode coated with an amorphous molybdenum sulphide catalyst, Nat. Commun. 5 (2014). doi:10.1038/ncomms4059.

[8] M.G. Walter, E.L. Warren, J.R. McKone, S.W. Boettcher, Q. Mi, E.A. Santori, N.S. Lewis, Solar Water Splitting Cells., Chem. Rev. (Washington, DC, United States). 110 (2010) 6446–6473. doi:10.1021/cr1002326.

[9] K. Fujishima, A. and Honda, A. Fujishima, K. Honda, Electrochemical Photolysis of Water at Semiconductor Electrode, Nature. 238 (1972) 37.

[10] T. Bak, J. Nowotny, M. Rekas, C.. Sorrell, Photo-electrochemical hydrogen generation from water using solar energy. Materials-

related aspects, Int. J. Hydrogen Energy. 27 (2002) 991–1022. doi:10.1016/S0360-3199(02)00022-8.

[11] M.S. Prévot, K. Sivula, Photoelectrochemical Tandem Cells for Solar Water Splitting, J. Phys. Chem. C. 117 (2013) 17879–17893. doi:10.1021/jp405291g.

[12] C. Ding, W. Qin, N. Wang, G. Liu, Z. Wang, P. Yan, J. Shi, C. Li, Solar-to-hydrogen efficiency exceeding 2.5% achieved for overall water splitting with an all earth-abundant dual-photoelectrode, Phys. Chem. Chem. Phys. 16 (2014) 15608. doi:10.1039/c4cp02391a.

[13] Gurudayal, D. Sabba, M.H. Kumar, L.H. Wong, J. Barber, M. Grätzel, N. Mathews, Perovskite–Hematite Tandem Cells for Efficient Overall Solar Driven Water Splitting, Nano Lett. 15 (2015) 3833–3839. doi:10.1021/acs.nanolett.5b00616.

[14] Z. Zhang, R. Dua, L. Zhang, H. Zhu, H. Zhang, P. Wang, Carbon-Layer-Protected Cuprous Oxide Nanowire Arrays for Efficient Water Reduction, ACS Nano. 7 (2013) 1709–1717. doi:10.1021/nn3057092.

[15] N. KELLY, T. GIBSON, Design and characterization of a robust photoelectrochemical device to generate hydrogen using solar water splitting, Int. J. Hydrogen Energy. 31 (2006) 1658–1673. doi:10.1016/j.ijhydene.2005.12.014.

[16] Y.W. Chen, J.D. Prange, S. Dühnen, Y. Park, M. Gunji, C.E.D. Chidsey, P.C. McIntyre, Atomic layer-deposited tunnel oxide stabilizes silicon photoanodes for water oxidation, Nat. Mater. 10 (2011) 539–544. doi:10.1038/nmat3047.

[17] T. Wang, Z. Luo, C. Li, J. Gong, Controllable fabrication of nanostructured materials for photoelectrochemical water splitting via atomic layer deposition, Chem. Soc. Rev. 43 (2014) 7469–7484. doi:10.1039/C3CS60370A.

[18] Y. Lin, Y. Xu, M.T. Mayer, Z.I. Simpson, G. McMahon, S. Zhou, D. Wang, Growth of p-Type Hematite by Atomic Layer Deposition and Its Utilization for Improved Solar Water Splitting, J. Am. Chem. Soc. 134 (2012) 5508–5511. doi:10.1021/ja300319g.

[19] M.T. Mayer, Y. Lin, G. Yuan, D. Wang, Forming Heterojunctions at the Nanoscale for Improved Photoelectrochemical Water

Splitting by Semiconductor Materials: Case Studies on Hematite, Acc. Chem. Res. 46 (2013) 1558–1566. doi:10.1021/ar300302z.

[20] S.J.A. Moniz, S.A. Shevlin, D.J. Martin, Z.-X. Guo, J. Tang, Visible-light driven heterojunction photocatalysts for water splitting – a critical review, Energy Environ. Sci. 8 (2015) 731–759. doi:10.1039/C4EE03271C.

[21] S. Choudhary, S. Upadhyay, P. Kumar, N. Singh, V.R. Satsangi, R. Shrivastav, S. Dass, Nanostructured bilayered thin films in photoelectrochemical water splitting – A review, Int. J. Hydrogen Energy. 37 (2012) 18713–18730. doi:10.1016/j.ijhydene.2012.10.028.

[22] S.Y. Reece, J.A. Hamel, K. Sung, T.D. Jarvi, A.J. Esswein, J.J.H. Pijpers, D.G. Nocera, Wireless Solar Water Splitting Using Silicon-Based Semiconductors and Earth-Abundant Catalysts, Science (80). 334 (2011) 645–648. doi:10.1126/science.1209816.

[23] M.J. Kenney, M. Gong, Y. Li, J.Z. Wu, J. Feng, M. Lanza, H. Dai, High-Performance Silicon Photoanodes Passivated with Ultrathin Nickel Films for Water Oxidation, Science (80). 342 (2013) 836–840. doi:10.1126/science.1241327.

[24] J.J.H. Pijpers, M.T. Winkler, Y. Surendranath, T. Buonassisi, D.G. Nocera, Light-induced water oxidation at silicon electrodes functionalized with a cobalt oxygen-evolving catalyst, Proc. Natl. Acad. Sci. 108 (2011) 10056–10061. doi:10.1073/pnas.1106545108.

[25] Z. Li, W. Luo, M. Zhang, J. Feng, Z. Zou, Photoelectrochemical cells for solar hydrogen production: current state of promising photoelectrodes, methods to improve their properties, and outlook, Energy Environ. Sci. 6 (2013) 347–370. doi:10.1039/C2EE22618A.

[26] R.T. Yang, Fundamentals and applications, 2001. doi:10.1038/nprot.2009.120.Multi-stage.

[27] A.W. Bott, D. Ph, Electrochemistry of Semiconductors, 1964. doi:10.1016/0038-092X(64)90079-9.

[28] C. Characteristics, Chapter 2 Electrode / Electrol Yte Interfaces : Structure and, 1900.

[29] J. Rodriguez Ruiz, Nanostructured TiO_2-based materials for photoelectrochemical applications, n.d.

[30] A.J. Bard, Photoelectrochemistry and heterogeneous photo-catalysis at semiconductors, J. Photochem. 10 (1979) 59–75. doi:10.1016/0047-2670(79)80037-4.

[31] A.J. Nozik, R. Memming, Physical Chemistry of Semiconductor−Liquid Interfaces, J. Phys. Chem. 100 (1996) 13061–13078. doi:10.1021/jp953720e.

[32] M.X. Tan, P.E. Laibinis, S.T. Nguyen, J.M. Kesselman, C.E. Stanton, N.S. Lewis, Principles and Applications of Semiconductor Photoelectrochemistry, pp. 21–144. doi:10.1002/9780470166420.ch2.

[33] S. Krishna Haram, Handbook of electrochemistry.

[34] H.-P. Boehm, The Chemical Physics of Surfaces. VonS. R. Morrison. Plenum Press, New York—London 1977., Angew. Chemie. 90 (1978) 500–501. doi:10.1002/ange.19780900640.

[35] W. Simons, A. Hubin, J. Vereecken, The role of electrochemical impedance spectroscopy (EIS) in the global characterisation of the reduction kinetics of hexacyanoferrate on anodised titanium, Electrochim. Acta. 44 (1999) 4373–4381. doi:10.1016/S0013-4686(99)00153-X.

[36] F. Di Quarto, A.J. Bard, Semiconductor electrodes, J. Electroanal. Chem. Interfacial Electrochem. 127 (1981) 43–58. doi:10.1016/S0022-0728(81)80466-4.

[37] S. Chen, Gold Nanoelectrodes of Varied Size: Transition to Molecule-Like Charging, Science (80). 280 (1998) 2098–2101. doi:10.1126/science.280.5372.2098.

[38] O.K. Varghese, C.A. Grimes, Appropriate strategies for determining the photoconversion efficiency of water photoelectrolysis cells: A review with examples using titania nanotube array photoanodes, Sol. Energy Mater. Sol. Cells. 92 (2008) 374–384. doi:10.1016/j.solmat.2007.11.006.

[39] A. Wahl, M. Ulmann, A. Carroy, J. Augustynski, Highly selective photo-oxidation reactions at nanocrystalline TiO_2 film electrodes, J.

Chem. Soc. Chem. Commun. (1994) 2277. doi:10.1039/c39940002277.

[40] J.J. Kelly, D. Vanmaekelbergh, Charge carrier dynamics in nanoporous photoelectrodes, Electrochim. Acta. 43 (1998) 2773–2780. doi:10.1016/S0013-4686(98)00018-8.

[41] A. Hagfeldt, B. Didriksson, T. Palmqvist, H. Lindström, S. Södergren, H. Rensmo, S.-E. Lindquist, Verification of high efficiencies for the Grätzel-cell. A 7% efficient solar cell based on dye-sensitized colloidal TiO2 films, Sol. Energy Mater. Sol. Cells. 31 (1994) 481–488. doi:10.1016/0927-0248(94)90190-2.

[42] R. Vogel, P. Hoyer, H. Weller, Quantum-Sized PbS, CdS, Ag_2S, Sb_2S_3, and Bi_2S_3 Particles as Sensitizers for Various Nanoporous Wide-Bandgap Semiconductors, J. Phys. Chem. 98 (1994) 3183–3188. doi:10.1021/j100063a022.

[43] J. NOWOTNY, T. BAK, M. NOWOTNY, L. SHEPPARD, Titanium dioxide for solar-hydrogen I. Functional properties, Int. J. Hydrogen Energy. 32 (2007) 2609–2629. doi:10.1016/j.ijhydene.2006.09.004.

[44] M. Baraton, Nano-TiO_2 for Solar Cells and Photocatalytic Water Splitting : Scientific and Technological Challenges for Commercialization, (2011) 64–77. doi:10.2174/1874140101105010064.

[45] X. Chen, S.S. Mao, Titanium Dioxide Nanomaterials: Synthesis, Properties, Modifications, and Applications, Chem. Rev. 107 (2007) 2891–2959. doi:10.1021/cr0500535.

[46] A. fujishima, K. Honda, Electrochemical Photolysis of Water at a Semiconductor Electrode, Nature. 238 (1972) 37–38. doi:10.1038/238037a0.

[47] A.L. Linsebigler, G. Lu, J.T. Yates, Photocatalysis on TiO_2 Surfaces: Principles, Mechanisms, and Selected Results, Chem. Rev. 95 (1995) 735–758. doi:10.1021/cr00035a013.

[48] H. Park, Y. Park, W. Kim, W. Choi, Surface modification of TiO_2 photocatalyst for environmental applications, J. Photochem. Photobiol. C Photochem. Rev. 15 (2013) 1–20. doi:10.1016/j.jphotochemrev.2012.10.001.

[49] H. Park, H. Kim, G. Moon, W. Choi, Photoinduced charge transfer processes in solar photocatalysis based on modified TiO_2, Energy Environ. Sci. 9 (2016) 411–433. doi:10.1039/C5EE02575C.

[50] N. Serpone, Is the Band Gap of Pristine TiO_2 Narrowed by Anion- and Cation-Doping of Titanium Dioxide in Second-Generation Photocatalysts?, J. Phys. Chem. B. 110 (2006) 24287–24293. doi:10.1021/jp065659r.

[51] S. Chen, L.-W. Wang, Thermodynamic Oxidation and Reduction Potentials of Photocatalytic Semiconductors in Aqueous Solution, Chem. Mater. 24 (2012) 3659–3666. doi:10.1021/cm302533s.

[52] U. Diebold, The surface science of titanium dioxide, Surf. Sci. Rep. 48 (2003) 53–229. doi:10.1016/S0167-5729(02)00100-0.

[53] O. CARP, Photoinduced reactivity of titanium dioxide, Prog. Solid State Chem. 32 (2004) 33–177. doi:10.1016/j.progsolidstchem.2004.08.001.

[54] C.G. Enke, Nonstoichiometry, diffusion, and electrical conductivity in binary metal oxides. (Wiley series on the science and technology of materials)., 1974. doi:10.1002/maco.19740251027.

[55] T. Bak, J. Nowotny, M. Rekas, C.C. Sorrell, Defect chemistry and semiconducting properties of titanium dioxide: III. Mobility of electronic charge carriers, J. Phys. Chem. Solids. 64 (2003) 1069–1087. doi:10.1016/S0022-3697(02)00481-X.

[56] E. Yagi, R.R. Hasiguti, M. Aono, Electronic Conduction Above 4 K of Slightly Reduced Oxygen-Deficient Rutile TiO_{2-x}, Phys. Rev. B. 54 (1996) 7945–7956. doi:10.1103/PhysRevB.54.7945.

[57] R. Beranek, B. Neumann, S. Sakthivel, M. Janczarek, T. Dittrich, H. Tributsch, H. Kisch, Exploring the electronic structure of nitrogen-modified TiO_2 photocatalysts through photocurrent and surface photovoltage studies, Chem. Phys. 339 (2007) 11–19. doi:10.1016/j.chemphys.2007.05.022.

[58] X. Hu, G. Li, J.C. Yu, Design, Fabrication, and Modification of Nanostructured Semiconductor Materials for Environmental and Energy Applications, Langmuir. 26 (2010) 3031–3039. doi:10.1021/la902142b.

[59] K. Shankar, J.I. Basham, N.K. Allam, O.K. Varghese, G.K. Mor, X. Feng, M. Paulose, J.A. Seabold, K.-S. Choi, C.A. Grimes, Recent Advances in the Use of TiO_2 Nanotube and Nanowire Arrays for Oxidative Photoelectrochemistry, J. Phys. Chem. C. 113 (2009) 6327–6359. doi:10.1021/jp809385x.

[60] G.K. Mor, K. Shankar, M. Paulose, O.K. Varghese, C.A. Grimes, Enhanced Photocleavage of Water Using Titania Nanotube Arrays, Nano Lett. 5 (2005) 191–195. doi:10.1021/nl048301k.

[61] J.J. Kelly, The influence of fluoride ions on the passive dissolution of titanium, Electrochim. Acta. 24 (1979) 1273–1282. doi:10.1016/0013-4686(79)87084-X.

[62] L. V. Taveira, J.M. Macák, H. Tsuchiya, L.F.P. Dick, P. Schmuki, Initiation and Growth of Self-Organized TiO_2 Nanotubes Anodically Formed in NH4F ⁄ (NH4) 2SO4 Electrolytes, J. Electrochem. Soc. 152 (2005) B405. doi:10.1149/1.2008980.

[63] P. Hoyer, Formation of a Titanium Dioxide Nanotube Array, Langmuir. 12 (1996) 1411–1413. doi:10.1021/la9507803.

[64] S.-Z. Chu, K. Wada, S. Inoue, M. Isogai, A. Yasumori, Fabrication of Ideally Ordered Nanoporous Alumina Films and Integrated Alumina Nanotubule Arrays by High-Field Anodization, Adv. Mater. 17 (2005) 2115–2119. doi:10.1002/adma.200500401.

[65] T. Kasuga, M. Hiramatsu, A. Hoson, T. Sekino, K. Niihara, Formation of Titanium Oxide Nanotube, Langmuir. 14 (1998) 3160–3163. doi:10.1021/la9713816.

[66] J.M. Macak, H. Hildebrand, U. Marten-Jahns, P. Schmuki, Mechanistic aspects and growth of large diameter self-organized TiO_2 nanotubes, J. Electroanal. Chem. 621 (2008) 254–266. doi:10.1016/j.jelechem.2008.01.005.

[67] Q. Chen, W. Zhou, G.H. Du, L.-M. Peng, Trititanate Nanotubes Made via a Single Alkali Treatment, Adv. Mater. 14 (2002) 1208–1211. doi:10.1002/1521-4095(20020903)14:17<1208::AID-ADMA1208>3.0.CO;2-0.

[68] A. Michailowski, D. AlMawlawi, G. Cheng, M. Moskovits, Highly regular anatase nanotubule arrays fabricated in porous anodic templates, Chem. Phys. Lett. 349 (2001) 1–5. doi:10.1016/S0009-

2614(01)01159-9.

[69] Z.R. Tian, J.A. Voigt, J. Liu, B. Mckenzie, H. Xu, Large Oriented Arrays and Continuous Films of TiO 2 -Based Nanotubes, J. Am. Chem. Soc. 125 (2003) 12384–12385. doi:10.1021/ja0369461.

[70] K.-S. Ahn, S.-H. Lee, A.C. Dillon, C.E. Tracy, R. Pitts, The effect of thermal annealing on photoelectrochemical responses of WO_3 thin films, J. Appl. Phys. 101 (2007) 93524. doi:10.1063/1.2729472.

[71] T. Zhu, M.N. Chong, E.S. Chan, Nanostructured tungsten trioxide thin films synthesized for photoelectrocatalytic water oxidation: A review, ChemSusChem. 7 (2014) 2974–2997. doi:10.1002/cssc.201402089.

[72] C.A. Bignozzi, S. Caramori, V. Cristino, R. Argazzi, L. Meda, A. Tacca, Nanostructured photoelectrodes based on WO_3: applications to photooxidation of aqueous electrolytes, Chem. Soc. Rev. 42 (2013) 2228–2246. doi:10.1039/C2CS35373C.

[73] M.C. Martínez-Rivera, B.W. Berry, K.G. Valentine, K. Westerlund, S. Hay, C. Tommos, Electrochemical and Structural Properties of a Protein System Designed To Generate Tyrosine Pourbaix Diagrams, J. Am. Chem. Soc. 133 (2011) 17786–17795. doi:10.1021/ja206876h.

[74] R. Vijayalakshmi, M. Jayachandran, D. Trivedi, C. Sanjeeviraja, Characterization of WO_3 Thin Films Prepared at Different Deposition Currents on CTO Substrates, Synth. React. Inorganic, Met. Nano-Metal Chem. (Formerly Synth. React. Inorg. Met. Chem. 36 (2006) 89–94. doi:10.1080/15533170500478610.

[75] N. Sonoyama, K. Iwase, H. Takatsuka, T. Matsumura, N. Imanishi, Y. Takeda, R. Kanno, Electrochemistry of LiMn2O4 epitaxial films deposited on various single crystal substrates, J. Power Sources. 189 (2009) 561–565. doi:10.1016/j.jpowsour.2008.10.037.

[76] P.E. Hovsepian, D.B. Lewis, Q. Luo, A. Farinotti, Corrosion resistance of CrN/NbN superlattice coatings grown by various physical vapour deposition techniques, Thin Solid Films. 488 (2005) 1–8. doi:10.1016/j.tsf.2005.03.016.

[77] S. Feng, J. Yang, M. Liu, H. Zhu, J. Zhang, G. Li, J. Peng, Q. Liu, CdS quantum dots sensitized TiO_2 nanorod-array-film

photoelectrode on FTO substrate by electrochemical atomic layer epitaxy method, Electrochim. Acta. 83 (2012) 321–326. doi:10.1016/j.electacta.2012.07.130.

[78] D.J. Comstock, S.T. Christensen, J.W. Elam, M.J. Pellin, M.C. Hersam, Synthesis of nanoporous activated iridium oxide films by anodized aluminum oxide templated atomic layer deposition, Electrochem. Commun. 12 (2010) 1543–1546. doi:10.1016/j.elecom.2010.08.029.

[79] S. Gupta, M. Tripathi, A review on the synthesis of TiO_2 nanoparticles by solution route, Open Chem. 10 (2012). doi:10.2478/s11532-011-0155-y.

[80] T. Pauporté, A. Goux, A. Kahn-Harari, N. de Tacconi, C.R. Chenthamarakshan, K. Rajeshwar, D. Lincot, Cathodic electrodeposition of mixed oxide thin films, J. Phys. Chem. Solids. 64 (2003) 1737–1742. doi:10.1016/S0022-3697(03)00122-7.

[81] E.A. Meulenkamp, Mechanism of WO3 Electrodeposition from Peroxy-Tungstate Solution, J. Electrochem. Soc. 144 (1997) 1664. doi:10.1149/1.1837657.

[82] W.L. Kwong, N. Savvides, C.C. Sorrell, Electrodeposited nanostructured WO_3 thin films for photoelectrochemical applications, Electrochim. Acta. 75 (2012) 371–380. doi:10.1016/j.electacta.2012.05.019.

[83] P.K. Shen, A.C.C. Tseung, Study of electrodeposited tungsten trioxide thin films, J. Mater. Chem. 2 (1992) 1141. doi:10.1039/jm9920201141.

[84] L. Kondrachova, B.P. Hahn, G. Vijayaraghavan, R.D. Williams, K.J. Stevenson, Cathodic Electrodeposition of Mixed Molybdenum Tungsten Oxides from Peroxo-polymolybdotungstate Solutions, Langmuir. 22 (2006) 10490–10498. doi:10.1021/la061299n.

[85] B. Yang, H. Li, M. Blackford, V. Luca, Novel low density mesoporous WO_3 films prepared by electrodeposition, Curr. Appl. Phys. 6 (2006) 436–439. doi:10.1016/j.cap.2005.11.035.

[86] N. Li, B. Zhou, P. Guo, J. Zhou, D. Jing, Fabrication of noble-metal-free Cd0.5Zn0.5S/NiS hybrid photocatalyst for efficient solar hydrogen evolution, Int. J. Hydrogen Energy. 38 (2013) 11268–

11277. doi:10.1016/j.ijhydene.2013.06.067.

[87] S.H. Baeck, T. Jaramillo, G.D. Stucky, E.W. McFarland, Controlled Electrodeposition of Nanoparticulate Tungsten Oxide, Nano Lett. 2 (2002) 831–834. doi:10.1021/nl025587p.

[88] W.J. Lee, P.S. Shinde, G.H. Go, C.H. Doh, Enhanced photoelectrochemical performance of WO_3/Ti photoanode due to in situ formation of a thin interfacial composite layer, Appl. Surf. Sci. 270 (2013) 267–271. doi:10.1016/j.apsusc.2013.01.013.

[89] M. Seifollahi Bazarjani, M. Hojamberdiev, K. Morita, G. Zhu, G. Cherkashinin, C. Fasel, T. Herrmann, H. Breitzke, A. Gurlo, R. Riedel, Visible Light Photocatalysis with c-WO_{3-x} /WO_3×H_2O Nanoheterostructures In Situ Formed in Mesoporous Polycarbosilane-Siloxane Polymer, J. Am. Chem. Soc. 135 (2013) 4467–4475. doi:10.1021/ja3126678.

[90] Y.-C. Nah, A. Ghicov, D. Kim, P. Schmuki, Enhanced electrochromic properties of self-organized nanoporous WO_3, Electrochem. Commun. 10 (2008) 1777–1780. doi:10.1016/j.elecom.2008.09.017.

[91] C. Ng, Y.H. Ng, A. Iwase, R. Amal, Influence of Annealing Temperature of WO_3 in Photoelectrochemical Conversion and Energy Storage for Water Splitting, ACS Appl. Mater. Interfaces. 5 (2013) 5269–5275. doi:10.1021/am401112q.

[92] S. Berger, H. Tsuchiya, A. Ghicov, P. Schmuki, High photocurrent conversion efficiency in self-organized porous WO_3, Appl. Phys. Lett. 88 (2006) 203119. doi:10.1063/1.2206696.

[93] Y. Liu, Y. Li, W. Li, S. Han, C. Liu, Photoelectrochemical properties and photocatalytic activity of nitrogen-doped nanoporous WO3 photoelectrodes under visible light, Appl. Surf. Sci. 258 (2012) 5038–5045. doi:10.1016/j.apsusc.2012.01.080.

[94] M. Regragui, M. Addou, B. El Idrissi, J.C. Bernède, A. Outzourhit, E. Ec-chamikh, Effect of the annealing time on the physico-chemical properties of WO_3 thin films prepared by spray pyrolysis, Mater. Chem. Phys. 70 (2001) 84–89. doi:10.1016/S0254-0584(00)00464-8.

[95] H.W. Jeong, T.H. Jeon, J.S. Jang, W. Choi, H. Park, Strategic

Modification of $BiVO_4$ for Improving Photoelectrochemical Water Oxidation Performance, J. Phys. Chem. C. 117 (2013) 9104–9112. doi:10.1021/jp400415m.

[96] H. Kim, J. Kim, W. Kim, W. Choi, Enhanced Photocatalytic and Photoelectrochemical Activity in the Ternary Hybrid of CdS/TiO_2 /WO_3 through the Cascadal Electron Transfer, J. Phys. Chem. C. 115 (2011) 9797–9805. doi:10.1021/jp1122823.

[97] T. Ohno, F. Tanigawa, K. Fujihara, S. Izumi, M. Matsumura, Photocatalytic oxidation of water on TiO_2-coated WO_3 particles by visible light using Iron(III) ions as electron acceptor, J. Photochem. Photobiol. A Chem. 118 (1998) 41–44. doi:10.1016/S1010-6030(98)00374-8.

[98] H. Park, A. Bak, T.H. Jeon, S. Kim, W. Choi, Photo-chargeable and dischargeable TiO_2 and WO_3 heterojunction electrodes, Appl. Catal. B Environ. 115–116 (2012) 74–80. doi:10.1016/j.apcatb.2011.12.006.

[99] R. Costi, A.E. Saunders, E. Elmalem, A. Salant, U. Banin, Visible Light-Induced Charge Retention and Photocatalysis with Hybrid CdSe−Au Nanodumbbells, Nano Lett. 8 (2008) 637–641. doi:10.1021/nl0730514.

[100] J. Fang, J. Wu, X. Lu, Y. Shen, Z. Lu, Sensitization of nanocrystalline TiO_2 electrode with quantum sized CdSe and ZnTCPc molecules, Chem. Phys. Lett. 270 (1997) 145–151. doi:10.1016/S0009-2614(97)00333-3.

[101] H. Park, W. Choi, M.R. Hoffmann, Effects of the preparation method of the ternary CdS/TiO_2/Pt hybrid photocatalysts on visible light-induced hydrogen production, J. Mater. Chem. 18 (2008) 2379. doi:10.1039/b718759a.

[102] W. Smith, Y. Zhao, Enhanced Photocatalytic Activity by Aligned WO_3/TiO_2 Two-Layer Nanorod Arrays, J. Phys. Chem. C. 112 (2008) 19635–19641. doi:10.1021/jp807703d.

[103] D. Zhao, C. Chen, C. Yu, W. Ma, J. Zhao, Photoinduced Electron Storage in WO_3/TiO_2 Nanohybrid Material in the Presence of Oxygen and Postirradiated Reduction of Heavy Metal Ions, J. Phys. Chem. C. 113 (2009) 13160–13165. doi:10.1021/jp9002774.

[104] H. Park, W. Choi, K.Y. Kim, A novel photoelectrochemical method of metal corrosion prevention using a TiO_2 solar panel, Chem. Commun. (2001) 281–282. doi:10.1039/b008106j.

[105] D. Tsukamoto, M. Ikeda, Y. Shiraishi, T. Hara, N. Ichikuni, S. Tanaka, T. Hirai, Selective photocatalytic oxidation of alcohols to aldehydes in water by TiO_2 partially coated with WO_3, Chem. - A Eur. J. 17 (2011) 9816–9824. doi:10.1002/chem.201100166.

[106] S. Bai, J. Jiang, Q. Zhang, Y. Xiong, Steering charge kinetics in photocatalysis: intersection of materials syntheses, characterization techniques and theoretical simulations, Chem. Soc. Rev. 44 (2015) 2893–2939. doi:10.1039/C5CS00064E.

[107] S.. M.Sze, L. Minng-Kve, SEMICONDUCTOR DEVICES: PHYSICS AND TECHNOLOGY, 2nd ed., 2008.

[108] V. Subramanian, E.E. Wolf, P. V. Kamat, Catalysis with TiO_2 /Gold Nanocomposites. Effect of Metal Particle Size on the Fermi Level Equilibration, J. Am. Chem. Soc. 126 (2004) 4943–4950. doi:10.1021/ja0315199.

[109] M.G. Walter, E.L. Warren, J.R. McKone, S.W. Boettcher, Q. Mi, E.A. Santori, N.S. Lewis, Solar Water Splitting Cells, Chem. Rev. 110 (2010) 6446–6473. doi:10.1021/cr1002326.

[110] M. Grätzel, Photoelectrochemical cells, Nature. 414 (2001) 338–344. doi:10.1038/35104607.

[111] Y. Li, T. Takata, D. Cha, K. Takanabe, T. Minegishi, J. Kubota, K. Domen, Vertically Aligned Ta_3N_5 Nanorod Arrays for Solar-Driven Photoelectrochemical Water Splitting, Adv. Mater. 25 (2013) 125–131. doi:10.1002/adma.201202582.

[112] A. Paracchino, V. Laporte, K. Sivula, M. Grätzel, E. Thimsen, Highly active oxide photocathode for photoelectrochemical water reduction, Nat. Mater. 10 (2011) 456–461. doi:10.1038/nmat3017.

[113] J. Yang, D. Wang, H. Han, C. Li, Roles of Cocatalysts in Photocatalysis and Photoelectrocatalysis, Acc. Chem. Res. 46 (2013) 1900–1909. doi:10.1021/ar300227e.

[114] M. Rycenga, C.M. Cobley, J. Zeng, W. Li, C.H. Moran, Q. Zhang, D. Qin, Y. Xia, Controlling the Synthesis and Assembly of Silver

Nanostructures for Plasmonic Applications, Chem. Rev. 111 (2011) 3669–3712. doi:10.1021/cr100275d.

[115] C. Langhammer, Z. Yuan, I. Zorić, B. Kasemo, Plasmonic Properties of Supported Pt and Pd Nanostructures, Nano Lett. 6 (2006) 833–838. doi:10.1021/nl060219x.

[116] X. Zhang, Y.L. Chen, R.-S. Liu, D.P. Tsai, Plasmonic photocatalysis, Reports Prog. Phys. 76 (2013) 46401. doi:10.1088/0034-4885/76/4/046401.

[117] W. Fan, Q. Zhang, Y. Wang, Semiconductor-based nanocomposites for photocatalytic H2 production and CO_2 conversion, Phys. Chem. Chem. Phys. 15 (2013) 2632. doi:10.1039/c2cp43524a.

[118] S.S. Lo, T. Mirkovic, C.-H. Chuang, C. Burda, G.D. Scholes, Emergent Properties Resulting from Type-II Band Alignment in Semiconductor Nanoheterostructures, Adv. Mater. 23 (2011) 180–197. doi:10.1002/adma.201002290.

[119] Y. Zhu, Y. Liu, Y. Lv, Q. Ling, D. Liu, Y. Zhu, Enhancement of photocatalytic activity for BiPO 4 via phase junction, J. Mater. Chem. A. 2 (2014) 13041. doi:10.1039/C4TA01807A.

[120] H. Tada, T. Mitsui, T. Kiyonaga, T. Akita, K. Tanaka, All-solid-state Z-scheme in CdS–Au–TiO_2 three-component nanojunction system, Nat. Mater. 5 (2006) 782–786. doi:10.1038/nmat1734.

[121] P. Zhou, J. Yu, M. Jaroniec, All-Solid-State Z-Scheme Photocatalytic Systems, Adv. Mater. 26 (2014) 4920–4935. doi:10.1002/adma.201400288.

[122] A. Kudo, Z-scheme photocatalyst systems for water splitting under visible light irradiation, MRS Bull. 36 (2011) 32–38. doi:10.1557/mrs.2010.3.

[123] F.F. Tao, W.F. Schneider, P. V. Kamat, Heterogeneous Catalysis at Nanoscale for Energy Applications, in: Heterog. Catal. Nanoscale Energy Appl., John Wiley & Sons, Inc, Hoboken, NJ, 2015: pp. 1–7. doi:10.1002/9781118843468.ch1.

[124] L. Ye, J. Liu, C. Gong, L. Tian, T. Peng, L. Zan, Two Different Roles of Metallic Ag on Ag/AgX/BiO_X (X =Cl,Br) Visible Light Photocatalysts: Surface Plasmon Resonance and Z-Scheme Bridge,

ACS Catal. 2 (2012) 1677–1683. doi:10.1021/cs300213m.

[125] H.J. Yun, H. Lee, N.D. Kim, D.M. Lee, S. Yu, J. Yi, A Combination of Two Visible-Light Responsive Photocatalysts for Achieving the Z-Scheme in the Solid State, ACS Nano. 5 (2011) 4084–4090. doi:10.1021/nn2006738.

[126] Z. Liu, Z.-G. Zhao, M. Miyauchi, Efficient Visible Light Active $CaFe_2O_4/WO_3$ Based Composite Photocatalysts: Effect of Interfacial Modification, J. Phys. Chem. C. 113 (2009) 17132–17137. doi:10.1021/jp906195f.

[127] P. Li, Y. Zhou, H. Li, Q. Xu, X. Meng, X. Wang, M. Xiao, Z. Zou, All-solid-state Z-scheme system arrays of $Fe_2V_4O_{13}$ /RGO/CdS for visible light-driving photocatalytic CO_2 reduction into renewable hydrocarbon fuel, Chem. Commun. 51 (2015) 800–803. doi:10.1039/C4CC08744E.

[128] J. Yu, S. Wang, J. Low, W. Xiao, Enhanced photocatalytic performance of direct Z-scheme g-C_3N_4–TiO_2 photocatalysts for the decomposition of formaldehyde in air, Phys. Chem. Chem. Phys. 15 (2013) 16883. doi:10.1039/c3cp53131g.

[129] X. Wang, G. Liu, Z.-G. Chen, F. Li, L. Wang, G.Q. Lu, H.-M. Cheng, Enhanced photocatalytic hydrogen evolution by prolonging the lifetime of carriers in ZnO/CdS heterostructures, Chem. Commun. (2009) 3452. doi:10.1039/b904668b.

[130] W.G.H. George, E.P.Box J.Stuart Hunter, Statistics for Experimenters: Design, Innovation, and Discovery, 2nd Editio, 2005.

[131] S. Berger, R. Hahn, P. Roy, P. Schmuki, Self-organized TiO_2 nanotubes: Factors affecting their morphology and properties, Phys. Status Solidi. 247 (2010) 2424–2435. doi:10.1002/pssb.201046373.

[132] J.M. Macak, H. Tsuchiya, A. Ghicov, K. Yasuda, R. Hahn, S. Bauer, P. Schmuki, TiO_2 nanotubes: Self-organized electrochemical formation, properties and applications, Curr. Opin. Solid State Mater. Sci. 11 (2007) 3–18. doi:10.1016/j.cossms.2007.08.004.

[133] S. Palmas, M. Mascia, A. Vacca, I. Tredici, Photoelectrocatalytic Performances of Nanostructured/Decorated TiO_2 Electrodes: Effect of Wavelength and Cell Configuration, Int. J. Photoenergy. 2013

(2013) 1–10. doi:10.1155/2013/173760.

[134] A. El Ruby Mohamed, S. Rohani, Modified TiO_2 nanotube arrays (TNTAs): progressive strategies towards visible light responsive photoanode, a review, Energy Environ. Sci. 4 (2011) 1065. doi:10.1039/c0ee00488j.

[135] H. Park, H. Kim, G. Moon, W. Choi, Photoinduced charge transfer processes in solar photocatalysis based on modified TiO_2, Energy Environ. Sci. 9 (2016) 411–433. doi:10.1039/C5EE02575C.

[136] A. Pimentel, D. Nunes, S. Pereira, R. Martins, E. Fortunato, Photocatalytic Activity of TiO_2 Nanostructured Arrays Prepared by Microwave-Assisted Solvothermal Method, in: Semicond. Photocatal. - Mater. Mech. Appl., InTech, 2016. doi:10.5772/63237.

[137] B.H. Meekins, P. V. Kamat, Got TiO_2 Nanotubes? Lithium Ion Intercalation Can Boost Their Photoelectrochemical Performance, ACS Nano. 3 (2009) 3437–3446. doi:10.1021/nn900897r.

[138] J. Idigoras, R. Tena-Zaera, J.A. Anta, Control of the recombination rate by changing the polarity of the electrolyte in dye-sensitized solar cells, Phys. Chem. Chem. Phys. 16 (2014) 21513–21523. doi:10.1039/C4CP03303E.

[139] P. Pu, H. Cachet, E.M.M. Sutter, Electrochemical impedance spectroscopy to study photo - induced effects on self-organized TiO_2 nanotube arrays, Electrochim. Acta. 55 (2010) 5938–5946. doi:10.1016/j.electacta.2010.05.048.

[140] Z. Zhang, P. Wang, Optimization of photoelectrochemical water splitting performance on hierarchical TiO_2 nanotube arrays, Energy Environ. Sci. 5 (2012) 6506. doi:10.1039/c2ee03461a.

[141] Y. Ye, Y. Liu, T. Guo, Effect of H_2O content in electrolyte on synthesis and field emission property of anodized TiO2 nanotubes, Surf. Coatings Technol. 245 (2014) 28–33. doi:10.1016/j.surfcoat.2014.02.027.

[142] P. Ampudia, S. Palmas, A. Vacca, M. Mascia, R. Matarrese, Design of experiments (DOE) for synthesis of nanotubular structured electrodes, Chem. Eng. Trans. 41 (2014) 349–354. doi:10.3303/CET1441059.

[143] L. Assaud, S. Bochmann, S. Christiansen, J. Bachmann, A large electrochemical setup for the anodization of aluminum towards highly ordered arrays of cylindrical nanopores, Rev. Sci. Instrum. 86 (2015) 73902. doi:10.1063/1.4926746.

[144] D. Regonini, F.J. Clemens, Anodized TiO_2 Nanotubes: Effect of anodizing time on film length, morphology and photoelectrochemical properties, Mater. Lett. 142 (2015) 97–101. doi:10.1016/j.matlet.2014.11.145.

[145] L. Qin, Q. Chen, R. Lan, R. Jiang, X. Quan, B. Xu, F. Zhang, Y. Jia, Effect of Anodization Parameters on Morphology and Photocatalysis Properties of TiO_2 Nanotube Arrays, J. Mater. Sci. Technol. 31 (2015) 1059–1064. doi:10.1016/j.jmst.2015.07.012.

[146] C.W. Lai, S. Sreekantan, Photoelectrochemical Performance of Smooth TiO_2 Nanotube Arrays: Effect of Anodization Temperature and Cleaning Methods, Int. J. Photoenergy. 2012 (2012) 1–11. doi:10.1155/2012/356943.

[147] S. Palmas, M. Mascia, A. Vacca, P. Ampudia, L. Mais, F. Ferrara, A. Pettinau, I. Meccanica, C. Via, S.A. Sotacarbo, G. Miniera, On the behavior of modified TiO_2 nanotubes for a photoanode-driven photoelectrochemical reduction of CO 2, (2015) 128–131.

[148] K.R. Reyes-Gil, D.B. Robinson, WO_3 -Enhanced TiO_2 Nanotube Photoanodes for Solar Water Splitting with Simultaneous Wastewater Treatment, ACS Appl. Mater. Interfaces. 5 (2013) 12400–12410. doi:10.1021/am403369p.

[149] N. Detacconi, C. Chenthamarakshan, K. Rajeshwar, T. Pauporte, D. Lincot, Pulsed electrodeposition of WO_3-TiO_2 composite films, Electrochem. Commun. 5 (2003) 220–224. doi:10.1016/S1388-2481(03)00021-3.

[150] S. Darmawi, S. Burkhardt, T. Leichtweiss, D.A. Weber, S. Wenzel, J. Janek, M.T. Elm, P.J. Klar, Correlation of electrochromic properties and oxidation states in nanocrystalline tungsten trioxide, Phys. Chem. Chem. Phys. 17 (2015) 15903–15911. doi:10.1039/C5CP02482J.

[151] G. Cappelletti, C. Ricci, S. Ardizzone, C. Parola, A. Anedda, Aged Titania Nanoparticles: The Simultaneous Control of Local and

Long-Range Properties, J. Phys. Chem. B. 109 (2005) 4448–4454. doi:10.1021/jp045192p.

[152] S. Ardizzone, G. Cappelletti, C. Ricci, A. Sin, Nanocrystalline WO_3 Polymorphs. Surfactant Assisted Growth Steps to Tailor Microstructure and NO_2 Response, J. Nanosci. Nanotechnol. 10 (2010) 8367–8374. doi:10.1166/jnn.2010.2743.

[153] E. Salje, K. Viswanathan, Physical properties and phase transitions in WO_3, Acta Crystallogr. Sect. A. 31 (1975) 356–359. doi:10.1107/S0567739475000745.

[154] O. Berger, W.-J. Fischer, V. Melev, Tungsten-oxide thin films as novel materials with high sensitivity and selectivity to NO_2, O_3 and H_2S. Part I: Preparation and microstructural characterization of the tungsten-oxide thin films, J. Mater. Sci. Mater. Electron. 15 (2004) 463–482. doi:10.1023/B:JMSE.0000031601.29022.07.

[155] K.J. Lethy, D. Beena, R. Vinod Kumar, V.P. Mahadevan Pillai, V. Ganesan, V. Sathe, Structural, optical and morphological studies on laser ablated nanostructured WO_3 thin films, Appl. Surf. Sci. 254 (2008) 2369–2376. doi:10.1016/j.apsusc.2007.09.068.

[156] K.K. Akurati, A. Vital, J.-P. Dellemann, K. Michalow, T. Graule, D. Ferri, A. Baiker, Flame-made WO_3/TiO_2 nanoparticles: Relation between surface acidity, structure and photocatalytic activity, Appl. Catal. B Environ. 79 (2008) 53–62. doi:10.1016/j.apcatb.2007.09.036.

[157] S. Bai, J. Jiang, Q. Zhang, Y. Xiong, Steering charge kinetics in photocatalysis: intersection of materials syntheses, characterization techniques and theoretical simulations, Chem. Soc. Rev. 44 (2015) 2893–2939. doi:10.1039/C5CS00064E.

[158] S. Palmas, A. Da Pozzo, F. Delogu, M. Mascia, A. Vacca, G. Guisbiers, Characterization of TiO_2 nanotubes obtained by electrochemical anodization in organic electrolytes, J. Power Sources. 204 (2012) 265–272. doi:10.1016/j.jpowsour.2012.01.007.

[159] W.-Y. Wang, B.-R. Chen, Characterization and Photocatalytic Activity of TiO_2 Nanotube Films Prepared by Anodization, Int. J. Photoenergy. 2013 (2013) 1–12. doi:10.1155/2013/348171.

[160] S. Palmas, M. Mascia, A. Vacca, J. Llanos, E. Mena, Analysis of

photocurrent and capacitance of TiO_2 nanotube–polyaniline hybrid composites synthesized through electroreduction of an aryldiazonium salt, RSC Adv. 4 (2014) 23957. doi:10.1039/c4ra01712a.

[161] T. Zhu, M.N. Chong, E.S. Chan, Nanostructured Tungsten Trioxide Thin Films Synthesized for Photoelectrocatalytic Water Oxidation: A review, ChemSusChem. 7 (2014) 2974–2997. doi:10.1002/cssc.201402089.

[162] S. Palmas, A. Da Pozzo, M. Mascia, A. Vacca, R. Matarrese, I. Nova, Photo-electrochemical behavior at different wavelengths of electrochemically obtained TiO_2 nanotubes, J. Appl. Electrochem. 42 (2012) 745–751. doi:10.1007/s10800-012-0456-7.

[163] X.. Li, F.. Li, C.. Yang, W.. Ge, Photocatalytic activity of WO_x-TiO_2 under visible light irradiation, J. Photochem. Photobiol. A Chem. 141 (2001) 209–217. doi:10.1016/S1010-6030(01)00446-4.

[164] F. Le Formal, S.R. Pendlebury, M. Cornuz, S.D. Tilley, M. Grätzel, J.R. Durrant, Back Electron–Hole Recombination in Hematite Photoanodes for Water Splitting, J. Am. Chem. Soc. 136 (2014) 2564–2574. doi:10.1021/ja412058x.

[165] M.R. Hasan, S.B. Abd Hamid, W.J. Basirun, S.H. Meriam Suhaimy, A.N. Che Mat, A sol–gel derived, copper-doped, titanium dioxide–reduced graphene oxide nanocomposite electrode for the photoelectrocatalytic reduction of CO_2 to methanol and formic acid, RSC Adv. 5 (2015) 77803–77813. doi:10.1039/C5RA12525A.

[166] W. Lee, C. Lai, S. Hamid, In Situ Anodization of WO_3-Decorated TiO_2 Nanotube Arrays for Efficient Mercury Removal, Materials (Basel). 8 (2015) 5702–5714. doi:10.3390/ma8095270.

[167] M.M. Momeni, Y. Ghayeb, Fabrication, characterization and photocatalytic properties of Au/TiO_2-WO_3 nanotubular composite synthesized by photo-assisted deposition and electrochemical anodizing methods, J. Mol. Catal. A Chem. 417 (2016) 107–115. doi:10.1016/j.molcata.2016.03.024.

[168] R. Poulomi,S. Berger, P. Schmuki, TiO_2 Nanotubes: Synthesis and Applications, *Angew. Chem. Int.* 50 No.13 (2011) 2904-2939, doi: 0.1002/anie.201001374.

[169] Varghese C. K., Paulose M., Shankar K., Mor G. K., Grimes C. A. J. Nanosci. Nanotechnol. 2005, 5, 1158.

[170] S.C. Pillai ,P. Periyat ,R. George ,D.E. McCormack ,M.K. Seery , H. Hayden ,J. Colreavy ,D. Corr ,S. J. Hinder, Synthesis of High-Temperature Stable Anatase TiO2 Photocatalyst, J. Phys. Chem. C, 111 (4) (2007), 1605–1611, doi: 10.1021/jp065933h.

[171] F.A. Scaramuzzo, M. Pasqualia, F. Muraa, A. Poziob, A. Dell'Eraa, A. Curullic, TiO_2 Nanotubes Photo-anode: an Innovative Cell Design, Chem. Eng. Trans 41 (2014), doi: 10.3303/CET1441038

Symbols and acronyms

A	electron affinity
AM	air mass filter
a_{ox}	activity of oxidized species
a_{red}	activity of reduced species
C	capacitance
c	speed of light
C_B	conduction band
C_{dl}	double layer capacitance
CE	counter electrode
C_G	capacitance of the Gouy-Chapman layer
C_H	capacitance of the Helmholtz double layer
C_o	concentration of oxidized species
CPE	constant phase element
CR	charge recombination
C_R	concentration of reduced species
C_{SC}	capacitance of the space charge layer
CTO	TiO_2 thermal compact oxide
CV	cyclic voltammetry
D	electron donor species
d	thickness

DI	deionized water
DOE	design of experiments
$D_{ox}(E)$	density of states for oxidized species in a solution
D_p	hole diffusion constant
$D_{red}(E)$	density of states for reduced species in a solution
E	energy
e^-, e’	electron
E, E_{appl}	applied potential
$E^{0,}$	formal reduction potential of the redox couple
E^0_{fb}	flat band potential at pH=0
E^0_{ox}	Fermi level of oxidized species
E^0_{red}	Fermi level of reduced species
E^0_{redox}	standard reduction potential
E^0_{rev}	standard reference potential for water splitting reaction
E_A	semiconductor affinity
E_b	external positive potential bias
E_f	Fermi level
$E_{F,redox}$	Fermi Level of a redox couple
E_{f*}	quasi-Fermi level
$^*E_{Fn}$	quasi-Fermi level of electrons
$^*E_{Fp}$	quasi-Fermi level of holes
E_{fb}, U_{fb}	flatband potential

Eg	bandgap energy
EG	ethylen glycol
EIS	Electrochemical Impedance Spectroscopy
	Electron acceptor species
EMF	electromotive force
E_{OC}, OCV	open-circuit potential
E_{redox}	electrochemical potential of electrons in solution
E_V	valence band edge
$E_{V,S}$	valence band edge at the surface
F	Faraday constant
F	fluoride concentration
f	frequency
F(R)	Kubelka-Munk function
FE-SEM	field-emission scanning electron microscope
FIB	focused ion beam
F	fluorides
	Concentration of fluorides
G	glycerol
h^+, $h^{\cdot}$	hole
$h\nu$	energy of light
I	current density
i_0	exchange current density at the interface

i_a	anodic current
i_c	cathodic current
I_{dep}	photocurrent generated in the depletion layer
I_{diff}	photocurrent due to the diffusion contribution
IPCE	incident photon to current efficiency
I_{ph}	photocurrent density
I_{SC}	short-circuit photocurrent
I_{sph}	saturation photocurrent density
J	concentration of sodium tungstate in the anodization bath
k	Boltzman constant
k_0	standar rate constant
k_b	recation rate constant for oxidation
k_f	reaction rate constant for reduction
kT	thermal energy
L	average crystallite size
	number of levels in DOE
$L(\lambda)$	penetration depth of light
L_D	Debye lenght
	levels in DOE
L_p	diffusion lenght of the minority carries
N	minimun number of samples in DOE
n	number of electrons transfered in a redox recation

	exponent in the constant phase element equation
	parameters in DOE
n(x)	density of electrons at the thermodynamic equilibrium
N_a	Avogadro's number
N_A	density of aceptor states
N_D	density of donor atates
NHE	normal hydrogen electrode
NIR	near-infrarred light
NPC	Normalized photocurrent density
NT	nanotubular structures
OC	TiO_2 compact oxide
OCVDM	open circuit decay measurements
O_x,O	oxidized species
P	incident power density of light
$p_{(x)}$	density of holes at the thermodinamic equilibrium
p_0	equilibrium hole concentration with no illumination
PEC	photoelectrochemical
PPT	pulse potential technique
p_{SC}	density of holes in the space charge region
Q	accumulated charge
q	elementary charge
R	universal gas constant

R, Red	reduces species
R_{CT}	Charge transfer resistance
RE	reference electrode
R	resistance
R_S	Ohmic solution resistance
S	Solvent content
SCE	Satured Calomel Electrode
SEM	Scanning electron microscopy
T	temperature
T	titanium dioxide
Ti	titanium
TiO_2	Titania
	Titania-Tungsten oxide under layer
U	potential
UV	ultraviolet light
VB	valance band
vis	visible light
W	Tungsten
	Tungsten oxide
W	Width of the depletion layer
W_0	depletion-layer width for a potential of 1
W	Wargbur impedance

W	Water content
WE	working electrode
WO_3	tungsten oxide
WO_x	tungsten oxide electrodeposited layer
X	Titania Under layer
XDR	X-ray diffractometry
y	WO_3 electrodeposition time
Z	Impedance
Z'	real component of impedance
Z''	imaginary component of impedance
α	absorption coefficient
γ	parameter that measure the CR at the original structure
ΔG	Gibbs free energy
ε	relative permittivity
ε_0	permittivity of vacuum
ε_r	dielectric constant of the semiconductor
λ	reorganization energy, wavelenght
τ	time constante in EIS measuremets
τ_n	electron lifetime
Φ	effective quantum yield
ϕ	aspect ratio
φ_0	phon flux

Φ_G	potential drop within the Gouy layer
Φ_H	potential drop within the Helmoltz layer
Φ_{OHP}	the potential at the Outer Helmoltz Plane (OHP)
Φ_{SC}	potential drop within the space charge region
ω	Angular frequency of rotation

List of Figures

List of Tables